DOCTOR OF PHILOSOPHY

Strong-field quantum electrodynamics in the field of ultra-intense lasers

Fleck, Kyle James

Award date:
2025

Awarding institution:
Queen's University Belfast

Link to publication

Terms of use
All those accessing thesis content in Queen's University Belfast Research Portal are subject to the following terms and conditions of use

- Copyright is subject to the Copyright, Designs and Patent Act 1988, or as modified by any successor legislation
- Copyright and moral rights for thesis content are retained by the author and/or other copyright owners
- A copy of a thesis may be downloaded for personal non-commercial research/study without the need for permission or charge
- Distribution or reproduction of thesis content in any format is not permitted without the permission of the copyright holder
- When citing this work, full bibliographic details should be supplied, including the author, title, awarding institution and date of thesis

Take down policy
A thesis can be removed from the Research Portal if there has been a breach of copyright, or a similarly robust reason.
If you believe this document breaches copyright, or there is sufficient cause to take down, please contact us, citing details. Email:
openaccess@qub.ac.uk

Supplementary materials
Where possible, we endeavour to provide supplementary materials to theses. This may include video, audio and other types of files. We endeavour to capture all content and upload as part of the Pure record for each thesis.
Note, it may not be possible in all instances to convert analogue formats to usable digital formats for some supplementary materials. We exercise best efforts on our behalf and, in such instances, encourage the individual to consult the physical thesis for further information.

Download date: 08. Jul. 2025

THE QUEEN'S UNIVERSITY BELFAST

SCHOOL OF MATHEMATICS AND PHYSICS

Strong-Field Quantum Electrodynamics in the Field of Ultra-Intense Lasers

Kyle James Fleck

MSci Applied Mathematics and Physics

A thesis presented upon application for admission to the degree of

DOCTOR OF PHILOSOPHY

in the Faculty of Engineering and Physical Sciences

June 2025

Abstract

Quantum electrodynamics (QED) is among the most precise theories in physics, with excellent agreement between theory and experiment in the perturbative regime. However, QED in strong background fields remains less explored experimentally due to the challenges in generating such environments. Theoretical studies have proposed various processes and calculation frameworks in this regime, but experimental validation is essential to improve theoretical understanding. To this end, experiments using ultra-intense laser fields or strong nuclear fields of crystals have been proposed, aiming to probe strong-field QED via the detection of emitted particles. These studies demand advanced detectors capable of withstanding extreme high-energy and high-flux conditions.

This thesis presents the development of two such detection techniques. Firstly, a gamma-ray spectrometer, designed to measure the energy spectra of high flux and energy photon beams is discussed, detailing its operation principles and simulation studies of its expected performance. A first experimental characterisation of the spectrometer is also presented, which involved the measurement of a $\sim$ 1 GeV bremsstrahlung source.

Secondly, an approach to inferring interaction properties from the spatial profile of a Compton-scattered photon beam is presented. The theory of this method is developed, with numerical studies for different interaction parameters considered, as well as a range of validity for applying the technique. This method is applied to a proposed gamma beam profiler for the LUXE experiment, with simulations demonstrating its effectiveness.

Finally, an experimental setup targeting rare two-photon QED processes, linear Breit-Wheeler production and elastic photon-photon scattering, is examined. The use of current and next-generation PW-class laser facilities is shown to significantly enhance signal yields. Simulation results support order-of-magnitude estimates, suggesting that direct observation and stringent bounds on these processes are feasible.

Contents

List of Figures

List of Tables

List Of Abbreviations

CPA	Chirped Pulse Amplification
FWHM	Full Width at Half Maximum
GRS	Gamma-Ray Spectrometer
HPDI	Highest Posterior Density Interval
IP	Interaction Point
LAD	Lorentz-Abraham-Dirac (equation)
LBW	Linear Breit-Wheeler (pair production)
LCS	Linear (Inverse) Compton Scattering
LL	Landau-Lifschitz (equation)
LUXE	Laser Und XFEL Experiment
LWFA	Laser Wakefield Acceleration
MAP	Maximum A Posteriori
MC	Monte-Carlo (simulation)
MLM	Marginal Likelihood Maximisation
NLBW	Non-Linear Breit-Wheeler (pair production)
NLCS	Non-Linear (Inverse) Compton Scattering

QED	Quantum Electrodynamics
RMS	Root Mean Square
RR	Radiation Reaction
SFQED	Strong-Field Quantum Electrodynamics
ZMF	Zero Momentum Frame

Acknowledgements

To begin with, none of the work done over the last three years would have been possible without the incredible support of my supervisors, Gianluca Sarri and Marco Borghesi. Their supervision, guidance and ever-inspiring depth of knowledge has been a great help and impetus in discussions over many a problem.

I'd also like to thank Dr. Tom Blackburn and the wider LUXE collaboration for effectively training me on strong-field QED simulations and analysis; this has become a vital part of my work here. To the people I have had the fortune to work with as part of the Sarri research group: our discussions, rants, debugging sessions and lunches have played an essential part as well.

I'm extremely thankful for my friends, particularly Mark, Rachel and Sara, for keeping me sane and reminding me that not everything is about Physics. Their endless encouragement has been much needed and invaluable to me.

Finally, and perhaps most importantly, to my family - they have supported me through my entire academic career despite not truly knowing what I do. There are no words that can truly express how appreciative and grateful I am for them.

Chapter 1

Introduction

The study of light, matter and their interaction is one of the oldest and most fundamental problems in Physics. In the modern era, the best description of this interaction is quantum electrodynamics (QED); an elegant theory that presents light and matter as excitations of all-pervasive fields. QED is one of the most precise and well-tested physical theories to date, for example, the agreement of the fine structure constant, $\alpha \approx {}^{1}/_{137}$, between experiment and theory to a precision of less than one part per billion [1]. Results in QED are typically obtained using perturbative methods, summing the contributions from successively higher order Feynman diagrams (a useful technique for diagrammatically producing a series expansion in the aforementioned constant α, the coupling constant of QED), with these higher order terms providing radiative and self-energy corrections for instance. However, in the presence of strong background electromagnetic fields ($\sim 1 \times 10^{16}\,\mathrm{V\,cm^{-1}}$), it is no longer possible to perform such an expansion and the expansion becomes all-order in α. This presents a major difficulty in theoretical investigations of non-perturbative, or strong-field, QED (SFQED) and so, various approximation frameworks have been developed to extract more tractable solutions [2]. Environments where such intense fields occur are of prominent interest, for instance, within the fields of magnetars [3, 4, 5], in aligned crystals [6], in the dynamics of plasmas produced by intense laser pulses [7, 8], and at the interaction point of next-generation particle colliders [9], therefore, accurate theoretical predictions are invaluable, particularly for field strengths currently unattainable in a laboratory.

Hence, in order to both validate the results from theory as well as the applicability and accuracy of the approximation frameworks, experimental investigation of QED in intense fields is vital. With advancements in modern technology, probing the non-perturbative regime of QED is becoming more feasible. In particular, the development of chirped pulse amplification (CPA) [10] has allowed lasers to reach unprecedented intensities [11], with next-generation facilities anticipating even higher intensities using PW-class systems [12]. With this advancement, there has been an invigorated interest in investigating strong-field QED within a laboratory, using these ultra-intense lasers as the source of the extreme background fields. The E-144 experiment at SLAC in 1996 [13, 14], which utilised a 46.6 GeV electron beam and a laser beam achieving peak intensities of $\sim 1 \times 10^{18}\,\mathrm{W\,cm^{-2}}$, is considered the pioneering SFQED experimental campaign which successfully observed non-linear Compton scattering and Breit-Wheeler pair production within the perturbative regime. Since then, multiple experiments have been performed with similar configurations, using electrons generated via laser wakefield acceleration (LWFA) in plasmas as well as conventional accelerators, investigating quantum effects on the radiation of accelerating charges and others [15, 16, 17, 18]. As E-144 only probed the perturbative regime of SFQED, two experiments, SLAC E-320 [19] and LUXE [20, 21], aim to follow the success of E-144 and not only demonstrate the perturbative regime, but also observe the transition to the non-perturbative regime of SFQED experimentally for the first time.

As well as needing development of the technology to produce the intense interaction regions required to probe SFQED, these experiments also require advanced detector systems which can reliably function within these environments [22, 23]. Not only is there a large dynamic range for particle rates, but there is also typically a substantial background, necessitating detectors which can survive such radiation intense environments while maintaining ability to resolve signal. Hence, much work has been done to develop and improve detection systems for use, particularly within the context of E-320 and LUXE [24, 25, 26].

In this thesis, we discuss the operating principles of two novel-type detector systems, which are designed to extract the energy spectrum and spatial profile of high-energy, high-flux photon beams. Their application to the specific case of LUXE is also considered, highlighting the significance of their utility for future SFQED experiments. The thesis has the following structure: a summary of SFQED theory is highlighted in Chapter 2, with details on particular processes (Compton scattering, Breit-Wheeler pair production, radiation reaction and elastic photon-photon scattering) given. A discussion of the interaction of particle beams with solid targets for the purpose of generating photon and lepton beams is also provided. As the work on this thesis has been motivated by particular upcoming experiments, these are also discussed in Chapter 3 with an emphasis on their scope and expectations. Additionally, the numerical and simulation toolkits used to produce the results presented in this thesis are also detailed. Chapter 4 describes the operating principles of the gamma ray spectrometer, along with numerical modelling and testing as well as an experimental implementation. An approach to determine laser intensity using Compton-scattered photon beams is presented in Chapter 5, detailing the theoretical justifications of such a method and numerical examples of extracting this information. In Chapter 6, improvements to a previous experimental setup to investigate linear Breit-Wheeler pair production and elastic photon-photon scattering are presented using numerical modelling to provide estimates on the experimental running requirements in order to obtain sufficient statistics of these rare events. Finally, Chapter 7 discusses the outlook of the work presented here and potential avenues of further development.

Throughout, natural units are assumed such that $\hbar = c = 1$ and so $e = \sqrt{4\pi\alpha}$ is the fundamental charge. Additionally, the Minkowski metric is used with the signature $g_{\mu\nu} = \mathrm{diag}(+1, -1, -1, -1)$. Four-vectors are notated without indices unless stated for emphasis with three-vectors indicated in bold, e.g. $a = a^{\mu} = (a^0, \boldsymbol{a})$.

Chapter 2

Theory

2.1 Outline of Strong-Field QED

Strong-field quantum electrodynamics is a theoretical framework which can be used to describe the interaction of electrons, positrons and photons with strong, background fields [2, 27]. To define a "strong field", the usual Dirac Lagrangian from quantum electrodynamics is taken, with the field A_μ separated into two components - A_μ, a gauge field which describes photons, and $\mathcal{A}_\mu$, an external background field [28]:

$$\mathcal{L} = \bar{\Psi}(i\not{\partial} - m)\Psi - e\bar{\Psi}(\not{A} + \not{\mathcal{A}})\Psi - \frac{1}{4}F^2, \tag{2.1}$$

where ∂_μ is the four-gradient operator, γ_μ are the Dirac matrices with the Feynman notation $\not{b} = \gamma \cdot b$, Ψ is the fermion wavefunction with $\bar{\Psi}$ its conjugate and $F_{\mu\nu} = \partial_\mu A_\nu - \partial_\nu A_\mu$ is the electromagnetic field tensor associated with the gauge field. e and m are the fermion charge and mass respectively. With this separation, and the absence of an F^2-like term for $\mathcal{A}$, the external field is treated classically as a solution of Maxwell's equations. Rearrangement of Eq. (2.1) results in

$$\mathcal{L} = \bar{\Psi}\left[i(\not{\partial} + ie\not{\mathcal{A}}) - m\right]\Psi - e\bar{\Psi}\not{A}\Psi - \frac{1}{4}F^2, \tag{2.2}$$

which leads to a dressed propagator including the presence of the external field in the square brackets. The separation of the field in this form and introducing the dressed propagator in Eq. (2.2) is known as the Furry picture [29]. The result of the Furry picture is that methods for calculating S-matrices and hence probability rates or cross sections, for instance the Feynman rules, in SFQED can be done by replacing the fermion propagator in usual QED calculations with the dressed propagator. One non-trivial case where the propagator, or equivalently the Dirac equation, can be solved for exactly is in a plane wave background. For a plane wave of the form $A = A(\varphi)$ where $\varphi = k \cdot x$ is the wave phase with wave four-vector, k, and at four-position, x, the solution to the Dirac equation produces the well-known Volkov states

$$\Psi_p(x) = \left[1 + \frac{e\not{k}\not{A}}{2k \cdot p}\right]\frac{u(p)}{\sqrt{2p_0}}\mathrm{e}^{iS}, \qquad S = -p \cdot x - \int_{-\infty}^{\varphi}\left[\frac{ep \cdot A(\phi)}{k \cdot p} - \frac{e^2 A(\phi)^2}{2k \cdot p}\right]\mathrm{d}\phi\,, \tag{2.3}$$

where $u(p)$ is a constant Dirac bispinor and S coincides with the classical action of a charged particle of momentum p in an electromagnetic field [30]. The Volkov solutions are used ubiquitously for calculating probability rates and cross sections within SFQED [27, 31, 32].

Interactions within the scope of SFQED are quantified using two key parameters: the classical non-linearity or normalised potential a_0 (also commonly called ξ or η in literature); and the quantum parameter, χ, which are defined as [27, 33]

$$a_0 \equiv \frac{|e|\sqrt{-A^2}}{m} = \frac{\boldsymbol{p}_\perp}{m}, \qquad \chi \equiv \frac{|e|\sqrt{(p_\nu F^{\mu\nu})^2}}{m^3} = \frac{\gamma}{E_{\mathrm{cr}}}\sqrt{(\mathbf{E} + \mathbf{v} \times \mathbf{B})^2 - (\mathbf{v} \cdot \mathbf{E})^2}, \tag{2.4}$$

where $|e|$ is the elementary charge and m is the electron mass. The first term for each parameter in Eq. (2.4) gives a gauge and Lorentz invariant definition for the parameters in terms of the field, A, the corresponding electromagnetic field tensor, $F^{\mu\nu} = \partial^\mu A^\nu - \partial^\nu A^\mu$, and the particle's four-momentum, p. The second equality in each of Eq. (2.4) provide a more conceptual definition of these key parameters involving the electric and magnetic components of the background field, $\boldsymbol{E}$ and $\boldsymbol{B}$; a_0 can be seen to be proportional to the quiver momentum transverse to the field's propagation, $\boldsymbol{p}_\perp$, of the particle in the field and is an indication of how relativistic this motion is. Additionally, a_0 describes the multiplicity of the interaction with the background field, i.e. multiphoton effects on processes, as tree-level processes typically scale as a_0^2 at leading order, for $a_0 \gg 1$. This provides the definition of a strong field - if multiphoton effects are important and the particle effectively interacts with a large number of photons from the background field without depleting its energy, the field can be described classically and so the Furry picture prescription applies. Hence, a strong field is defined as a field such that $a_0 \gg 1$ and these multiphoton, or non-linear, effects are non-negligible. In this regime, the probability of interacting with n background photons scales as a_0^{2n}.

The quantum parameter χ, being proportional to the field, has the interpretation of being the work done by the external field in moving the particle a distance of the Compton wavelength, $\lambda_C = {}^1\!/_m$, in its rest frame, in units of a critical field strength, E_{cr}. The connection between the quantum nature of the interaction and χ, as well as the definition of the critical field E_{cr}, can be derived from work by Sauter, Heisenberg and Schwinger [34, 35, 36], by considering the generation of electron-positron pairs in a constant electric field, named the Schwinger effect. Heuristically, an electron-positron pair can be extracted from the negative energy Dirac sea in a vacuum by a constant, external electric field, $\boldsymbol{E}$, if it is sufficiently strong to separate the virtual charges by a distance λ_C, hence producing a real pair. The probability rate (per unit volume) for generation of these pairs has been found through various approaches to be [34, 36, 37]

$$W = \frac{2e^2E^2}{(2\pi)^2}\sum_{n=1}^{\infty}\frac{1}{n^2}\exp\left(-n\pi\frac{m^2}{eE}\right). \tag{2.5}$$

The exponent provides the definition of the critical field strength, known as the Schwinger limit, $E_{\text{cr}} \equiv {}^{m^2}\!/_e = 1.32 \times 10^{16}\,\text{V}\,\text{cm}^{-1}$. From Eq. (2.5), pair production in a static electric field is exponentially suppressed for $E \ll E_{\text{cr}}$; in the opposing limit, pair production increases quadratically with increasing E. Evidently, the ratio ${}^E\!/_{E_{\text{cr}}}$ is a heuristic measure of the quantum nature of the background field.

Furthermore, for a plane wave background with wavevector $\boldsymbol{k} = \omega_0\hat{\boldsymbol{n}}$, the magnetic field is orthogonal to the electric field and propagation direction as $\boldsymbol{B} = \hat{\boldsymbol{n}} \times \boldsymbol{E}$, which gives a quantum parameter of $\chi = {}^{\gamma E}\!/_{E_{cr}}(1 - \cos\theta)$, where θ is the angle between the wavevector and the particle's velocity. Hence, $\chi \sim {}^{E^*}\!/_{E_{cr}}$ where E^* is the magnitude of the electric field as seen in the particle's rest frame. Therefore, $\chi \sim 1$ implies that the field strength in the particle's rest frame is of the same order as the Schwinger limit and quantum effects on its dynamics are important.

[2, 12, 38] provide comprehensive reviews of the currently accessed areas of (a_0, χ) parameter space in laser-particle experiments at various facilities, as well as potential capabilities of future

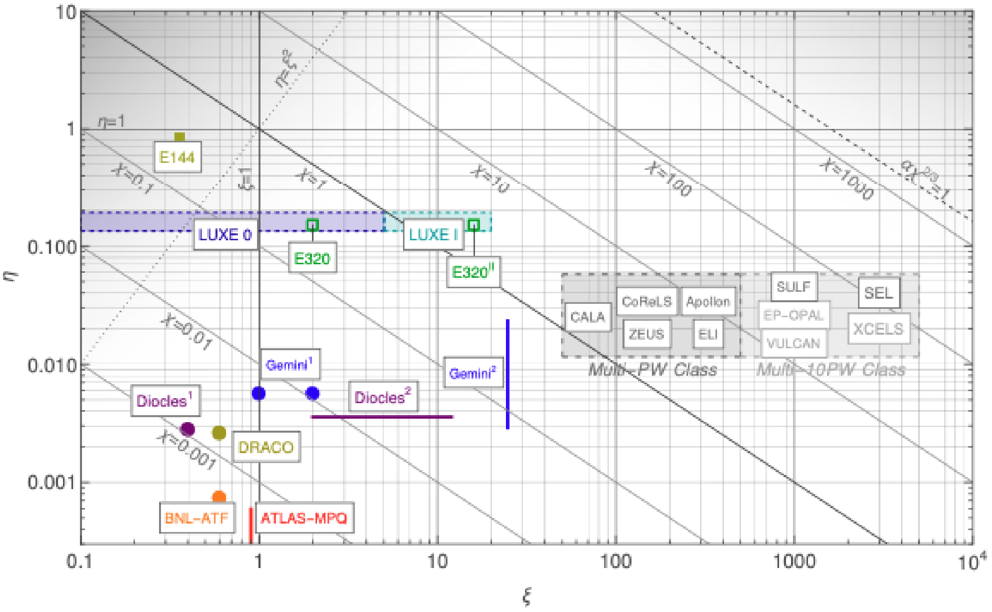

Figure 2.1: Map of current and planned SFQED experiments in $(a_0, \eta \approx {}^{\chi}/_{a_0})$ parameter space. Solid lines and markers represent reported experimental results and dashed lines and empty markers indicate future experiments. Reproduced from [2] under the terms of the Creative Commons CC-BY license.

generation laser facilities. Figure 2.1 has been taken from [2], which visualises the experimental landscape of SFQED investigations, using the parameters ξ (a_0) and η which is defined such that in a plane wave background, $\chi = \eta a_0$. This map shows that current results have been able to successfully probe the multiphoton regime with $a_0 \lesssim 25$. However, the quantum regime where $\chi \gg 1$ has not been well-explored, with only one previous experiment achieving $\chi \sim 0.5$ [13, 14], and on-going/upcoming experiments E-320 and LUXE proposed to reach χ of a few. Next generation lasers, particularly future exawatt-scale facilities, will be able to provide conditions that are both strongly multiphoton and far into the quantum regime, potentially reaching the Ritus-Narozhny limit where $\alpha\chi^{2/3} \gtrsim 1$ [39].

Determining the rates for SFQED processes involves the evaluation of multidimensional integrals which have the general form

$$\mathrm{R} \sim \int \prod_i \frac{\mathrm{d}^4 p_i}{(2\pi)^4} |S|^2, \tag{2.6}$$

where $|S|^2 = S^\dagger S$ is the square of the S-matrix for a particular process and $S^\dagger$ denotes its Hermitian conjugate. These integrals are often intractable for arbitrary background fields, however some field configurations provide analytical solutions, for instance a monochromatic plane wave background [40, 41]. Therefore, specific approximations are often made in order to extract useful results from Eq. (2.6). Currently, there are two main approximation frameworks employed in the literature of theoretical investigations of QED; the Locally Constant Field Approximation (LCFA) [42, 43] and the Locally Monochromatic Approximation (LMA) [2].

The locally constant field approximation, also called the constant crossed field (CCF) approximation, is the most widely utilised due to its wide applicability [44]. The fundamental approach to the LCFA is to assume that the probability rate for a process can be determined by taking the field locally as a constant, crossed field and integrating over this local rate. A constant, crossed field is one such that $\boldsymbol{E} \perp \boldsymbol{B}$ and $\boldsymbol{E}, \boldsymbol{B}$ have constant and equal magnitude, - one such configuration is a plane wave, which can be described by two Lorentz invariant parameters, a_0 and χ. The framework of the LCFA then allows for probability rates to be "built up" from contributions of these local rates, which are given by the results for a plane wave background. Such an approximation requires: (a) that $a_0 \gg 1$, and (b) that the probe particle is ultrarelativistic, which ensures that the higher order field invariants are negligible compared to χ as in a plane wave where the higher order invariants are identically zero. These assumptions are rather general, and in particular do not depend on the specific structure of the field, making the LCFA particularly useful is cases where the background field is unknown a priori, such as in laser-plasma particle-in-cell (PIC) simulations [38, 45]. Further, since the LCFA is so ubiquitous, substantial effort has been made to increase its range of validity and accuracy [46, 47].

A disadvantage of the LCFA is that, for $a_0 \sim O(1)$, it fails to capture spectral effects such as harmonics which arise due to interference of different points of the field. Instead, by describing the background field as a many-cycle pulse, these interference effects can be accounted for. The locally monochromatic approximation then combines two established approximations: that the temporal envelope of the field is slowly varying with respect to some "slow" time-scale; and that the resulting integrals can be expanded in terms of an interference phase [2, 48]. Since the LMA has stricter requirements than the LCFA framework, the LMA is better suited for interactions where the incident particle and laser beams are well-characterised. Moreover, these harmonic features in spectra that the LCFA fails to capture appear for $a_0 \sim O(1)$, which corresponds to the intermediately non-linear regime. For high intensities, $a_0 \gg 1$, the LMA rates tend to those calculated under the LCFA. As the LMA is derived from a construction of the global probability from local rate like the LCFA framework, it can be easily implemented in particle simulation codes of both a PIC and Monte-Carlo (MC) nature.

2.2 Laser-Particle Interactions

2.2.1 Multi-photon Compton Scattering

When a charged particle moves in a background field, it can absorb energy and momentum from the field and then go on to emit a single photon. In standard linear QED, the process of a charged particle, henceforth assumed to be an electron for brevity, absorbing and then re-emitting a photon is inverse Compton scattering, where the recoil due to emission results in an inelastic scattering of the photon. Due to the dressed states, (2.3), in the presence of the background field, rather than a one-to-one absorption/emission, the electron can effectively absorb multiple photons from the field, hence this process is named multi-photon or non-linear Compton scattering (NLCS).

For a plane wave background, multi-photon Compton emission can be described using the Volkov states Eq. (2.3). In this case, where the background has a constant wave four-vector k, the non-linear Compton emission of a single photon with momentum k' satisfies the momentum conservation

$$q + \ell k = q' + k', \tag{2.7}$$

where ℓ is some integer. In more general fields, ℓ can take on non-integer values. Instead of the (canonical) momentum of the electron, p, the time averaged kinetic momentum $\langle p - eA \rangle$ appears in the conservation equation due to the presence of the background field. This quantity is the quasimomentum of the electron, q, and is defined as

$$q_\mu = p_\mu - \frac{m^2 a_0^2}{2k \cdot p} k_\mu \tag{2.8}$$

in a plane wave. The square of the quasimomentum gives the effective mass of the electron, $q^2 \equiv m_*^2 = m^2(1 + a_0^2)$, showing that the presence of the background field enhances the rest mass of the electron; in the absence of a background field, $m_\star \to m$.

From Eq. (2.7), the energy of the emitted photon for a given ℓ is given by

$$\omega' = \frac{\ell k \cdot p}{p \cdot n' + \left(\ell + \frac{m^2 a_0^2}{4p \cdot k}\right) k \cdot n'}, \tag{2.9}$$

where $k'_\mu = \omega' n'_\mu$ and $(n')^2 = 0$. The dependency on the value of ℓ shows that the emitted photons form harmonics, ω'_ℓ, with the effective harmonic order $\ell_{\text{eff}} \sim a_0^3$ representing the number of photons absorbed from the background field [27]. Additionally, as ℓ is an integer in the case of a plane wave background, [40, 49] show that the emission rate can be expanded as a sum over these harmonics involving Bessel functions, $J_\nu(z)$. For example, in a circularly polarised wave, the emission rate is given by

$$W = \frac{e^2 m^2}{4q_0} \sum_{\ell=1}^{\infty} \int_0^{u_\ell} \frac{\mathrm{d}u}{(1+u^2)} \left[-4J_\ell^2(z) + a_0^2 \left(2 + \frac{u^2}{1+u}\right) \left(J_{\ell+1}^2(z) + J_{\ell-1}^2(z) - 2J_\ell^2(z)\right) \right], \tag{2.10}$$

where $u_\ell = 2\ell(k \cdot p)/m_*^2$ and $z = 2\ell m^2 \sqrt{\nu(1-\nu)} \left({}^{a_0}/\!_{\sqrt{1+a_0^2}} \right)$ and $\nu = u/u_\ell$. q_0 is the time-component of the four-vector q. In the limit of small a_0, the contribution of the partial emission rate is $W_\ell \sim a_0^{2\ell}$ and so for $a_0 \ll 1$, the emission rate can be approximated by the $\ell = 1$ term only:

$$W \simeq \frac{e^2 m^2 a_0^2}{4p_0} \left[\left(1 - \frac{4}{u_0} - \frac{8}{u_0^2}\right) \ln(1+u_0) + \frac{1}{2} + \frac{8}{u_0} - \frac{1}{2(1+u_0)^2} \right], \tag{2.11}$$

where $u_0 \approx {}^{2k \cdot p}/_{m^2}$. With the correct replacement of a_0 by the normalised four-potential for a single photon of energy ω, $a_0^2 \to {}^{4\pi e^2}/_{m\omega}$, Eq. (2.11) reproduces the Klein-Nishina formula for the linear (single-photon) Compton scattering cross section [49]

$$\sigma = 2\pi\alpha^2\lambda^2 \frac{1}{x} \left[\left(1 - \frac{4}{x-1} + \frac{8}{(x-1)^2}\right) \ln x + \frac{1}{2} + \frac{8}{x} - \frac{1}{2x^2} \right], \tag{2.12}$$

where $x \equiv {}^{s}/_{m^2}$ and $\sqrt{s}$ is the centre-of-momentum or zero-momentum-frame (ZMF) energy.

The opposing limit, $a_0 \gg 1$, can be obtained directly from Eq. (2.10), however an alternative approach is detailed in [49]. From its definition in a plane wave, $a_0 = {}^{eF}/_{m\omega}$, where $F^2 = F^{\mu\nu}F_{\mu\nu}$ is the field amplitude and ω is the energy (frequency) of the plane wave. Hence, a_0 can be made larger by decreasing ω, and the limit $a_0 \to \infty$ corresponds to a constant, crossed background field. As the total emission intensity is an Lorentz invariant, it can depend only on invariant combinations of $F_{\mu\nu}$ and p_μ; this restriction results in the three independent and dimensionless invariants:

$$\begin{cases} \chi &= \frac{e}{m^3}\sqrt{-(F_{\mu\nu}p^\nu)^2}, \\ f &= \frac{e^2}{m^4}F^2, \\ g &= \frac{e^2}{m^4}\epsilon_{\lambda\mu\nu\rho}F^{\lambda\mu}F^{\nu\rho}. \end{cases} \tag{2.13}$$

where $\epsilon_{\lambda\mu\nu\rho}$ is the Levi-Civita permutation symbol, and χ is the same quantum parameter as defined previously in Eq. (2.4). In the ultrarelativistic regime, $f, g \ll \chi^2$ for arbitrary fields and in a crossed field $f = g = 0$ exactly, hence χ is the important parameter to describe emission rates. Furthermore, as χ is an invariant, the determination of the emission rate for a crossed field will equivalently apply to any constant field and vice versa. Therefore, the $a_0 \gg 1$ limit can be obtained by considering the emission rate for a constant magnetic field as the background; this corresponds to the phenomenon of synchrotron radiation, and hence, the crossed field limit is also referred to as the synchrotron limit. Expressed in terms of χ, the spin and polarisation averaged synchrotron emission rate is given by [33, 43, 32]

$$\frac{\mathrm{d}W}{\mathrm{d}\omega'} = \frac{\alpha}{\sqrt{3}\pi\gamma^2}\left[\left(1 - x + \frac{1}{1-x}\right)K_{2/3}(\zeta) - \int_\zeta^\infty K_{1/3}(y)\ \mathrm{d}y\right], \tag{2.14}$$

where $\zeta = {}^{2x}/_{3\chi(1-x)}$, $\omega' = x\gamma m$ and $K_\nu(z)$ are the modified Bessel (MacDonald) functions [50]. The emission rate Eq. (2.14) has the useful asymptotic forms for $\chi \ll 1$ and $\chi \gg 1$:

$$\frac{\mathrm{d}W}{\mathrm{d}\omega'} \sim \begin{cases} \frac{5\chi}{32\sqrt{3}\pi^2}, & \chi \ll 1, \\ \frac{7\Gamma(\frac{2}{3})}{54\pi}(3\chi)^{\frac{2}{3}}, & \chi \gg 1, \end{cases} \tag{2.15}$$

where $\Gamma(z)$ is the gamma function.

The above conditions on χ, f, g and $a_0 \gg 1$ additionally detail the requirements for the valid use of the LCFA to calculate emission rates within arbitrary background fields. Figure 2.2 depicts the simulated energy spectra of emitted photons after the interaction of a 10 GeV electron

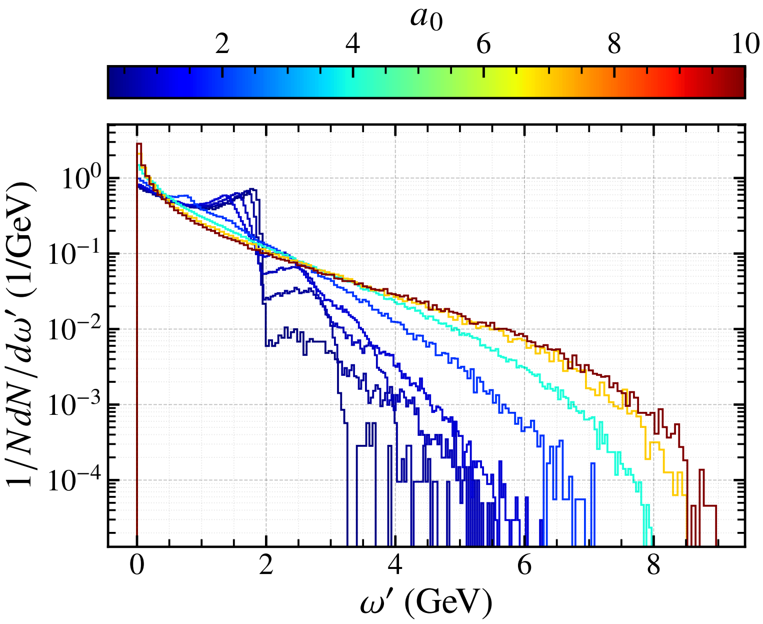

Figure 2.2: Energy spectra of Compton scattered photons during the interaction of a 10 GeV electron beam (with 10‰ energy spread) and a plane wave laser background of wavelength $\lambda = 800$ nm and varying normalised field amplitude, a_0.

beam with a plane wave background with $\omega = 1.55$ eV ($\lambda = 800$ nm) for various field amplitudes. For $a_0 \ll 1$, the standard Compton-like spectra can be seen with different harmonics (Eq. (2.9)) appearing and the synchrotron limit is also seen for $a_0 \gtrsim 5$, where the LCFA also becomes more accurate.

The angular distribution of the emitted photons within a plane wave background depends on polarisation of the field, however its main characteristic is that it is highly directional along the direction of the electron's initial momentum. For a linearly polarised field, in the case that $a_0 \gg 1$, emission occurs predominantly within an elliptical cone whose size is $\theta \sim {}^{a_0}/_{\gamma}, {}^{1}/_{\gamma}$ parallel and perpendicular to the polarisation direction respectively.

Assuming a head-on collision between the electron and the plane wave field, Eq. (2.9) can be written in the form [51, 52]

$$\omega'_\ell \simeq \frac{4\ell\gamma^2\omega}{1+\gamma^2\theta^2+2\ell\eta+a_0^2} \simeq \frac{4\ell\gamma^2\omega}{1+\gamma^2\theta^2+(2\chi+1)a_0^2}, \tag{2.16}$$

where $\eta = {}^{\chi}/_{a_0} = {}^{2\gamma\omega}/_{m}$, θ is the scattering angle between the incident electron and emitted photon, and the scaling $\ell_{\mathrm{eff}} \simeq a_0^3$ has been used in the denominator. In the limit $\theta \to 0$, the emitted photon energy reaches a peak, which assuming $\chi \ll 1$, is given by

$$\omega'_\ell \simeq \frac{4\ell\gamma^2\omega}{1+a_0^2}. \tag{2.17}$$

In the case of $\ell = 1$, the harmonic is designated as the Compton edge, which corresponds to the linear QED Compton edge for $a_0 \to 0$, where the scattered frequency is the Doppler-shifted result of a relativistic mirror $\omega' \to 4\gamma^2\omega$ [53]. The scaling of the denominator in Eq. (2.17) is the same as m_*^2, hence this redshifting of the Compton harmonic due to the increasing strength of the background field can be attributed to the increase in the effective mass of the electron; reducing the (linear) Compton edge. This redshifting of the Compton edge is also visible in Fig. 2.2 for $a_0 \lesssim 2$, where the first order edge can be seen to be moving to lower energy with increasing a_0 as predicted by Eq. (2.17).

Furthermore, in the $\chi \ll 1$ regime where quantum effects can be neglected, the number of Compton scattered photons emitted per laser cycle per incident electron is given by

$$N_\gamma \sim \begin{cases} 1.53 \times 10^{-2} a_0^2 & a_0 < 1, \\ 3.31 \times 10^{-2} a_0 & a_0 \gg 1. \end{cases} \tag{2.18}$$

Considering Eqs. (2.9) and (2.18), in the linear regime where $a_0 < 1$ and so $\ell \sim \lceil a_0^3 \rceil = 1$, the energy of the emitted photons scales as $\omega' \propto \gamma^2\omega$ with $N_\gamma \propto a_0^2$. At high intensities where $a_0 \gg 1$, $\omega' \sim \gamma^2 a_0 \omega$ and $N_\gamma \propto a_0$, a high-energy and high-yield photon source can be generated readily in the non-linear regime. As an example, a 15 GeV electron beam containing a charge of 250 pC interacting with a counter-propagating laser of $\omega = 1.55$ eV ($\lambda = 800$ nm) and $a_0 = 2$ over 10 laser cycles provides $\sim 10^9$ Compton scattered photons with harmonics up to ~ 10 GeV.

2.2.2 Non-linear Breit-Wheeler Pair Production

In linear QED, the process of pair production by two photons is related to the Compton scattering process via a crossing symmetry. For the $\ell = 1$ limit, which is equivalent to the interaction of two photons to produce an electron-positron pair, the cross section for the two-photon or linear

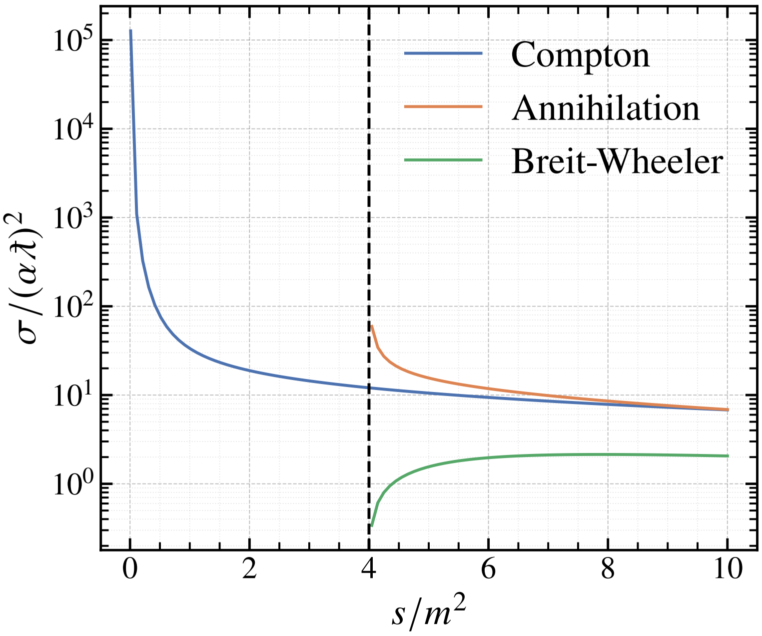

Figure 2.3: Comparison of the cross sections for processes as calculated in linear QED. Compton scattering (blue) is given by the Klein-Nishina formula Eq. (2.12); linear Breit-Wheeler (green) is given by Eq. (2.19) and electron-positron pair annihilation (orange) is related to Eq. (2.19) via a crossing symmetry from the s-channel to t-channel [49]. The energy threshold for pair production and annihilation is repesented by the dashed vertical line.

Breit-Wheeler (LBW) process is given by [54]

$$\sigma = \frac{\pi}{2}\alpha^2\lambda^2(1-\beta^2)\left[2\beta(\beta^2-2) + (3-\beta^4)\ln\frac{1+\beta}{1-\beta}\right], \tag{2.19}$$

where $\beta \equiv \sqrt{1 - {}^{4m^2}\!/_{s}}$.

This crossing symmetry also exists in the presence of a background field and results in the non-linear Breit-Wheeler pair production (NLBW), where an external photon in the background field absorbs sufficient energy and momentum from the field to effectively "split" into an electron-positron pair [55]:

$$e^{\pm} + \ell\omega \longrightarrow e^{\pm} + \gamma \qquad \text{(NLC)}, \tag{2.20}$$

$$\gamma + \ell\omega \longrightarrow e^{-} + e^{+} \qquad \text{(NBW)}. \tag{2.21}$$

Since an electron-positron pair is created, the Breit-Wheeler process has an energy threshold which significantly affects the resulting production rate in comparison to non-linear Compton scattering. This can also be seen in the linear limit of Eq. (2.19), where the cross section is only real for $\beta \geq 0$ or equivalently $\sqrt{s} > 2m$; the ZMF energy must be at least the rest mass energy of the pair. This results in a minimum value for the harmonic ℓ: $\ell_{\text{min}} = {}^{2m_*^2}\!/_{k' \cdot k} \leq \ell$, where k is the wavevector of the field and k' is the momentum of incident photon. This can be interpreted, in a plane wave background, as the minimum number of photons that are required to be absorbed from the background in order to produce the pair [56].

The production rate for NLBW has three distinct regimes of behaviour depending on the field amplitude a_0 and the photon quantum number χ_γ [2]. χ_γ is analogous to the (electron) quantum parameter, χ, defined in Eq. (2.4) but with the replacement $p \to k'$. For $a_0 \ll 1$, it is possible for a single background photon to satisfy the energy threshold and production is described by linear pair production due to the collision of two photons. A multiphoton regime for $a_0 \lesssim 1$ is also possible, whereby multiple $\ell \geq \ell_{\text{min}}$ photons are absorbed from the background. In both of these cases, the production rate scales similarly to NLCS with $W \sim a_0^{2\ell_{min}}$, with higher ℓ being suppressed due to $a_0 < 1$. For the strong field limit, $a_0 \gg 1$, a significant number of background photons can produce an electron-positron pair and the process is strongly non-linear. In this instance, the production rate also depends on the photon quantum parameter, χ_γ, as (in the case of a plane wave)

$$W \sim \begin{cases} \alpha \chi_\gamma \mathrm{e}^{-{}^{8}\!/_{3\chi_\gamma}} & \chi_\gamma \ll 1, \\ \alpha \chi_\gamma^{{}^{2}\!/_{3}} & \chi_\gamma \gg 1. \end{cases} \tag{2.22}$$

In the limit $\chi_\gamma \ll 1$, the production rate scales similarly to the Schwinger production process Eq. (2.5) due to the same quantum tunnelling nature of the process. Additionally, the strong suppression at small χ_γ emphasises that pair production is an inherently quantum process with no classical analogue. Hence, the production of electron-positrons pairs acts as a benchmark for the highly quantum regime of SFQED. In the opposite limit of large χ_γ, the production rate scales in the same way as NLCS, leading to the possibility of QED casades forming within extremely intense laser pulses.

2.3 Radiation Reaction

It is well-established that accelerating charges emit radiation. From a classical viewpoint, this is caused by the reconfiguration of the particle's own electromagnetic field as it moves; within a quantum description, the radiation is attributed to the emission of photons. In either case, there is a back-reaction of the radiation on the particle which results from the particle interacting with its own field (classical) or the recoil from the emission of a photon (quantum). This back-reaction is termed radiation reaction and a full, fundamental description of this phenomenon has still not yet been found. Within the regime of classical electrodynamics, Abraham and Lorentz formulated an equation of motion which includes a term for the reaction force by the radiation field, which was then generalised to a relativistically covariant form by Dirac, commonly referred to as the Lorentz-Abraham-Dirac (LAD) equation [57, 58, 59]:

$$\frac{\mathrm{d}u^\mu}{\mathrm{d}s} = \frac{e}{m}F^{\mu\nu}u_\nu + \frac{e^2}{6\pi m}\left[\frac{\mathrm{d}^2u^\mu}{\mathrm{d}s^2} + \left(\frac{\mathrm{d}u_\nu}{\mathrm{d}s}\frac{\mathrm{d}u^\nu}{\mathrm{d}s}\right)u^\mu\right]. \tag{2.23}$$

Here, u is the four-velocity of the particle, s is the proper time, e, m are the particle's charge and mass respectively, and $F^{\mu\nu}$ is the electromagnetic field tensor of the externally applied field. The first term in Eq. (2.23) is the usual Lorentz force and the second term accounts for the reaction of the particle's radiation field. Although Eq. (2.23) satisfies both Maxwell's and Lorentz's equations in a self-consistent manner, whereby the current found from the Lorentz equation of motion is in Maxwell's equations to determine the consequent self-fields, the second order derivative $\frac{\mathrm{d}^2u^\mu}{\mathrm{d}s^2}$ introduces problematic features in the solutions of the LAD equation. For instance, runaway solutions exist where the radiation reaction force exponentially increases with time, as well as pre-acceleration of the charge where momentum changes precede changes in the field. Alternative formulations for radiation reaction have been proposed in order to overcome the issues of the LAD equation. One of the most commonly used within classical electrodynamics was presented by Landau and Lifshitz, by reducing the order of the LAD equation [30]. If the radiation reaction forces are much smaller than the force exerted by the applied field, the acceleration, $\frac{\mathrm{d}u^\mu}{\mathrm{d}s}$, can be replaced by the usual Lorentz force in the radiation reaction term of Eq. (2.23). The resulting equation, referred to as the Landau-Lifshitz equation, is then first order in the particle's velocity and hence removes the pathological solutions associated with Eq. (2.23) [60];

$$\frac{\mathrm{d}u^\mu}{\mathrm{d}s} = \frac{e}{m}F^{\mu\nu}u_\nu + \frac{e^4}{6\pi m}\left[\frac{m}{e}(\partial_\lambda F^{\mu\nu})u^\lambda u_\nu + F^{\mu\nu}_{\nu\lambda}u^\lambda + (F^{\nu\lambda}u_\lambda)^2 u^\mu\right]. \tag{2.24}$$

By virtue of the reduction of order method, all physically meaningful solutions of the LL equation are also solutions of the LAD equation. For the reduction of order to be valid, the characteristic length, L, that the field varies over, and its magnitude, E, must satisfy the conditions $L \gg \alpha\lambda_C$ and $E \ll {}^{E_{cr}}/_{\alpha}$ in the instantaneous rest frame of the particle [27]. Within the regime of classical electrodynamics, these conditions are automatically met as they coincide with the requirements for neglecting quantum effects.

The LL equation permits an exact solution for the case of a particle moving in an external plane wave field. Following the notation of [33], for a field with potential $eA^\mu = ma_0 \sum\limits_i f_i(\varphi)\varepsilon_i^\mu$, where $f_i(\varphi)$ are the temporal envelopes of the pulse along each of the polarisation axes, $\varepsilon_1, \varepsilon_2$, the solution of Eq. (2.24) can be expressed concisely in light-front coordinates: $u^-, u^+, \mathbf{u}^\perp$. k^μ is the four-wavevector of the field and satisfies the light-like condition $k^2 = 0$. From Eq. (2.24), the solution for the light-front momentum, $mu^- = {}^{k\cdot p}/_{\omega_0}$, is [61]

$$u^-(\varphi) = \frac{u_0^-}{1 + \frac{2}{3}R_c I(\varphi)}, \qquad I(\varphi) = \int_{-\infty}^{\varphi}\left[f_1'(\psi)^2 + f_2'(\psi)\right]\,\mathrm{d}\psi\,. \tag{2.25}$$

The classical radiation reaction parameter is defined as [33] $R_c = {}^{a_0^2 u_0^- \omega_0}/_{m}$, and u_0^- is the initial light-front momentum. In particular, for an ultrarelativistic particle with $\gamma \gg 1$, $u^- \approx 2\gamma$ and

$$\gamma(\varphi) = \frac{\gamma_i}{1 + R\gamma_i}, \tag{2.26}$$

with $R = ({}^{4a_0^2\omega_0}/_{3m})I(\varphi)$ and γ_i is the initial gamma factor. The transverse light-front momenta are given as

$$\mathbf{u}^\perp = \frac{u^-}{u_0^-}\left[\mathbf{u}_0^\perp + a_0 f_{1,2}(\varphi) + \frac{2R_c}{3}H_{1,2}(\varphi) + \frac{2R_c}{3a_0}f_{1,2}'(\varphi)\right], \tag{2.27}$$

with $H_j(\varphi) = \int_{-\infty}^{\varphi} f_j'(\psi)I(\psi)\,\mathrm{d}\psi$ and the prime denotes differentiation with respect to the phase φ. The final light-front component can be determined from the on-shell condition

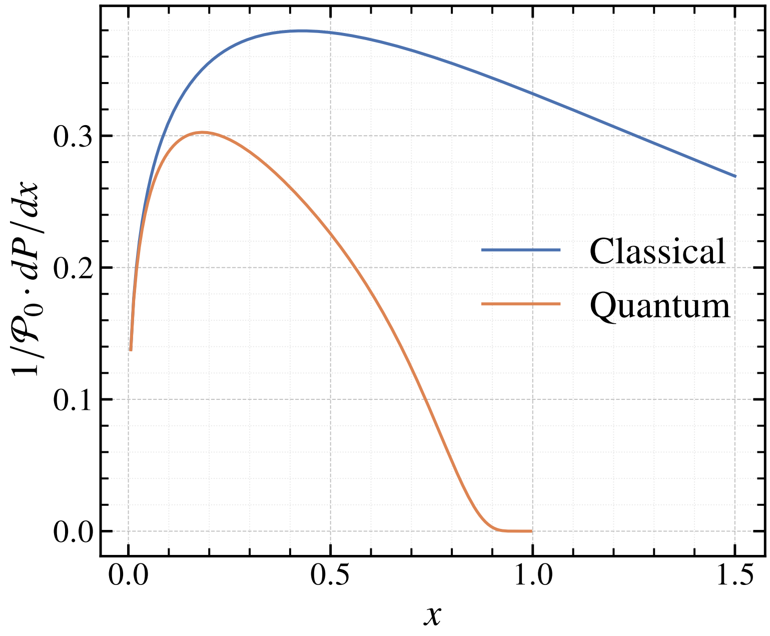

Figure 2.4: Classical (blue) and quantum (orange) spectra for $\chi = 2$, given by Eqs. (2.28) and (2.29) respectively.

$u^+u^- - \mathbf{u}^\perp \cdot \mathbf{u}^\perp = 1$.

The energy spectrum of the emitted radiation can be determined by considering the Larmor power as the charge accelerates in the external field [33, 55]. Viewing the instantaneous trajectory as a small arc, the emission exhibits the behaviour of synchrotron radiation in an instantaneously constant field. Using the parameter χ as previously defined in terms of the electric and magnetic fields, the classical emission spectrum in terms of the radiated energy $\omega = x\gamma m$ by an electron with parameter χ and Lorentz factor γ is [33, 30, 49]

$$\frac{1}{\mathcal{P}_0}\frac{dP_{cl}}{d\omega} = \frac{\sqrt{3}\omega}{2\pi(\gamma m)^2\chi^2}\left[2K_{2/3}(\zeta) - \int_{\zeta}^{\infty} K_{1/3}(y)\ \mathrm{d}y\right], \qquad \zeta = \frac{2x}{3\chi}. \tag{2.28}$$

with the total radiated power, $\mathcal{P}_0 = {}^2\!/\!{}_3\alpha m^2\chi^2$. As can be seen in Fig. 2.4, the classical emission spectrum has no upper cut-off in x, i.e. the emitted radiation can, in principle, be larger than the initial particle energy. This is obviously non-physical and is resolved by including quantum corrections to Eq. (2.28).

By considering the quantisation of the emitted radiation, as well as it's spin contribution, the emission spectrum takes the same form as Eq. (2.14)

$$\frac{1}{\mathcal{P}_0}\frac{dP_q}{d\omega} = \frac{\sqrt{3}\omega}{2\pi(\gamma m)^2\chi^2}\left[\left(1-x+\frac{1}{1-x}\right)2K_{2/3}(\zeta) - \int_{\zeta}^{\infty} K_{1/3}(y)\ \mathrm{d}y\right], \tag{2.29}$$

with $\zeta \rightarrow {}^{2x}/_{3\chi(1-x)}$. In the limit, $x \ll 1$, the classical form Eq. (2.28) is obtained. As shown in Fig. 2.4, the quantum emission spectrum has similar behaviour to the classical case for low x, where the emitted radiation carries only a small fraction of the particle's energy (momentum) and also has the correct upper bound where the radiation carries all of the particle's energy at $x = 1$. Furthermore, integration of Eq. (2.29) over emitted energy gives the total radiated power as [62]

$$\frac{\mathcal{P}_q}{\mathcal{P}_0} = \frac{9\sqrt{3}}{8\pi}\int_0^{\infty} \frac{8y\ \mathrm{d}y}{27({}^{2}/_{3}+\chi y)^3}\left[\int_y^{\infty} K_{5/3}(z)\ \mathrm{d}z + \frac{3}{2}\frac{\chi^2 y^2}{{}^{2}/_{3}+\chi y}K_{2/3}(y)\right] \equiv g(\chi), \tag{2.30}$$

which is the classical power scaled by a factor, $g(\chi)$, commonly referred to as the Gaunt factor. An analytical approximation to Eq. (2.30) which is accurate to within 2% for arbitrary χ was presented in [43],

$$g(\chi) \simeq \frac{1}{\left[1+4.8(1+\chi)\ln(1+1.7\chi)+2.44\chi^2\right]^{2/3}} \tag{2.31}$$

Hence, with a quantum description of the power spectrum, not only is there a corrected cut-off, but the instantaneous radiated power is reduced by a quantum multiplicative factor. Utilising a combination of the LL equation to describe motion between emission events, and the quantum corrected spectrum, Eq. (2.29), results in a "semiclassical" model of radiation reaction which is commonly used in simulations of electron-laser beam interactions and electron-plasma interactions both for benchmarking purposes and when a fully quantum description involving stochastic effects is not required.

A complete quantum model which also accounts for the stochastic nature of radiation emission produces a Fokker-Planck-type equation of motion involving emission operators. Incidentally, as the emission is no longer deterministic as in the classical and semiclassical models, it is possible for a single emission event to result in a large momentum change for the particle and hence the emitted photon carries a significant portion of the initial particle energy. signifying the breakdown of continuous radiation. The converse is also possible, where the particle does not radiate at all (quenching) or not significantly resulting in the particle reaching areas of phase space which would be classically forbidden (straggling) [33]. Moreover, the inclusion of stochastic effects produces a markedly different behaviour in the final particle energy spectrum compared to the (semi)classical model. While in both cases the mean particle energy decreases and, on average, more energetic particles radiate more, the width (variance) of the energy spectrum broadens in the stochastic quantum case but narrows in the (semi)classical case [63]. [64, 65, 66] attribute this to the diffusion term in the quantum Fokker-Planck equation of motion. The first and second moments of the energy distribution are shown to evolve as

$$\frac{\mathrm{d}\langle\gamma\rangle}{\mathrm{d}t} = -\frac{\langle g(\chi)\mathcal{P}_0\rangle}{m} \tag{2.32}$$

$$\frac{\mathrm{d}\sigma^2}{\mathrm{d}t} = -2\frac{\Delta\gamma g(\chi)\mathcal{P}_0}{m} + \frac{\langle S\rangle}{m^2}, \tag{2.33}$$

in the stochastic emission model, with $\Delta\gamma = \gamma - \langle\gamma\rangle$ and $\sigma^2 = \langle\Delta\gamma^2\rangle$ is the variance of the energy distribution. The evolution of $\langle\gamma\rangle$ in the semiclassical model is identically given by Eq. (2.32), while the first term in Eq. (2.33) describes the semiclassical evolution of σ^2. The second term in Eq. (2.33), which has opposite sign to the semiclassical term, is the diffusion contribution which counteracts the narrowing caused by classical emission. The function, S, is defined in [66] as

$$S(\chi) = \frac{55\alpha m^2}{24\sqrt{3}\lambda_c\eta}\chi^4 g_2(\chi), \tag{2.34}$$

where $g_2(\chi) \simeq \left[1 + (1 + 4.528\chi)\ln(1 + 12.29\chi) + 4.632\chi^2\right]^{-7/6}$ is the second Gaunt factor. The classical model without quantum corrections to the energy spectrum evolves in the same way as the semiclassical model but with $g(\chi) \to 1$. This comparison of the energy spectrum for the example of 500 MeV electrons colliding with a 40 fs laser pulse at $a_0 = 5$ is shown in Fig. 2.5.

The appropriateness of each model is dependent primarily on the parameter χ. For $\chi \ll 1$, the classical description of radiation reaction as a continuous force acting on the particle applies, with motion described by the LL equation. The quantum correction to the emission spectrum is applied when $\chi \lesssim 1$, reducing the radiated power and correcting the maximum fraction of energy

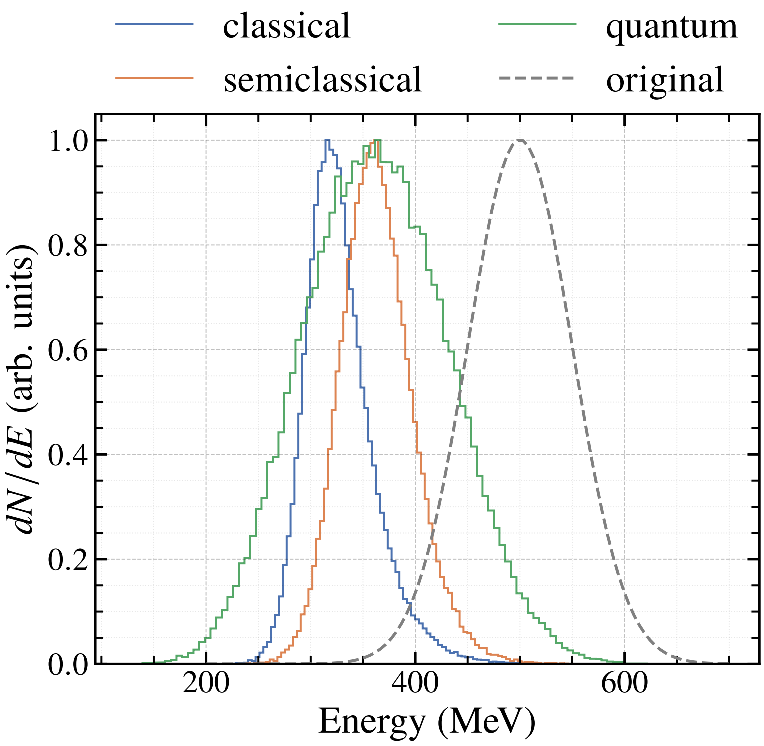

Figure 2.5: Simulated energy spectrum for electrons which radiate during the interaction of a pencil-like electron beam and a laser pulse. The electron beam has a central energy 500 MeV (10% RMS spread) and the laser pulse is modelled as Gaussian with $a_0 = 25$ and FWHM duration 30 fs.

that can be radiated. In the regime of large $\chi \gg 1$, the stochastic effects become important and in this case the full quantum model is required for an accurate description of the particle's dynamics as emission becomes a discrete, probabilistic process.

Despite the various models in different regimes, a completely resolved theory of radiation reaction remains unfound in part due to the experimental difficulties in detection. Recent developments in laser technology has reinvigorated investigations into radiation reaction, with intensities $\gtrsim 1\times10^{19}$ W cm^{-2} achieved routinely as an example. Such a laser was used in [17, 18] to investigate radiation reaction in an electron-laser beam interaction, with the high-energy (~2 GeV) electrons produced via LWFA at the Astra-Gemini facility. These campaigns demonstrated a successful measurement of the electron energy loss by radiation in a regime where $\chi \lesssim 1$. Interestingly, it was found that the semiclassical model provided the best match to the measured results, indicating that the fully stochastic regime had not yet been reached and that the influence of these effects on electron dynamics requires $\chi \gg 1$. This conclusion is also evidence that the reduced power emission is observable when χ is no longer non-negligible. One disadvantage of the setup in [17, 18] is that shot-to-shot fluctuations in the in initial electron beam make it difficult to compare the scattered and unscattered electron energy spectra. Some potential improvements are discussed in [67], including the contemporaneous measurement of the initial and scattered energy spectra.

An alternative scattering field, provided by the atomic and nuclear fields within an aligned crystal, was used in [68] and a 178.2 GeV positron beam from the Super-proton-synchrotron North Area facility at CERN. In this instance, a stochastic quantum model gave the best match to the experimental results, with emission spectra comparable to Eq. (2.29). However, both [18] and [68] discuss the limitations of Eq. (2.29) since it is derived under the assumptions of the LCFA which is not applicable for $a_0 \sim \mathcal{O}(1)$.

2.4 Elastic Photon-Photon Scattering

In classical electrodynamics, due to the linear nature of Maxwell's equations, electromagnetic fields do not interact with themselves. From a semiclassical viewpoint, the photon is uncharged and so is unaffected by the presence of electromagnetic fields. This is not the case in QED, where photons can scatter due to the production of virtual electron-positron pairs in vacuum as represented by the Feynman diagrams in Fig. 2.6. Using the standard results of QED, the cross section for this scattering process can be calculated, for example as done by [49, 69, 70].

An alternative approach involves constructing an effective field theory for the electromagnetic field [71]. The final term in Eq. (2.1) describes the non-interacting behaviour of electromagnetic fields and is expressed in terms of the electric and magnetic fields as $\mathcal{L}_0 = {}^1\!/\!{}_2(|\boldsymbol{E}|^2 - |\boldsymbol{B}|^2)$. Since the Lagrangian is quadratic in the fields, the resulting equations of motion (Maxwell's equations), determined by taking derivatives with respect to the fields, are linear in $\boldsymbol{E}$ and $\boldsymbol{B}$. By considering the change in the vacuum energy due to the presence of an electromagnetic field, corrections containing higher orders of the fields can be obtained; the lowest order correction in α for weak fields, $|\boldsymbol{E}| \ll E_{\mathrm{cr}}$, $|\boldsymbol{B}| \ll B_{\mathrm{cr}}$, is given by [28, 35, 72]

$$\mathcal{L}_1 = \frac{2\alpha^2}{45m^4}\left[(|\boldsymbol{E}|^2 - |\boldsymbol{B}|^2)^2 + 7(\boldsymbol{E}\cdot\boldsymbol{B})^2\right]. \tag{2.35}$$

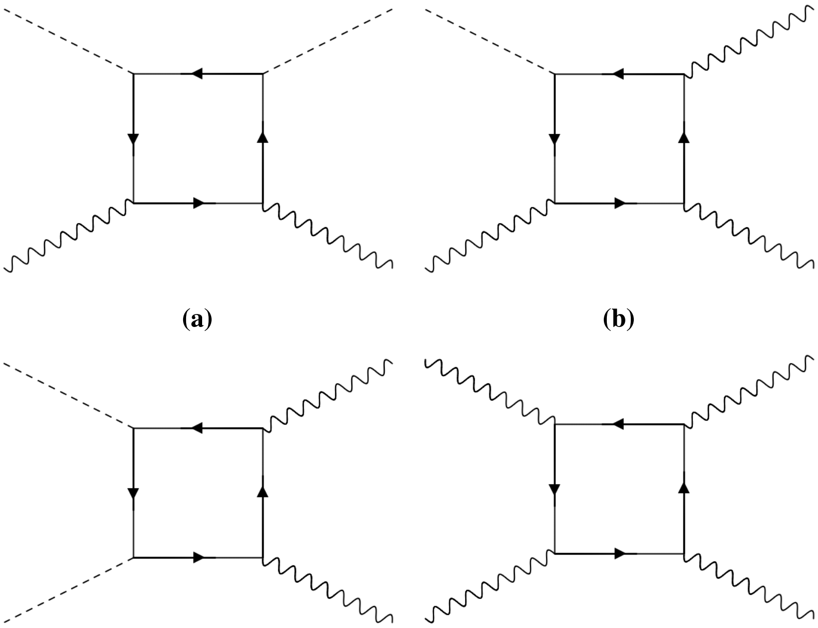

(a) (b)

(c) (d)

Figure 2.6: Lowest order Feynman diagram of two-photon scattering processes in vacuum: (a) stimulated or Delbrück scattering, (b) spontaneous scattering or photon splitting, (c) and (d) photon-photon scattering. Dashed lines represent virtual or background field photons and wavy lines represent real photons.

These non-linear terms describe the polarisation and scattering effects that arise from diagrams such as Fig. 2.6. Through standard QED techniques such as the LSZ reduction formula [73], the interaction terms, scattering matrix elements and corresponding cross section for photon-photon scattering can be derived from Eqs. (2.1) and (2.35). In the zero momentum frame (ZMF), each incident photon has energy ω, the total photon-photon scattering cross section in the low-energy limit $\omega \ll m$ has the form [49, 69, 70, 74]

$$\sigma_{\gamma\gamma} \simeq \frac{973\alpha^4\lambda^2}{10125\pi}\left(\frac{\omega}{m}\right)^6, \tag{2.36}$$

and $\sigma_{\gamma\gamma} \sim \omega^{-2}$ in the high-energy limit. The cross section, being proportional at lowest order to α^4 due to the four vertices in Fig. 2.6d, is extremely small, having a maximum value of $\approx 2\,\mu\mathrm{b}$ at $\omega \approx m$ (or ZMF energy $\sqrt{s} \approx 1\,\mathrm{MeV}$).

Due to the size of the cross section, the photon-photon scattering process has not yet been experimentally observed. Instead, upper bounds have been placed on the cross section at different ZMF energies for various interaction configurations such as all-optical dual beam [75, 77, 78], three beam [76] and four beam [84] configurations as depicted in Fig. 2.7. Additional theoretical

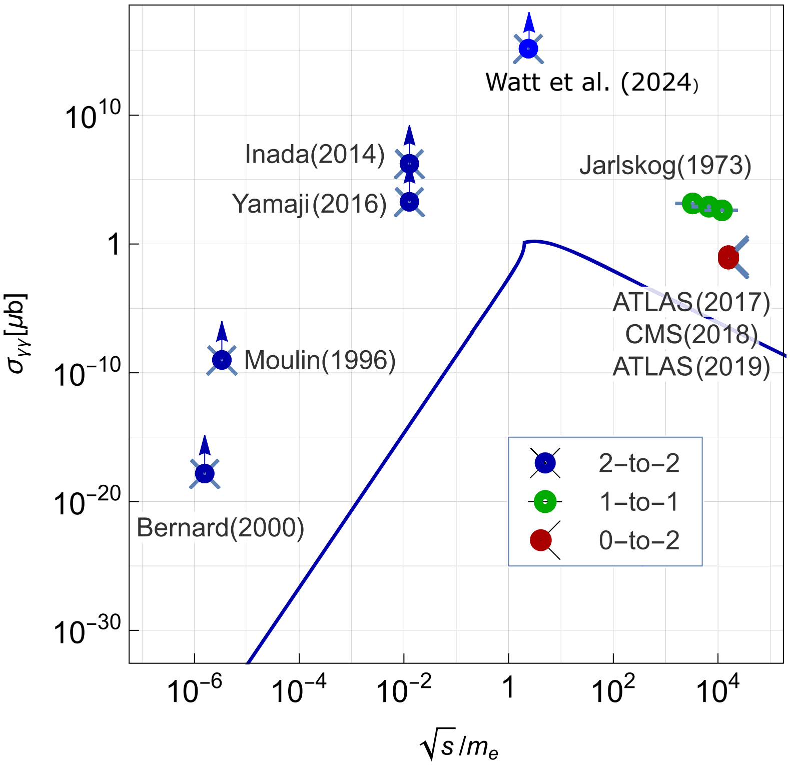

Figure 2.7: Dependence of the photon-photon scattering cross section on the ZMF energy. Also shown are experimental bounds on the value of the cross section from various experimental investigations [75, 76, 77, 78, 79, 80, 81, 82, 83]. Reproduced from [79] under the terms of the Creative Commons CC-BY license.

and numerical investigations into these configurations have been considered to improve the interaction rate [85, 86]. Figure 2.7 summarises these measurements from experiments, as well as experiments involving the collision of one or two virtual photons in the nuclear fields of heavy ions (Fig. 2.6c) [81, 82, 83]; stimulated/Delbrück scattering (Fig. 2.6a) [80]; and photon splitting (Fig. 2.6b) [80, 87].

In [79], an alternative approach is used involving a high-energy, broadband bremsstrahlung source generated by LWFA electrons, and a dense x-ray bath produced by laser-plasma ablation of a thin foil. This configuration accessed an effective ZMF energy of 1.11 ± 0.06 MeV, anticipating the maximum value for the scattering cross section. No direct observations of photon-photon scattering were made, however the closest upper bound on the cross section to date was made, within 10^{11} of the theoretical value.

2.5 Particle-Solid Interactions

As well as producing photons and electrons/positrons via non-linear Compton and Breit-Wheeler processes within a laser field, it is also possible to generate such particle beams using solid targets. Particularly, the generation of beams using the well-known bremsstrahlung and Bethe-Heitler pair productions processes is reviewed here.

2.5.1 Electron-Positron and Photon Generation

Within the field of a nucleus, the dominant interaction process for photons above 1 MeV is Bethe-Heitler pair production. In the unscreened ultrarelativisitic limit, the cross section for a photon of energy ω interacting with a target nucleus of atomic number, Z, is given by Bethe, Heitler and Maximon as [88, 89]

$$\frac{\mathrm{d}\sigma}{\mathrm{d}x} = 4Z^2\alpha r_e^2\left[x^2 + (1-x)^2 + \frac{2}{3}x(1-x)\right]\left[\ln\frac{2\omega x(1-x)}{m_e} - \frac{1}{2}\right], \tag{2.37}$$

where $\epsilon = x\omega$ is the energy of the outgoing electron/positron, and r_e is the classical electron radius, $r_e = {}^{\bar{\lambda}}/_{\alpha}$. Equation (2.37) is symmetric in the electron/positron energy as the Coulomb interaction with the nucleus is not accounted for. The total cross section is given by integrating $x \in [0, 1]$ to give

$$\sigma = \frac{28}{9}Z^2\alpha r_e^2\left(\ln\frac{2\omega}{m_e} - \frac{109}{42}\right). \tag{2.38}$$

Equation (2.38) is weakly dependent on photon energy and can be assumed to be approximately constant over small energy ranges. In the complete screening regime, valid for $\omega \gtrsim 1\,\mathrm{GeV}$, Eq. (2.37) becomes [90, 91]

$$\frac{\mathrm{d}\sigma}{\mathrm{d}x} = \frac{A}{N_A X_0}\left[1 - \frac{4}{3}x(1-x)\right]. \tag{2.39}$$

N_A is Avogadro's constant, X_0 is the radiation length of the target material in $\mathrm{g\,cm^{-2}}$, with $X_0^{-1} \sim \alpha Z^2 r_e^2 N_A A^{-1}$ and A is the atomic number of the target. In this regime, the total cross

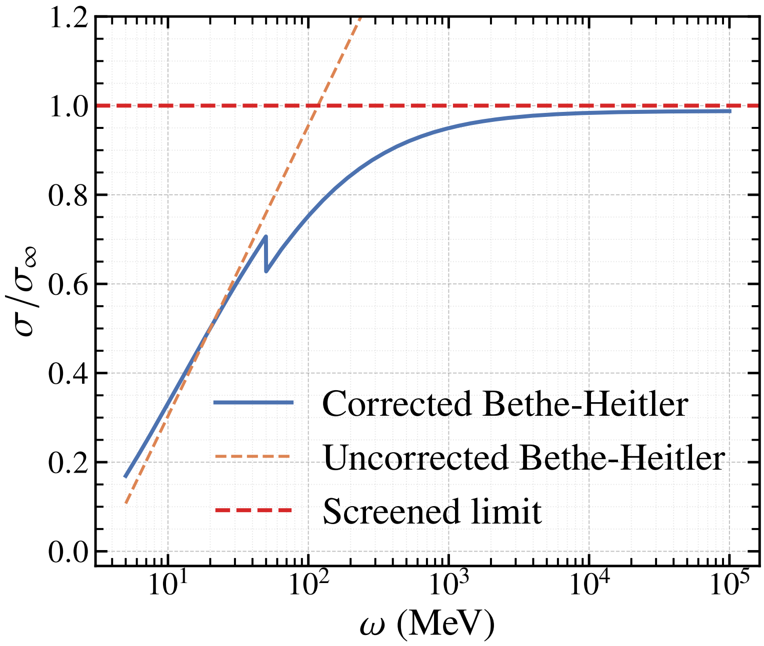

Figure 2.8: Total cross section for Bethe-Heitler pair production as a function of photon energy for $Z = 74$. The corrected cross section model used within the simulation software GEANT4 is shown in blue, the unscreened limit Eq. (2.38) (orange) and the completely screened limit Eq. (2.40) (red) are shown as well. Values have been normalised to the screened limit.

section becomes independent of the photon energy:

$$\sigma = \frac{7A}{9N_A X_0} \equiv \sigma_\infty. \tag{2.40}$$

Figure 2.8 compares the two limits of screening in Eqs. (2.38) and (2.40) with the corrected Bethe-Heitler model used within the GEANT4 software [92]. The discontinuity in the corrected cross section arises from a functional change in the parameterisations that underpin the model. Additionally, the GEANT4 model includes corrections for the Coulomb wavefunctions of the electron and positron, as well as pair conversion in the electron field of the atom. These corrections are not included in Eq. (2.38) which results in the mismatch of the model even at low photon energy.

For a single photon traversing a target of thickness t radiation lengths (i.e. $T = tX_0$), the number of pairs generated is

$$\mathrm{d}N_{\text{pairs}} = \frac{1 - \mathrm{e}^{-\mu t}}{\mu} \frac{N_A X_0}{A} \frac{\partial^2 \sigma}{\partial \epsilon \partial \Omega} \, \mathrm{d}\epsilon \, \mathrm{d}\Omega. \tag{2.41}$$

The photon attenuation factor, $\mu = {}^{7\sigma(\omega)}\!/_{9\sigma_\infty} = {}^{N_A X_0 \sigma(\omega)}\!/_{A}$, where σ_∞ is the complete screening limit of the cross section in Eq. (2.40). By integrating over the lepton energy and solid angle, the total pair yield can be estimated; using Eq. (2.39), the total pair yield for a single photon is

$$N_{\text{pairs}} = \frac{7}{9}\frac{1-\mathrm{e}^{-\mu t}}{\mu}. \tag{2.42}$$

If $\mu T \ll 1$, the exponential can be expanded to first order, $\mathrm{e}^{-\mu t} \approx 1 - \mu t$. In this limit, the pair yield is $7t/9$, or replacing with true thickness $7T/9X_0$. Since $X_0^{-1} \sim Z^2$, the number of pairs can be increased by using targets with a large Z, hence materials such as tantalum ($Z = 73$), tungsten ($Z = 74$) or even lead ($Z = 82$) are preferred. For a beam of photons with energy distribution $\mathrm{d}N_\gamma/\mathrm{d}\omega$, the number of pairs produced within an energy range $[\epsilon, \epsilon + \mathrm{d}\epsilon]$ assuming a thin target, is obtained from Eq. (2.41) as

$$\frac{\mathrm{d}N_{\text{pairs}}}{\mathrm{d}\epsilon} = \int \frac{N_A X_0 t}{A}\frac{\mathrm{d}\sigma}{\mathrm{d}\epsilon}\frac{\mathrm{d}N_\gamma}{\mathrm{d}\omega}\,\mathrm{d}\omega. \tag{2.43}$$

Since pair production and bremsstrahlung are related processes by crossing symmetry, the bremsstrahlung cross section has similar forms to Eqs. (2.37) and (2.39) in the unscreened and screened limits. Within the unscreened limit, the cross section for an electron (positron) of energy ϵ to emit a photon of energy $\omega = y\epsilon$ is [49]

$$\frac{\mathrm{d}\sigma}{\mathrm{d}y} = 4Z^2\alpha r_e^2 \frac{1}{y}(1-y)\left[\frac{1}{1-y} + (1-y) - \frac{2}{3}\right]\ln\left[\frac{2\omega y(1-y)}{m}\right]. \tag{2.44}$$

One fundamental feature of Eq. (2.44) is the infrared divergence due to the factor of y^{-1}, which corresponds to the increased emission of arbitrarily small energy. This divergence results in the total cross section, and hence the total number of emitted photons, being undefined. However, the total energy radiated $\mathcal{E}_{rad} \propto \int_0^1 y\frac{\mathrm{d}\sigma}{\mathrm{d}y}\,\mathrm{d}y$ is finite. In the complete screening limit where $\epsilon \gtrsim 1\,\text{GeV}$, the bremsstrahlung cross section takes the form

$$\frac{\mathrm{d}\sigma}{\mathrm{d}y} = \frac{A}{N_A X_0}\frac{1}{y}\left[\frac{4}{3}(1-y) + y^2\right]. \tag{2.45}$$

Similarly to the unscreened limit, the total cross section is infinite due to the infrared divergence however the radiated energy is finite.

2.5.2 Thick Target Effects

If $t \gtrsim 1$, the thin target approximation no longer holds and Eqs. (2.43) and (4.1) become inapplicable. To determine the effects from thicker targets, the approach detailed in [93] is followed, using the complete screening bremsstrahlung and pair production cross sections. The integro-differential shower equations remain unchanged, however the boundary conditions are amended to account for an incident mono-energetic photon beam. As in [93], let $I_\gamma(t,\omega)\,\mathrm{d}\omega$ be the intensity of photons at depth t within the target in the energy interval $[\omega, \omega + \mathrm{d}\omega]$. $I_e(t,E)\,\mathrm{d}E$ is the analogous quantity for the electrons and positrons combined. Shower equations are

$$\left\{\begin{aligned}
\frac{\partial I_\gamma(t,\omega)}{\partial t} &= -\frac{7}{9} I_\gamma(t,\omega) + \int\limits_{\omega}^{\omega_0} I_e(t,E)\left[\frac{4}{3}\left(1-\frac{\omega}{E}\right)+\left(\frac{\omega}{E}\right)^2\right]\frac{\mathrm{d}E}{\omega},\\
\frac{\partial I_e(t,E)}{\partial t} &= 2\int\limits_{E}^{\omega_0} I_\gamma(t,\omega)\left[\frac{4}{3}\left(1-\frac{\omega}{E}\right)+\left(\frac{\omega}{E}\right)^2\right]\frac{E^2\,\mathrm{d}\omega}{\omega^3}\\
&\quad + \int\limits_{0}^{\omega_0-E} I_e(t,E+\omega)\left[\frac{4}{3}\left(1-\frac{\omega}{E+\omega}\right)+\left(\frac{\omega}{E+\omega}\right)^2\right]\frac{\mathrm{d}\omega}{\omega}\\
&\quad - I_e(t,E)\int\limits_{0}^{E}\left[\frac{4}{3}\left(1-\frac{\omega}{E}\right)+\left(\frac{\omega}{E}\right)^2\right]\frac{\mathrm{d}\omega}{\omega},
\end{aligned}\right. \tag{2.46}$$

with corresponding boundary conditions

$$\begin{cases} I_\gamma(0,\omega) &= \delta(\omega-\omega_0),\\ I_e(0,E) &= 0. \end{cases} \tag{2.47}$$

The photon shower equation can be directly integrated using the boundary conditions by assuming a solution of the form $I_\gamma(t,\omega) = F(t,\omega)\mathrm{e}^{-7t/9}$, resulting in

$$I_\gamma(t,\omega) = \mathrm{e}^{-7t/9}\delta(\omega-\omega_0) + \frac{1}{\omega}\int_0^t \mathrm{e}^{-(7/9)(t-t')}\int_\omega^{\omega_0} I_e(t',E)\left[\frac{4}{3}\left(1-\frac{\omega}{E}\right)+\left(\frac{\omega}{E}\right)^2\right]\mathrm{d}E\ \mathrm{d}t'\,. \tag{2.48}$$

The first term represents the attenuation of the incident photon beam into electron-positron pairs, while the second term represents the bremsstrahlung generated by any pairs produced within the target. The lepton shower equation has no closed form solution, however it can be solved iteratively. By defining the zeroth generation particles as the incident photons such that $I_\gamma^{(0)}(t,\omega) = \delta(\omega - \omega_0)$, the electrons and positrons generated by these photons, as well as the bremsstrahlung photons, are then defined as first generation. Hence, by setting $I_e(t,E) = 0$ and using $I_\gamma^{(0)}(t,\omega)$, the first generation pairs can be found by direct integration of the lepton shower equation

$$I_e^{(1)}(t,E) = \frac{2t}{\omega_0}\left[1 - \frac{4}{3}\left(\frac{E}{\omega_0}\right)\left(1 - \frac{E}{\omega_0}\right)\right]. \tag{2.49}$$

The first generation photons can be obtained from Eq. (2.49) by substitution into the integral term in Eq. (2.48), and separating the integrals over t' and E.

$$\begin{aligned} I_\gamma^{(1)}(t,\omega) &= \frac{162}{49\omega}\left(\frac{7t}{9} - 1 + \mathrm{e}^{-7t/9}\right)\mathcal{F}\left(\frac{\omega}{\omega_0}\right) \\ \mathcal{F}(k) &\equiv \frac{4}{3}k(1+k)\ln k + \frac{28}{27}(1-k)\left[1 + k\left(k + \frac{43}{28}\right)\right] \end{aligned} \tag{2.50}$$

As $\lim\limits_{\omega\to 0} \omega I_\gamma^{(1)}(t,\omega) = \frac{28}{27}$, the characteristic infrared divergence of the bremsstrahlung can be seen. Additionally, although the photon number $\int I_\gamma(t,\omega)\,\mathrm{d}\omega$ is divergent, the mean photon energy, $\int \omega I_\gamma(t,\omega)\,\mathrm{d}\omega$, is finite.

Chapter 3

Experimental Programs and Numerical Modelling

3.1 SFQED Experiments

Within the past decade, multiple experiments have been proposed to investigate previously unexplored regimes of QED, as shown in Fig. 2.1. Broadly speaking, they can be categorised by the electron source, generated either by conventional accelerators or via plasma-based acceleration. Experiments involving laser wakefield accelerated (LWFA) electrons as a source, also termed "all-optical" in literature, have had much success in investigating QED. Production of 100's of MeV-scale x-ray sources using NLCS has been demonstrated at various facilities [94, 95, 96], indicating that it is a viable technique for producing high-brilliance photon beams within a compact laboratory environment [15]. Additionally, studies on radiation reaction in the $\chi \lesssim 1$ regime have also been carried out using ~2 GeV LWFA electrons, validating the appropriateness of the semiclassical model [17, 18]. Further investigation of the NLBW process has also been analysed using the ATLAS laser at CALA, Germany, which highlights the capability to observe pair production generated by the interaction of a high-energy bremsstrahlung beam and a high intensity laser [97].

Of the current experiments represented in Fig. 2.1, three are sourced by conventionally accelerated electrons: E-144, E-320 and LUXE. Taking advantage of the 13 GeV, 2 nC electron

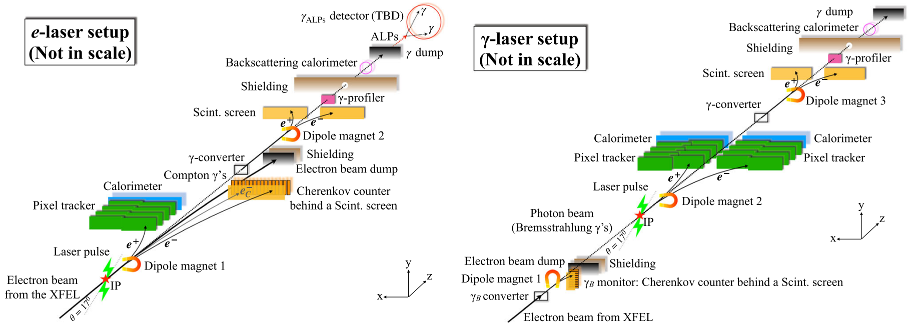

Figure 3.1: Schematic diagram of the proposed LUXE setup for the electron-laser (left) and photon-laser (right) modes. Reproduced from [21] under the terms of the Creative Commons CC-BY license.

beams that can be produced at the FACET-II linear accelerator, the E-320 experiment [19] follows the premise of the original E-144 experiment. Using a 20 TW NIR laser, E-320 expects to achieve intensities of $a_0 \lesssim 7$ and $\chi \lesssim 1$, accessing well into the non-perturbative transition regime, where tunnelling pair production can occur. With this setup, it will be possible to not only repeat the results of the E-144 experiment, but the departure from the perturbative a_0^{2n} will also be seen experimentally, providing crucial information on scaling laws within the transition regimes where analytical results are challenging to obtain.

As well as E-320, LUXE (Laser Und XFEL Experiment) [20, 21] is another proposed experiment that leverages the ∼16.5 GeV, 0.25 nC electron beam from the European XFEL (Eu-XFEL) and the high intensities of an optical laser up to 350 TW. With this setup it is possible to achieve parameters of $a_0 \lesssim 24$ and $\chi \lesssim 4.5$; this not only allows investigation of the non-linear, multi-photon regime of Compton scattering and Breit-Wheeler pair production, but also the transition regime from a classical to quantum electrodynamical description of radiation reaction, similarly to E-320.

In contrast to E-320, LUXE has two modes of operation: an electron-laser mode, where the Eu-XFEL electron beam is collided directly with the intense laser pulse at the designated interaction point (IP), and will be used to study non-linear Compton scattering, non-linear Breit-Wheeler production and trident production. In the second mode (photon-laser), the electron beam is first used to generate a high-energy, broadband bremsstrahlung photon beam as in Eq. (2.45) using a high-Z converter target. After the electrons and generated positrons are separated from the bremsstrahlung beam, the photons continue to the IP where they collide with the laser pulse. This operational mode allows for a purer environment to investigate non-linear

Breit-Wheeler pair production, and potentially photon-photon scattering, using real photons in isolation for the first time, compared to, for example, the use of virtual photons in the nuclear fields of heavy ions [81, 98]. The E-320 experiment has a setup that is comparable to the electron-laser mode of LUXE [99].

After the IP, LUXE has a series of detectors aimed at measuring the electron, positron and photon signal generated by the electron-laser or photon-laser interactions, as sketched in Fig. 3.1. The predicted signal for LUXE is shown in Fig. 3.2, taken from [21], and shows the large range of particle rates anticipated within the experiment. In particular, the photon signal is especially challenging to measure due to the combination of high energy (up to ∼16.5 GeV) and high flux ($\sim 1 \times 10^9\,\mathrm{s}^{-1}$), as shown in Fig. 3.2b. Due to the complexity of the experiment and the consequent challenges in measuring such a signal, the detector systems employed in LUXE are specifically developed from traditional detection techniques such as a pixel tracker array for the positron signal ad well as Čerenkov detectors and scintillators for electrons [22, 23]. The intricacies involved in the measurement of the photon signal prompted the development of three separate but complementary detectors: the gamma-ray spectrometer, whose development and testing is detailed in Chapter 4; the gamma beam profiler, the principles of which are outlined as well in Chapter 5; and the gamma flux monitor, details on which can be found in [21] and is not discussed further here. Additionally, a beyond the Standard Model investigation into the production of axion-like particles is also possible at LUXE, utilising the high-flux, high-energy Compton produced photon source [100]. Other facilities have been developed to investigate other non-linear QED processes, for example, HIBEF in Helmholtz, Germany and the PVLAS experiment at INFN, Italy aim to study vacuum birefringence in strong electromagnetic fields [101, 102]; a QED regime that is currently beyond the scope of LUXE and E-320.

While experiments like E-320 and LUXE are designed to investigate non-linear, multiphoton QED processes, elastic two-photon processes such as linear Breit-Wheeler production and photon-photon scattering have yet to be observed due to the large ZMF energy required. Additional difficulty for the measurement of photon-photon scattering is the extremely small cross section, being an α^4-order process. Previous campaigns aimed at detecting such scattering events using optical and x-ray beams were unable to detect scattering events directly, instead bounding the

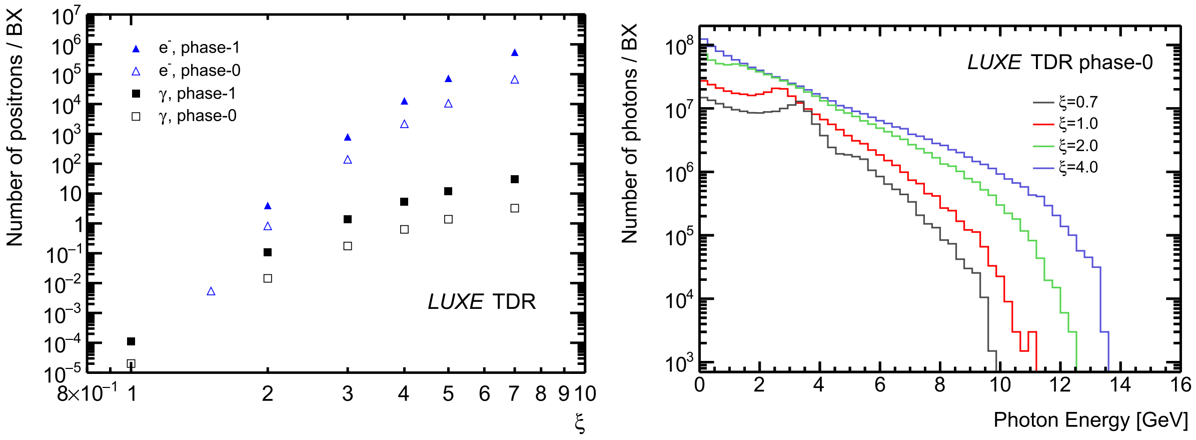

(a)

(b)

Figure 3.2: Anticipated (a) positron, and (b) photon rates at LUXE as a function of normalised laser amplitude a_0, called ξ in the plot. e^- and γ refer to the electron-laser and photon-laser operating modes respectively; phase-0 indicates a laser power of 40 TW, and phase-1 occurs after an upgrade to 350 TW. Reproduced from [21] under the terms of the Creative Commons CC-BY license.

magnitude of the cross section [75, 76, 77, 78]. For these experiments, the ZMF energy was $\sqrt{s} \sim 1$ keV which corresponds to a scattering cross section of $\sigma_{\gamma\gamma} \sim 1 \times 10^{-42}\,\mathrm{cm}^2$; c.f. the Thomson scattering cross section, $\sigma_T = 6.65 \times 10^{-25}\,\mathrm{cm}^2$ [30, 59]. One configuration utilising gamma-ray photons produced via Compton-scattering of electrons and an extreme ultraviolet (XUV) pulse has been detailed in [103], which suggests the possibility of detecting elastic scattering events within one day of operation by observing the resultant transverse profile of the gamma beam after collision with the XUV pulse. An alternative approach, using a high energy (GeV-scale) bremsstrahlung beam and a dense, ~ 0.1 keV-scale x-ray field generated within a vacuum hohlraum was proposed in [104] to study linear Breit-Wheeler production. With this configuration, it is possible to achieve a ZMF energy of $\sqrt{s} \approx 1$ MeV. This configuration could be adapted to also investigate photon-photon scattering, as $\sqrt{s} \approx 1$ MeV yields the peak scattering cross section of $\sim 10^{-30}\mathrm{cm}^2$, as was done at the Gemini laser facility at RAL, UK.

Here, the dual-beam laser capabilities were utilised; one beam to generate the LWFA electron source, and the other to generate a dense x-ray bath from an exploding germanium foil, rather than a hohlraum [105]. Using the produced electron beam with energies up to ~700 MeV, and a beam charge of 50 pC, a collimated, high energy (up to ~500 MeV) bremsstrahlung beam is produced using a bismuth converter target which is then propagated through the dense x-ray field. It was demonstrated that this compact configuration could be a compelling platform for future investigations into photon-photon interactions with the proposed improvements. Furthermore, the same investigation was also able to place the most stringent bound on the elastic photon-photon scattering cross section to date [79] as seen in Fig. 2.7, emphasising the potential of further development of this setup.

3.2 Numerical Modelling Methods

Modelling the signal and noise anticipated within experiments requires the use of Monte-Carlo (MC) simulations. In short, MC methods can be used to simulate stochastic processes such as those described in Chapter 2 by sampling particle properties from the differential cross sections of these processes. Additionally, tracking capabilities are also useful to propagate these particles through geometries and fields. For the work in this thesis, three main MC simulation software were utilised: PTARMIGAN, FLUKA, and GEANT4.

The signal that is to be measured at LUXE originates from the (non-linear) Compton scattering and Breit-Wheeler processes during electron-laser and photon-laser interactions. These SFQED processes are simulated within the PTARMIGAN framework, which is an MC-based code to simulate the interactions of high-energy particle (electron, positron or photon) beams with strong laser fields [63, 106]. PTARMIGAN has the ability to simulate both non-linear Compton scattering and non-linear Breit-Wheeler production within background fields of different configurations, with plane-wave or Gaussian-like spatial structures and flat-top, square cosine and Gaussian type temporal envelopes. As well as this, processes are polarisation resolved - the background field can be implemented with linear or circular polarisation, and the spin/polarisation of the emitted particles is also included. These processes are modelled using rates calculated in both the LCFA and LMA frameworks, allowing for the use of models appropriate for the simulated a_0 and χ parameters, as well as for drawing comparisons between the effects captured by either model. LMA-calculated rates are available only for $a_0 \lesssim 20$ due to necessary pre-tabulation of values, whereas LCFA rates can be used for arbitrary values.

Another useful feature of PTARMIGAN is the potential to use different models for radiation reaction, which can be disabled if desired. The software implements both a classical RR

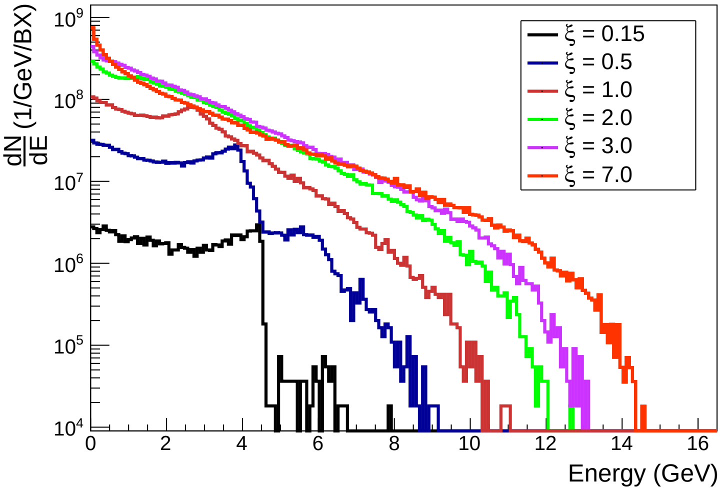

Figure 3.3: Example energy spectra of Compton-scattered photons generated by PTARMIGAN for the interaction of a 16.5 GeV electron beam with a focused laser pulse per bunch crossing (BX) of different normalised intensities, ξ (equivalent to a_0). Reproduced from [21] under the terms of the Creative Commons CC-BY license.

model, where the emission is sampled as a deterministic process using the classical synchrotron spectrum Eq. (2.28) and the particle trajectory is determined from the LL equation Eq. (2.24). A fully quantum model, incorporating stochastic emission effects non-deterministically with the trajectory of the particle following the usual Lorentz equation between emission events, and the quantum synchrotron spectrum Eq. (2.29) is used to generate the radiated photon properties. A third semiclassical RR model which follows the same deterministic approach as the classical model for the trajectory and emission, however photon properties are instead sampled using the Gaunt-corrected emission spectrum. This model is available only in the LCFA framework. With all of these features, PTARMIGAN is highly advantageous for simulating the electron-laser and photon-laser interactions to be performed at LUXE for various experimental parameters and configurations. The output from PTARMIGAN simulations can also be structured into a phase space format which can be imported into further simulations involving tracking through full experimental geometries.

The particle tracking through a geometry is done using both FLUKA [107, 108] and GEANT4 [109, 110, 111] here. Both codes are general-purpose MC simulation and tracking frameworks and are considered industry standard within a wide range of branches of physics. As such, the general operating principles for both codes is the same and are able to simulate the

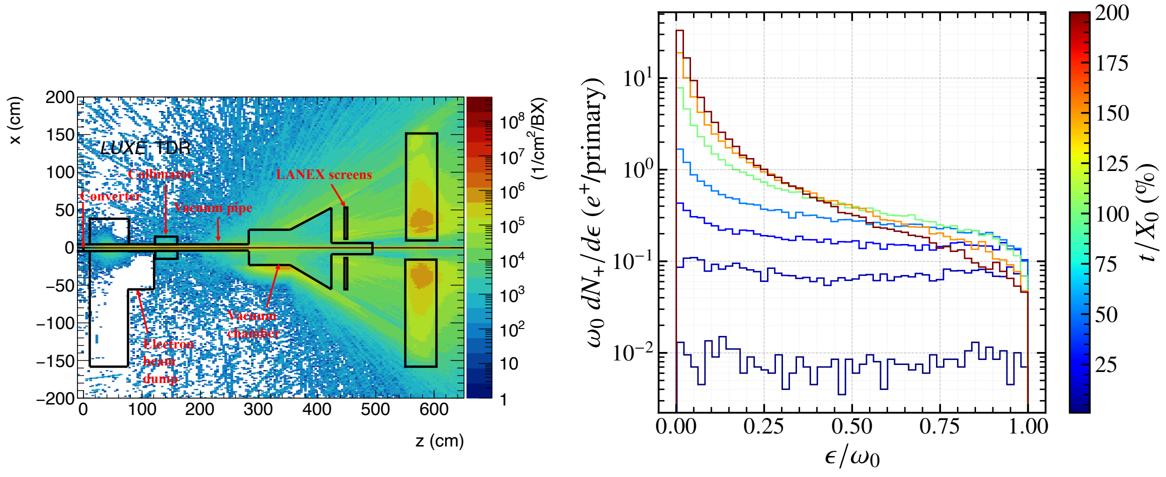

(a) **(b)**

Figure 3.4: Example plots produced using the scoring output of (a) Fluka, and (b) Geant4. (a) depicts the photon fluence within a specific detector subsection within the LUXE experimental setup and is taken from [21]. (b) shows resultant positron spectra produced from interacting a monoenergetic photon beam with a high-Z foil of different fractions of X_0 thick. This is elucidated further in Section 4.1. (a) has been reproduced from [21] under the terms of the Creative Commons CC-BY license.

behaviour of a large array of particle types, and their antiparticles, as they traverse some defined geometry. Tracking is done in discrete steps, taking into account the propagation through different materials as well as the effect of electric and magnetic fields. Within these materials, processes such as Compton scattering, photoelectric production, ionisation, bremsstrahlung and pair production are modelled using MC sampling and particle tracks are subject to multiple scattering also. Furthermore, optical processes like scintillation, Čerenkov and transition radiation can also be simulated. The extraction of various particle properties such as energy, position or momentum direction at specified planes or geometry boundaries (known as scoring) is also possible and is the main method of extracting information from such simulations.

Overall, Fluka and Geant4 are generally equivalent and both have similar capabilities. Fluka is popular in the field of radiation physics, with its accurate generation of hadronic events well-documented, but it is also capable of accurately simulating the transport of electrons, positrons and photons (known as electromagnetic particles within this context, as the do not engage in strong or weak interactions) over a large energy range from ~1 keV to ~1 PeV. On the other hand, Geant4 is heavily utilised in high energy physics, particularly in the design and development of particle colliders, as well as medical physics and space radiation physics. Like Fluka, Geant4 is able to simulate electromagnetic particles from ~1 eV up to ~100 TeV.

Furthermore, GEANT4 provides greater customisation of the physics incorporated within the simulation, including the ability to define additional processes not included within the software. Throughout the work presented here, a combination of FLUKA and GEANT4 is used, both for benchmarking comparisons and due to considerations of geometry description and scoring techniques. The exact software used is indicated as appropriate in the text.

The increased customisability of GEANT4 is particularly useful for the simulations involving photon-photon scattering, as this is not already implemented in either GEANT4 or FLUKA. An external package, developed for modelling linear Breit-Wheeler and photon-photon scattering in experiments at Gemini, RAL, UK, is used in combination with GEANT4 for the work presented here studying elastic photon scattering [54]. Within this module, it is possible to implement a static radiation field within which the linear Breit-Wheeler and elastic photon-photon scattering are available physical processes that photons (designated as gammas within the simulation architecture) can undergo.

Chapter 4

Gamma Ray Spectroscopy

Gamma-ray beams with high energies per photon (~MeV - TeV scale) are of great interest across a large range of physical disciplines, such as astrophysical [112] and nuclear [113] phenomena. Typical methods of generating such high-flux and high-energy sources in a laboratory include: passing an electron beam through a high-Z solid target to generate bremsstrahlung [114, 115, 116]; non-linear Compton emission from the interaction of an electron beam with the focus of an intense laser [15, 95]; or even direct irradiation of solid targets using next-generation multi-PW lasers [117, 118].

Conventional methods of photon detection such as gas ionisation detectors, Compton scattering in semiconductor devices and scintillators have difficulty resolving gamma-ray beams in this energy range as the dominant photon process above 1 MeV is pair production, and for high-flux beams, the copious number of electron-positron pairs generated cannot be correlated to their original photon readily. Alternatives to these have their own limitations, either designed to operate at high energy but at low flux [114], down to the single particle level [119], or are capable of resolving a high-flux beam at the MeV scale [120, 121] or within a narrow energy region [122].

A design similar to that described in [120] has been developed to operate with gamma-rays at the GeV-scale, with preliminary simulation studies [25] and a first experimental demonstration [26] highlighting the development of the implementation and diagnostic tools for reproducing the photon spectrum. The basic operation principle of this novel-style gamma-ray spectrometer

(GRS) is conceptually simple. The incident high-energy, high-flux photon beam is directed onto a high-Z solid target which converts a small fraction ($\lesssim 1\%$) of the gamma-rays into electron-positron pairs via the well-known Bethe-Heitler pair production process. These pairs are then separated and diverted out of the unconverted gamma-ray beam using a dipole magnet which also induces an energetic dispersion of the pairs in a plane transverse to the magnetic field. These dispersed pairs are then propagated to a scintillator screen where the signal can be measured using standard techniques. Finally, the original photon spectrum is recovered by means of a deconvolution algorithm which utilises knowledge of the converted electron/positron energy spectra and the Bethe-Heitler cross section.

This chapter focuses on the development of this detector design and is structured as follows: Section 4.1 discusses the key components of the spectrometer - pair generation, magnetic spectroscopy and the reconstruction algorithm; Section 4.2 shows the results from simulations with a focus on the GRS implementation at LUXE; and finally, Section 4.3 focuses on the first experimental characterisation of the spectrometer.

4.1 Principles of Operation

4.1.1 Generation of Electron-Positron Pairs in a Solid Target

In order to spectrally resolve the photon beam, a high-Z target is used to convert a fraction of the beam into electron-positron pairs via the Bethe-Heitler process as outlined in Section 2.5. As the GRS is designed to be non-invasive, it is important that the production of the electron-positron pairs has a negligible influence on the characteristics of the original photon beam such as energy spectrum and spatial distribution. Hence, it is important to optimise not only the pair yield in order to have a statistically significant signal to resolve and deconvolve, but the target should be designed to negligibly interfere with the photon beam.

For modelling purposes, it is interesting to consider the conversion response to a mono-energetic beam, ${}^{\mathrm{d}N_\gamma}/_{\mathrm{d}\omega} = N_0\delta(\omega - \omega_0)$. Integrating Eq. (2.43) over both photon and lepton

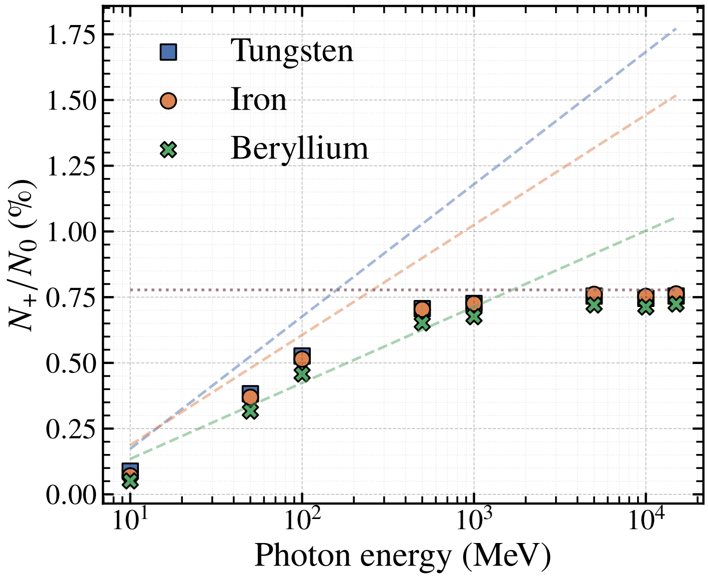

Figure 4.1: Percentage yield of positrons from a mono-energetic photon beam incident on tungsten (blue), iron (orange) and beryllium (green) converters, 1% X_0 thick. The yield predicted by Eq. (2.41) using the unscreened Eq. (2.38) (dashed line) and the completely screened Eq. (2.40) (dotted line) cross sections are shown for comparison.

energy gives the number of pairs as

$$\frac{N_{\text{pairs}}}{N_0} = \frac{N_A X_0 t}{A} \sigma(\omega_0). \tag{4.1}$$

This ratio can be used to compare different cross section models, such as Eqs. (2.38) and (2.40), with simulation in different energy regimes. Particularly, in the complete screening regime of Eq. (2.40), the yield is predicted to be independent of the material and depends only on the converter thickness relative to the radiation length, t. As shown in Fig. 4.1, the unscreened cross section, Eq. (2.38), is more accurate at lower photon energies $\lesssim$ 100 MeV, while the complete screening limit, Eq. (2.40), is comparable to the advanced GEANT4 model above the GeV limit.

Following from the production of showers, Eqs. (2.49) and (2.50), as the converter thickness increases, electrons and positrons lose energy through bremsstrahlung, which can also produce additional pairs with lower energy. This straggling results in an energy spectrum which significantly deviates from Eqs. (2.43) and (4.1) as seen in Fig. 4.2a. Above $t = 1/2$, the number of positrons (and similarly electrons) in the high energy tail is reduced as they radiate more. Consequently, there is a higher population of lower energy positrons and a decreased mean energy. From Eq. (2.49), the mean positron energy in the thin target approximation is

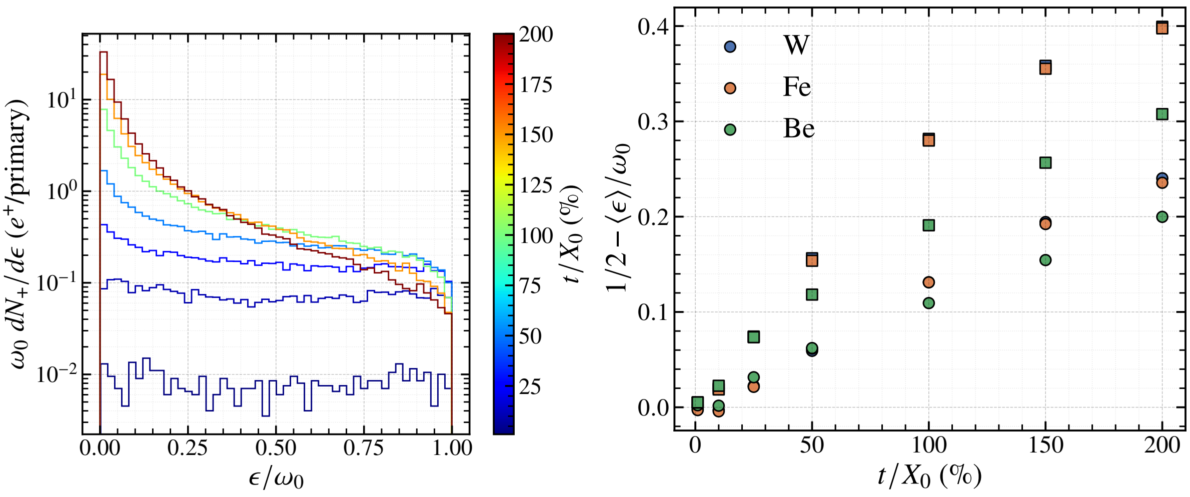

(a) **(b)**

Figure 4.2: (a) Resultant energy spectra of positrons exiting a tungsten converter of different thicknesses in % of X_0 for an incident mono-energetic photon beam with $\omega_0 = 5\,\text{GeV}$. (b) Deviation of the mean positron energy from the thin target limit as a function of converter thickness for tungsten (blue), iron (orange) and beryllium (green) targets. Two incident photon beams of energy 500 MeV (circles) and 5 GeV (squares).

$\langle E \rangle = \omega_0/2$. Fig. 4.2b shows the deviation of the mean positron energy from this limiting value with increasing thickness. Even at $t \approx 0.25$, the mean positron energy deviates by over 10% for $\omega_0 = 5\,\text{GeV}$. Therefore, thicknesses up to 10% of X_0 are sufficient to generate a sufficiently large electron-positron signal without compromising the spectral distribution of the thin-target approximation.

4.1.2 Magnetic Spectroscopy

The techniques of magnetic spectroscopy for measuring the energy of charged particles are fairly standard. In the context of the GRS, after the electron-positrons pairs are generated via Bethe-Heitler pair production, they can be passed through a dipole magnet to not only separate the particles due to charge, but also transversely disperse them due to their energy. For a particle of mass, m, and charge, e, traversing a dipole field of strength, $\mathbf{B}$, with momentum, $\mathbf{p}$, it makes a circular trajectory with radius of curvature $\rho = |\mathbf{p}|^2/e|\mathbf{p}\times\mathbf{B}|$. In the ultrarelativistic limit for a particle of energy ϵ, $|\mathbf{p}| = \sqrt{\epsilon^2 - m^2} \approx \epsilon$, and $\rho \approx \epsilon/e|\mathbf{B}|$. For a magnetic field of length, z_M, with a detector screen placed a distance z_D on-axis after the exit of the magnet, it can be shown from geometrical considerations that the transverse displacement along the plane of $\mathbf{B}$ due to dispersion of an on-axis particle is given by

$$x = \rho - \frac{\rho^2 - z_M z_D - z_M^2}{\sqrt{\rho^2 - z_M^2}}. \tag{4.2}$$

In the case $\rho \gg z_M$ or equivalently, $\epsilon \gg e|\mathbf{B}|z_M$, then

$$x \approx \frac{z_M}{\rho}\left(\frac{z_M}{2} + z_D\right). \tag{4.3}$$

Hence, given the position of a particle on the screen, Eq. (4.3) can be inverted to give $\epsilon = \epsilon(x)$.

The resolution of this method is limited due to two factors: the finite resolution of the detector screen, and the divergence of the incident particle beam. If the width of a pixel or cell on the detector, w, is greater than the separation of two energies ϵ_1, ϵ_2 with $\epsilon_1 < \epsilon_2$, then these energies cannot be resolved. Hence, $\delta x \equiv x(\epsilon_1) - x(\epsilon_2) = w$ is the smallest possible separation that can be resolved. Assuming $\rho_{1,2} \gg z_M$, then from Eq. (4.2)

$$\delta x \approx z_M(z_M + z_D)\frac{\rho_2 - \rho_1}{\rho_1 \rho_2} \longrightarrow z_M(z_M + z_D)\frac{\delta\rho}{\rho^2}, \tag{4.4}$$

as $\rho_{1,2} = \rho \longrightarrow \infty$ in the limit of small pixel size. Therefore, the energy resolution due to the granularity of the detector is

$$\frac{\delta\rho}{\rho} \equiv \left(\frac{\delta\epsilon}{\epsilon}\right)_{\text{pixel}} = \frac{\rho w}{z_M(z_M + z_D)}. \tag{4.5}$$

The resolution due to the particle divergence is considered in [123], but involves similar considerations as before. Since the resolutions are independent, the total energy resolution available is the quadrature sum of the contributions which is (approximately) a linear function of the lepton energy,

$$\frac{\Delta\epsilon}{\epsilon} = \frac{(z_S + z_M + z_D)\Theta_S}{(z_D + z_M/2)z_M} \times \frac{\epsilon}{eB} \oplus \frac{\delta x}{z_M(z_M + z_D)} \times \frac{\epsilon}{eB}. \tag{4.6}$$

In the ultrarelativistic limit, for a photon beam with divergence, θ_γ, to produce a beam of electrons/positrons with energy $\epsilon = \gamma m$ results in a divergence of $\Theta_S \sim \sqrt{\theta_\gamma^2 + 1/\gamma^2}$.

4.1.3 Reconstruction of the Photon Spectrum

The problem of determining the original photon spectrum amounts to solving Eq. (2.43) for ${}^{\mathrm{d}N_\gamma}/_{\mathrm{d}\omega}$, given a measurement of ${}^{\mathrm{d}N_{\mathrm{pairs}}}/_{\mathrm{d}\epsilon}$ and a model for the differential cross section. Since a photon of energy ω cannot produce an electron/positron with energy $\epsilon > \omega$, the limits of integration in Eq. (2.43) can be bounded as $[\epsilon, \omega_{\mathrm{max}}]$, where ω_{max} is the maximum energy of the photon beam. The differential cross section is now strictly positive within this integration range. Hence, Eq. (2.43) can be written in the form of a Volterra integral equation of the first kind,

$$\frac{\mathrm{d}N_{\mathrm{pairs}}}{\mathrm{d}\epsilon} = \int_{\epsilon}^{\omega_{\mathrm{max}}} \frac{N_A X_0 T}{A} \frac{\mathrm{d}\sigma}{\mathrm{d}\epsilon} \frac{\mathrm{d}N_\gamma}{\mathrm{d}\omega} \,\mathrm{d}\omega, \tag{4.7}$$

and the spectral reconstruction of the photon beam is equivalent to solving this Volterra equation.

The principles of solving this equation will be discussed in the context of the general form

$$y(t) = \int_t^a K(s,t)\, x(s)\, \mathrm{d}s. \tag{4.8}$$

$x(s)$ is the unknown function to be solved for, $y(t)$ is the known or measured response and $K(s,t)$ is the kernel function. It is also assumed here that a is a real, positive constant. Applying the extended trapezium rule to discretise the integral in s-space into $N-1$ partitions of width h, and since $s_1 = t$ and $s_N = a$:

$$y(t) \approx \frac{1}{2}K(t,t)x(t)h + \frac{1}{2}K(a,t)x(a)h + h\sum_{i=2}^{N-1} K(s_i,t)\, x(s_i). \tag{4.9}$$

Rearranging for $x(t)$ gives the "back-substitution" solution to Eq. (4.8) [124],

$$x(t) \approx \left[\frac{1}{2}K(t,t)\right]^{-1} \left[\frac{1}{h}y(t) - \frac{1}{2}K(a,t)x(a) - \sum_{i=2}^{N-1} K(s_i,t)\, x(s_i)\right]. \tag{4.10}$$

For a fixed grid in s-space, only the terms where $s_i > t$ are included in the sum. Then for $t = a$, the sum contains no terms and Eq. (4.9) reduces to $y(a) \approx K(a,a)x(a)h$ and so

$x(a) \approx y(a)/K(a,a)h$. From this, Eq. (4.10) can be expressed as

$$x(t) \approx \left[\frac{1}{2}K(t,t)\right]^{-1}\left[\frac{1}{h}y(t) - \frac{1}{2h}\frac{K(a,t)}{K(a,a)}y(a) - \sum_{i=2}^{N-1} K(s_i,t)\, x(s_i)\right]. \tag{4.11}$$

Due to dependence of $x(t)$ on previously calculated terms, error is amplified for each value of t. This expresses the well-known ill-conditioned nature of Volterra-type problems, which are typically sensitive to their initial conditions.

This error amplification can be seen even in the simple case that the $y(t)$ in Eq. (4.11) are exact and so the error in $x(t)$ is given by

$$\delta x(t) = 2\sqrt{\sum_i \left[\frac{K(s_i,t)}{K(t,t)}\delta x(s_i)\right]^2}, \tag{4.12}$$

where the sum over i is such that all $s_i > t$. Taking $\kappa = {}^{K(s_i,t)}/_{K(t,t)}$ to be approximately constant and independent of s, t, Eq. (4.12) becomes $\delta x(t)^2 \approx 2\kappa \sum\limits_i \delta x(s_i)^2$. From this, it can be seen that the accumulation of error in Eq. (4.11) depends on the number of gridpoints used, i.e. a higher resolution will increase the rate of accumulation, and the initial error in the point $x(s_N)$, denoted δx_N. Figure 4.3 shows an example of this exponential error accumulation for $\delta x_N = 1$ and using the kernel $K(s,t) = 1 - {}^{4t}/_{3s}(1 - {}^{t}/_{s})$, which is the form of Eq. (2.39).

Instead, it is more beneficial to formulate Eq. (4.8) in a statistical manner, which then allows for the regularisation of the problem and to statistically quantify the uncertainty in the solution [125, 126, 127]. Equation (4.8) can be expressed as an operator equation $y = \mathcal{K} \circ x$, then discretisation is equivalent to a matrix representation, $\mathbf{y} = K\mathbf{x} + \boldsymbol{\varepsilon}$, where $\boldsymbol{\varepsilon}$ is a term to account for error in $\mathbf{y}$. If $\boldsymbol{\varepsilon} = 0$, then the standard solution $\mathbf{x} = K^{-1}\mathbf{y}$ is equivalent to Eq. (4.11) for the appropriate discretisation rule. The ill-condition of the problem means that this direct inversion is unstable, as mentioned earlier. Instead, we assume that $\boldsymbol{\varepsilon}$ comes from a normal distribution with zero mean and unknown covariance Σ, i.e. $\boldsymbol{\varepsilon} = \mathbf{y} - K\mathbf{x} \sim \mathcal{N}(0, \Sigma)$. The probability density function (PDF) is then of multivariate normal form

$$\mathbb{P}(\mathbf{y}|\mathbf{x}; K, \Sigma) = \frac{1}{\sqrt{(2\pi)^d \det\Sigma}} \exp\left[-\frac{1}{2}(\mathbf{y} - K\mathbf{x})^T\Sigma^{-1}(\mathbf{y} - K\mathbf{x})\right], \tag{4.13}$$

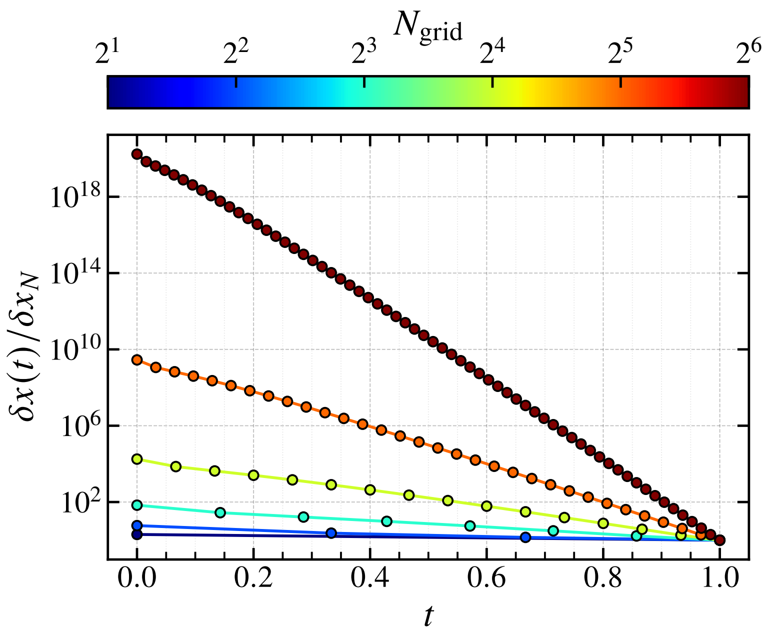

Figure 4.3: Plot of the error propagation in the Volterra solution Eq. (4.11), as given by Eq. (4.12) for different grid sizes, N. The kernel used is specified in text.

where $d = \dim(\mathbf{y}) = \dim(K\mathbf{x})$. The dependence of the PDF on K and Σ will be dropped and implicitly assumed for brevity. The solution to Eq. (4.8) can then be generated from the posterior distribution, $\mathbb{P}(\mathbf{x}|\mathbf{y})$, which is given by Bayes' Theorem:

$$\mathbb{P}(\mathbf{x}|\mathbf{y}) \propto \mathbb{P}(\mathbf{y}|\mathbf{x}) \cdot \mathbb{P}(\mathbf{x}). \tag{4.14}$$

This requires the statement of a prior distribution for $\mathbf{x}$, $\mathbb{P}(\mathbf{x})$. To have an analytical solution, assume a normal distribution with known mean $\mathbf{x}_0$ and unknown covariance Σ_x,

$$\mathbb{P}(\mathbf{x}) = \frac{1}{\sqrt{(2\pi)^{d_x} \det \Sigma_x}} \exp\left[-\frac{1}{2}(\mathbf{x}-\mathbf{x}_0)^T \Sigma_x^{-1} (\mathbf{x}-\mathbf{x_0})\right]. \tag{4.15}$$

To calculate the posterior distribution from Eq. (4.14), the hyperparameters Σ and Σ_x need to be determined. One approach to hyperparameter estimation is marginal likelihood maximisation (MLM), where the marginal likelihood distribution is given by

$$\mathbb{F}(\mathbf{y};\Sigma,\Sigma_x) = \int \mathrm{d}\mathbf{x}\ \mathbb{P}(\mathbf{y}|\mathbf{x};\Sigma) \cdot \mathbb{P}(\mathbf{x};\Sigma_x), \tag{4.16}$$

where the hyperparameter dependence has been shown. The notation $\mathbb{F}(\mathbf{y})$ is used to emphasise that, although the marginal likelihood distribution resembles a PDF, it does not, in general, have unit integral and so is not a true probability density. The hyperparameter estimates, $\hat{\Sigma}, \hat{\Sigma}_x$, are then defined as

$$\hat{\Sigma}, \hat{\Sigma}_x = \underset{\Sigma,\Sigma_x}{\arg\max}\ \mathbb{F}(\mathbf{y}|\Sigma,\Sigma_x) \equiv \underset{\Sigma,\Sigma_x}{\arg\min}\,[-\ln \mathbb{F}(\mathbf{y}|\Sigma,\Sigma_x)], \tag{4.17}$$

i.e. they maximise $\mathbb{F}(\mathbf{y})$, or equivalently due to the monotonicity of the logarithm, minimise its negative logarithm. The latter framing of the optimisation problem is particularly useful numerically, as it removes exponentiation in calculations. For $\mathbb{P}(\mathbf{y}|\mathbf{x})$ and $\mathbb{P}(\mathbf{x})$ given by Eq. (4.16) and Eq. (4.15) respectively, the marginal likelihood also has a Gaussian form. The minimising function (the negative logarithm of the marginal likelihood with constants and common scaling factors removed) is

$$L = -\ln\det A + \ln\det\Sigma + \ln\det\Sigma_x + (\mathbf{y}-\boldsymbol{\mu}_y)^T B^{-1}(\mathbf{y}-\boldsymbol{\mu}_y) + \mathbf{x}_0^T C^{-1}\mathbf{x}_0, \tag{4.18}$$

where

$$A = (\Sigma_x^{-1} + K^T\Sigma^{-1}K)^{-1}, \tag{4.19}$$

$$B = \Sigma + K\Sigma_x K^T, \tag{4.20}$$

$$C = \Sigma_x + AK^T\Sigma K A, \tag{4.21}$$

$$\boldsymbol{\mu}_y = A(\Sigma_x^{-1}\mathbf{x}_0 + K^T\Sigma^{-1}\mathbf{y}). \tag{4.22}$$

Equation (4.18) can be rather expensive to evaluate so an alternative can be used to approximate the minimum, with the possibility of using Eq. (4.18) a small number of times in an optimisation loop to fine-tune the hyperparameter values. By normalising Eq. (4.16) to unit integral (making it a true PDF), the terms in Eq. (4.18) which do not involve $\mathbf{y}$ are cancelled out due to the Gaussian form of the marginal likelihood. Hence, the reduced minimising function, L_{red}, takes the form

$$L_{\text{red}} = \ln\det B + (\mathbf{y}-\boldsymbol{\mu}_y)^T B^{-1}(\mathbf{y}-\boldsymbol{\mu}_y), \tag{4.23}$$

where $\boldsymbol{\mu}_y$ and B are defined as above. A simple form for the covariance matrices comes from assuming that the components of $\boldsymbol{\varepsilon}$ and $\mathbf{x}$ are mutually independent and of equal variation. Under this assumption, Σ and Σ_x take the form $1/\beta \otimes \mathbb{1}$ and $1/\theta \otimes \mathbb{1}$ respectively, where β, θ are strictly positive real values, and $\mathbb{1}$ is the identity matrix. Hence, the optimisation problem of finding the $2 \times d(d-1)/2$ components of the two symmetric matrices, Σ, Σ_x, is reduced to finding the two minimising values of β and θ.

Once the hyperparameters have been estimated, the posterior distribution can be determined from Eq. (4.14). Again, due to the normal likelihood and prior distributions, the posterior is also a normal distribution in $\mathbf{x}$, with mean $\boldsymbol{\mu}_x = A(\Sigma_x^{-1}\mathbf{x}_0 + K^T\Sigma^{-1}\mathbf{y})$ and covariance A as defined in Eq. (4.19). The solution to the (discretised) Volterra equation is then chosen to be the maximum a posteriori (MAP) estimate; for a normal distribution, this coincides with the mean, hence

$$\hat{\mathbf{x}} = (\Sigma_x^{-1} + K^T\Sigma^{-1}K)^{-1}(\Sigma_x^{-1}\mathbf{x}_0 + K^T\Sigma\mathbf{y}). \tag{4.24}$$

The hat denotes here the estimated solution, not a unit vector. It is educational to consider the MAP solution for the diagonal covariance case discussed above, and also taking the known prior mean $\mathbf{x}_0$ to be zero. Letting $\lambda = \theta/\beta$, Eq. (4.24) becomes

$$\hat{\mathbf{x}} = (K^TK + \lambda\mathbb{1})^{-1}K^T\mathbf{y}, \tag{4.25}$$

which is precisely the linear least squares solution to $\mathbf{y} = K\mathbf{x}$ with Tikhonov regularisation [128].

The uncertainty in the solution Eq. (4.24) is given by a confidence interval on the MAP. There are many ways to define this, but the one selected here is the highest posterior density interval (HPDI). Let X be a random variate with PDF $f_X(x)$. The $(1-\alpha)$ level HPDI is then the interval,

$$\mathcal{I}_\alpha = \{x | f_X(x) \geq f_\alpha\} \subseteq X, \tag{4.26}$$

where f_α is the largest constant such that $\mathbb{P}(X \in \mathcal{I}_\alpha) \geq 1 - \alpha$. In general, HPDI can be the union of multiple subsets of X. For a univariate normal distribution, which is unimodal and symmetric about its peak, Eq. (4.26) has an analytical solution for the HPDI. As normal distribution is symmetric, so is the HPDI - define it to be the interval $X \in [-\ell, +\ell]$. Then, for the standard normal distribution, $\mathbb{P}(X \in \mathcal{I}_\alpha) \geq 1 - \alpha$, has the equivalent requirement

$$\Phi(\ell) \geq \frac{1-\alpha}{2} + \Phi(0), \tag{4.27}$$

where $\Phi(x)$ is the cumulative density function (CDF) of the standard normal distribution. $\Phi(x)$ is monotonically increasing by definition, hence the smallest ℓ satisfying Eq. (4.27) will give the largest $f_\alpha = f_X(\ell)$ in Eq. (4.26). Therefore, the half-width of the $1 - \alpha$ level HPDI for the standard normal distribution is

$$\ell_{min} = \Phi^{-1}\left[\frac{1-\alpha}{2} - \Phi(0)\right]. \tag{4.28}$$

For a univariate normal distribution $\mathcal{N}(\mu, \sigma)$, the HPDI half-width is $\ell_\pm = \mu \pm \sigma\ell_{min}$.

It is possible to define the HPDI for a multivariate normal distribution in a similar fashion. Consider the distribution, $Z \sim \mathcal{N}(0, \mathbb{1})$, whose PDF can be expressed as

$$\mathbb{P}(\mathbf{z}) = (2\pi)^{-n/2} \exp\left(-\frac{1}{2}\mathbf{z}^T\mathbf{z}\right), \tag{4.29}$$

where $\mathbf{z}$ is n-dimensional and $\mathbb{1}$ is the $n \times n$ identity matrix. Due to symmetry, the HPDI forms a hypersphere in z-space about the mean (origin). Defining the z-space radius, r, as $r^2 \equiv \|\mathbf{z}\|_2^2 = \mathbf{z}^T\mathbf{z}$, the radial CDF (or probability that the radius of $\mathbf{z}$ is less than or equal to a given value) is given by

$$F_n(r) = (2\pi)^{-n/2}\Omega_n \int_0^r \varrho^{n-1} \exp\left(-\frac{\varrho^2}{2}\right) \mathrm{d}\varrho. \tag{4.30}$$

$\Omega_n = 2\pi^{n/2}/\Gamma({}^n\!/\!_2)$ is the solid angle in n-dimensional space and $\Gamma(z)$ is the gamma function. The integral in Eq. (4.30) leads to

$$F_n(r) = 1 - \frac{\Gamma(n/2, r^2/2)}{\Gamma(n/2)} = P\left(\frac{n}{2}, \frac{r^2}{2}\right), \tag{4.31}$$

where $\Gamma(a, z)$ is the upper incomplete gamma function and $P(a, z)$ is the (lower) regularised

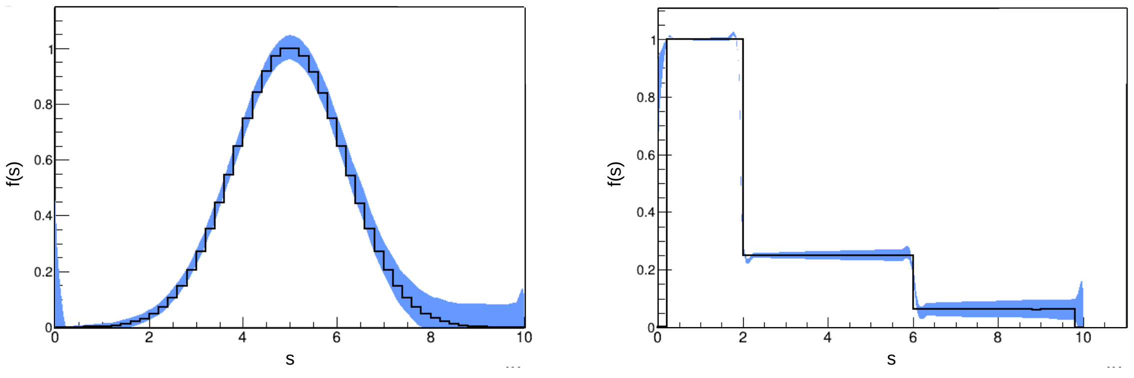

(a) **(b)**

Figure 4.4: Result of deconvolving an artificial signal using Eq. (2.39) for (a) Gaussian, $\mu = 5$ and $\sigma = 2$; (b) a piecewise step function. The 95% HPDI is shown as a shaded blue area. Reproduced from [26] under the terms of the Creative Commons CC-BY license.

gamma function. Finding the $1 - \alpha$ HPDI amounts to solving $F_n(r) = 1 - \alpha$ for r. For a general distribution, $X \sim \mathcal{N}(\mu, \Sigma)$, the HPDI forms a hyper-ellipsoid in x-space, which can be generated from the standard hypersphere. Let $\hat{\boldsymbol{\rho}}$ be an n-dimensional unit vector and R_c be the critical radius found from solving $F_n(R_c) = 1 - \alpha$. This hyper-ellipsoid is then the set of points defined by

$$\mathbf{h} = \boldsymbol{\mu} + R_c L^{-1} \hat{\boldsymbol{\rho}}, \tag{4.32}$$

where $\Sigma = LL^T$ is the Cholesky decomposition of the covariance matrix, which is guaranteed to exist due to the positive semi-definite nature of Σ. It can also be shown that Eq. (4.31) and Eq. (4.32) are equivalent to Eq. (4.27) in the case $n = 1$.

The procedure outlined above was tested using two input functions, chosen to determine the ability of the Bayesian reconstruction to reproduce overall spectral shape and localised features. Choosing a function $f(s)$ as the signal, an input for the deconvolution algorithm is generated using Eq. (4.8) with the kernel defined by Eq. (2.39). The units of s are arbitrary for this consideration. Poisson generated noise is added to the convolved signal to emulate the noise present in a full simulation or experiment. Fig. 4.4a shows the reconstruction of a Gaussian function of the form $f(s) = \exp\left[-\frac{1}{2}(\frac{s-\mu}{\sigma})^2\right]$, which nominal values $\mu = 5$, $\sigma = 2$, with the 95% HPDI represented by a shaded region. The deconvolution algorithm reconstructs the entire spectral shape remarkably well, capturing the characteristic Gaussian bell-shape, as well as locating the mean and standard deviation. The HPDI band also matches the shape well, indicating an acceptable level of uncertainty in the reconstruction of $f(s)$.

To determine the performance at reconstructing localised spectral features, a second signal function was chosen to be a piecewise step function with edges located at $s = 2$ and $s = 6$. The resulting deconvolved spectrum for this signal is shown in Fig. 4.4b, where the edges in the signal are clearly reconstructed. The HPDI shows some uncertainty in determining the exact location of the edges due to the lack of a sharp discontinuity there. However, this uncertainty is approximately 6% (3%) for the $s = 2$ (6) edge.

Therefore, in conjunction with the current design of the GRS, the deconvolution algorithm as the capability of reconstructing the incident photon spectra, with a strong fidelity for spectral shape and is able to reproduce characteristic edge features with almost percent-level accuracy. Additionally, this algorithm provides a "boilerplate" method for similar physical problems that reduce to solving a Volterra-type equation. Due to this generality of the problem, developments in machine learning and neural networks could provide a way to further improve the deconvolution algorithm in terms of speed, online diagnostic capability and uncertainty consideration.

4.2 Simulation Studies

The performance of gamma ray spectrometer was analysed in the context of LUXE. For this, Ptarmigan was used to simulate the Compton scattered photons generated by the collision of a laser pulse and a 16.5 GeV electron beam, for a normalised laser intensity of $a_0 = 0.5$ and 7. As discussed in Chapter 2, the energy spectrum of photons produced in the $a_0 = 0.5$ collision shows the Compton edge and a few higher harmonics whereas for $a_0 = 7$, the spectrum becomes smoother and more synchrotron-like. The goal is to use these energy spectra as input for a start-to-end Monte-Carlo simulation of the GRS to determine the efficacy of extracting the photon spectra using the methods outlined previously, and if the spectral shape can be sufficiently resolved to determine the location of the Compton edges.

The GRS was modelled in full within Fluka, including: a 10 µm tungsten converter target; a lead shielding structure and a 50 cm long lead collimator; a dipole magnet with integrated field strength $\int B\,\mathrm{d}x = 1.68\,\mathrm{T\,m}$; and two scintillator screens placed either side of the main

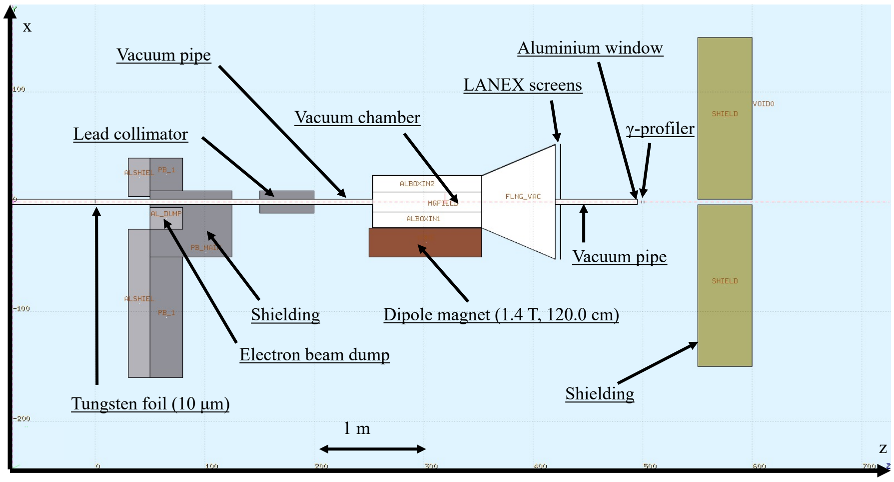

Figure 4.5: Rendering of the simplified LUXE geometry as simulated in Fluka. Reproduced from [21] under the terms of the Creative Commons CC-BY license.

Optical Properties of LANEX (Gd_2O_2S:Te)	
Peak Emission Wavelength	545 nm
Light Yield ($\sim 60-80$ keV)	$6 \times 10^4\ \gamma/\mathrm{MeV}$
Decay Time	~3 µs
Afterglow (>3 ms)	$< 0.1\%$

Table 4.1: Main scintillation properties of LANEX, taken from [129].

gamma beam. Propagation of the gamma beam and produced pairs is encapsulated by an on-axis vacuum pipe to reduce secondary production and subsequent noise. The geometry as rendered in Fluka shown in Fig. 4.5. From the thin target approximation of Eq. (2.43), the fraction of the photon beam that will be converted to e^+e^- pairs is ${}^{N_{\text{pairs}}}/_{N_\gamma} = {}^{t}/_{\lambda_{\text{PP}}} \approx 0.2\%$ for a 10 µm thick target, where $\lambda_{\text{PP}} = {}^{9X_0}/_{7} \approx 4.5$ mm is the mean free path for photon pair production in tungsten. The shielding structure and collimator, with 4.8 cm bore diameter, act in combination to give an acceptance angle of 19 mrad for the produced e^+e^- pairs and the unconverted gamma beam. Two scintillator screens, each 50 cm long in the dispersion axis, are placed either side of the on-axis vacuum pipe, offset by 2.5 cm from the main axis. e^+e^- pairs deflected onto screens by a $z_M = 120$ cm, $B = 1.4$ T dipole magnet, located ~2.5 m after the converter. From the orientation of the magnetic field, electrons are deflected towards positive x and positrons towards negative x. Hence, in Fig. 4.5, the upper detector screen is designated the "electron-" or "e-side" detector and the lower screen, the "positron-" or "p-side" detector.

The following analysis focuses on the case $a_0 = 0.5$, however the same analysis was done for the $a_0 = 7$ case with similar conclusions. The final result of deconvolving the measured positron spectra is shown for both values of a_0. To look at extracting the electron and positron energy spectra, hadronic contributions (e.g. neutrons, protons) were not included in the simulations. The energy deposited in the LANEX screens, which is proportional to the number of scintillation photons produced as in Table 4.1, was scored as in Fig. 4.6. The entire distribution on the e-side and p-side is shown in Figs. 4.6a and 4.6d respectively. A clearly defined signal region can be seen along the dispersion (x) axis, with an approximately one to two orders of magnitude smaller background outside this region. By integrating the signal along the dispersion axis, a measure of the signal-to-background can be estimated as shown in Figs. 4.6c and 4.6f. On the e-side detector, the dominant contribution to the energy deposition and hence scintillation signal is, as expected, the electrons. This indicates that positron noise is negligible on the electron-side of the GRS as electrons and positrons would deposit energy identically in the scintillator. Additionally, although photon fluence could be high through the scintillator, due to their energy, they interact and negligibly lose energy within the thin scintillator layer. For the positron-side detector, similar signal is seen. The dominant contribution is the positron energy deposition, however there is a non-negligble contribution from electron noise within the centre of the signal region.

To extract a profile of the energy deposition along the dispersion axis, the distributions in Figs. 4.6a and 4.6d are integrated in y between -1 cm and 1 cm to produce Figs. 4.6b and 4.6e. The contributions by particle type are also shown. Again, on the e-side screen, electrons are the dominant signal and positrons on the p-side as desired. The non-negligible electron noise is still apparent on the positron-side, however, across the true signal region corresponding to the energy range 1.4 GeV to 8 GeV (see Fig. 4.9b), the mean signal-to-noise ratio is 4.58. This indicates the signal can still be meaningfully extracted from Fig. 4.6e.

Calibration of energy deposition by electrons and positrons in scintillator allows for estimation of the absolute particle number, as well as the spectral shape. The Landau material parameter, ξ_L, is defined as [130, 131]

$$\xi_L = 2\pi N_A r_e^2 m_e^2 \left\langle \frac{Z}{A} \right\rangle \frac{\rho L_z}{\beta^2} \approx 0.154 \left\langle \frac{Z}{A} \right\rangle \frac{\rho L_z}{\beta^2}\ \text{MeV}, \tag{4.33}$$

where $\langle Z/A \rangle$ is the average atomic number-mass ratio, ρL_z is the density of the material in g cm^{-2}

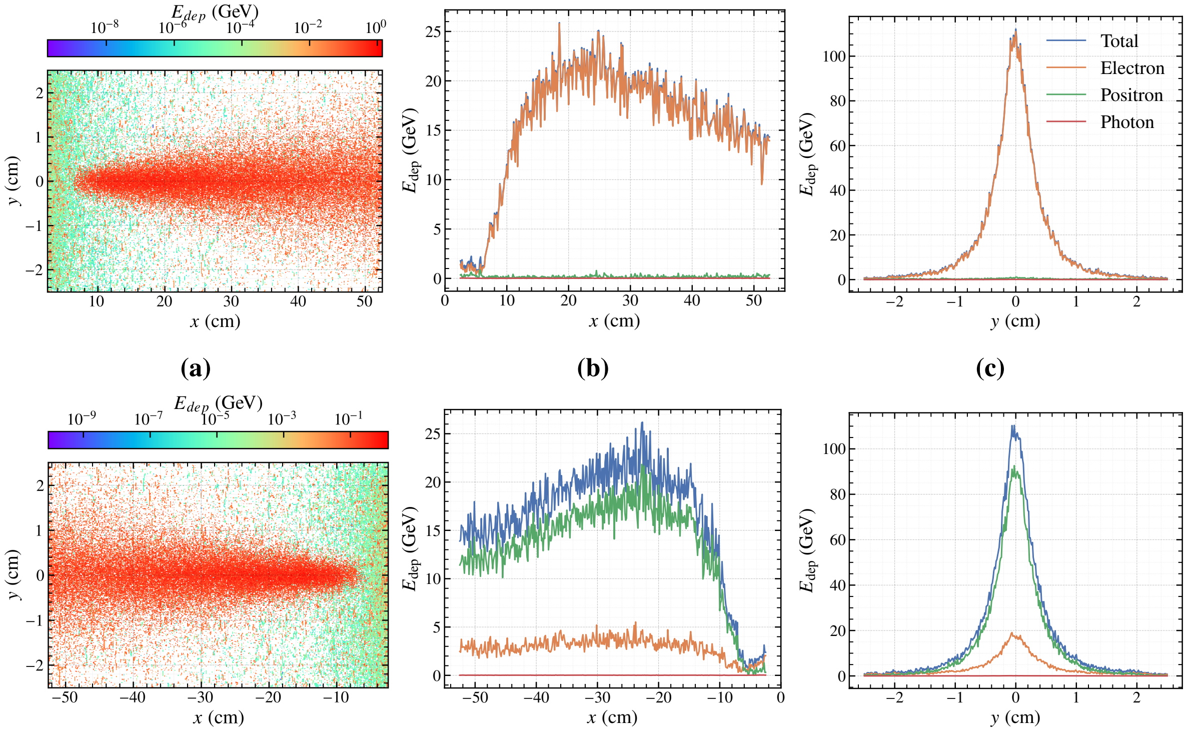

(a) **(b)** **(c)**

(d) **(e)** **(f)**

Figure 4.6: Energy deposition by electron, positrons and photons on the scintillator screens. (a), (d) show the total energy deposited by all particles on the screen on the electron and positron sides respectively. (b) and (c) show the integrated line outs of the energy deposition in y and x respectively for the electron side, and also separated into contribution by particle type. (e) and (f) show the same for the positron side detector.

and β is the velocity parameter of the incident electron/positron. For $L_Z = 1$ mm of LANEX material, the Vavilov parameter is $\kappa = {}^{\xi_L}/_{E_{\max}} \sim 1 \times 10^{-5}$, hence energy deposition is expected to follow a Landau distribution. $E_{\max}$ is the maximum possible energy transfer of the electron during an energy deposition event. The most probable value (MPV) of energy deposition in the ultrarelativistic limit is [132]

$$\Delta_{MPV} = \xi_L \left[\ln \frac{2m_e \xi_L}{\mathcal{E}_p^2} + 0.2 \right], \tag{4.34}$$

where $\mathcal{E}_p$ is the plasma energy of the material. The width of the Landau distribution is also $\approx 4\xi_L$. As the incident particle energy increases, ξ_L approaches a constant value and energy deposition in the material from Eq. (4.34) reaches a Fermi plateau of 0.82 MeV. Hence, to good approximation, for electrons and positrons with energy $\gtrsim$ 10 MeV, energy deposition can be taken to be constant. GEANT4 simulations of a pencil-like electron beam with energies ≥10 MeV interacting with a 1 mm thick plane of Gd_2O_2S corroborate this approximation as seen in Fig. 4.7a. Furthermore, using the photon yield from Table 4.1, the number of scintillation photons produced per incident electron (identically for positrons) is then $\sim 4.92 \times 10^4\ \gamma/\mathrm{e}^-$. The estimated particle number (equivalently, fluence for uniformly sized spatial bins) can be estimated from Figs. 4.6b and 4.6e by scaling by ${}^{1}/_{\Delta_{MPV}}$. The result is shown in Fig. 4.7 (blue) and compared to the true scored particle count (orange).

For the specified dipole magnet, Eq. (4.3) can be used if $\epsilon \gg 500$ MeV for the electrons and positrons. The dispersion function is given numerically as ϵ [GeV] $\approx {}^{766}/_{x\ [\mathrm{mm}]}$, as shown in Fig. 4.8a along with the detection region corresponding to the edges of the screen. In this configuration, the GRS is able to capture electrons and positrons within the energy range 1.5 GeV to 30 GeV. As the maximum photon energy, and hence generated e^+/e^- energy is 16.5 GeV, the spectrometer can resolve up to the maximum energy, corresponding to a position of 46 mm.

To estimate the energy resolution, contributions from the pixelation and the source divergence must be considered as in Eq. (4.5). For a camera containing 2048 pixels each of size 13 µm along a chip of length 2.6 cm, the optical system capturing the scintillation light produced by the LANEX screen must have a magnification $M \sim 1/20$, and hence a spatial resolution of $\delta x \simeq 260$ µm. Additionally, the photon source has an angular divergence of $\theta_\gamma \sim 0.1$ mrad.

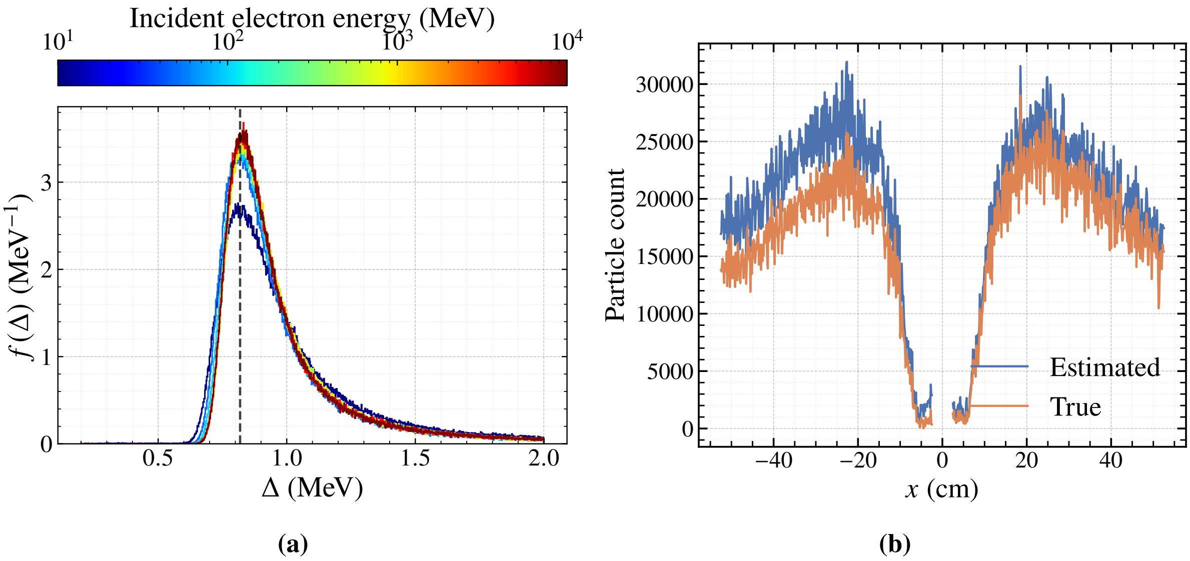

(a) **(b)**

Figure 4.7: (a) Distribution of energy deposited by a monoenergetic electron beam for different incident energies. The theoretical value from Eq. (4.34) is shown as a red dashed line. (b) Electron and positron number distributions as estimated from the energy deposition distributions in Fig. 4.6 (blue) and as measured directly from the scintillator boundary (orange).

From these estimates, it can be seen in Fig. 4.8b that the resolution of the spectrometer is limited by the source divergence. Additionally, the resolution of energies up to 15 GeV is better than 1%.

As Eqs. (4.2) and (4.3) do not take divergent or off-axis particles into account, transforming the spatial distributions in Fig. 4.7 may produce errors in the energy spectrum. Fig. 4.8c shows the energy-position phase space of the positrons entering the p-side detector screen. This distribution is identical to the e-side electrons. The positron signal is highly concentrated around the contour given by Eq. (4.3), indicating that the influence of off-axis particles is negligible. Additionally, the energy-position phase space in the non-dispersed axis is shown in Fig. 4.8d. As expected, this is symmetric about $y = 0$ and also highlights the energy-dependent divergence of the produced positrons.

The transformation of the position-space distribution to an energy spectrum is performed as follows. Using the inverse of Eq. (4.3), the position values are converted to the corresponding energy and binned onto a linear energy scale. The error associated with each bin is determined from the available energy resolution, Eq. (4.5), of each data point contained in that bin, i.e.,

$$\sigma_i^2 = \sum_{j\in i} \left(\frac{\Delta\epsilon}{\epsilon}\right)_j^2 \epsilon_j^2, \tag{4.35}$$

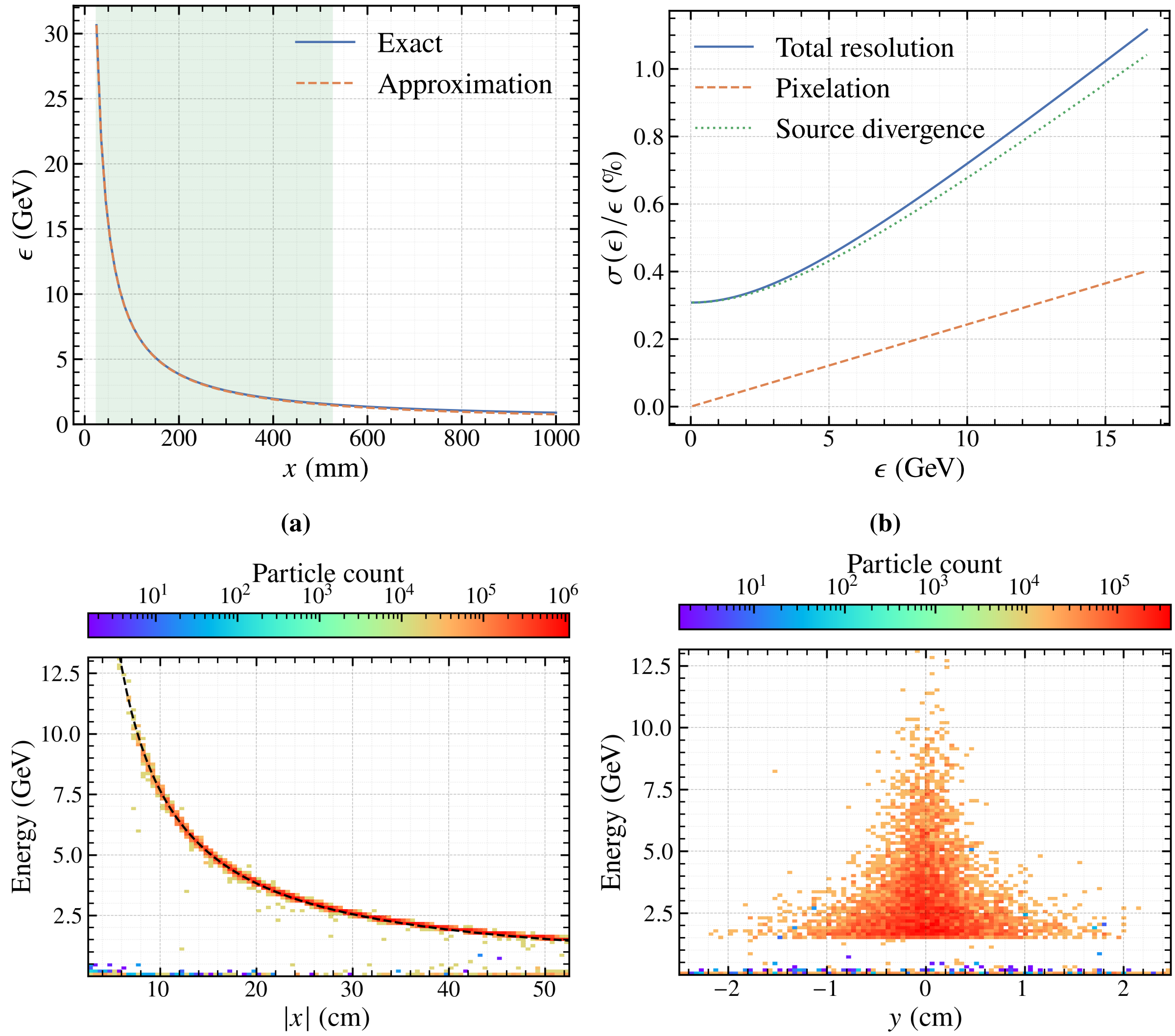

(a) **(b)**

(c) **(d)**

Figure 4.8: (a) Energy-position dispersion relation for LUXE specifications using Eq. (4.2) (blue) and Eq. (4.3) (orange) with the detectable region of the scintillator screens is depicted in green. (b) The energy resolution available to the spectrometer. (c), (d) are simulated energy-position distributions for the positrons entering the positron-side detector. The dispersion function Eq. (4.3) is represented as a dashed black line in (c).

is the squared error of the ith bin containing all j data points. This results in the energy spectra shown in Fig. 4.9a as solid blue and orange lines for the electrons and positrons respectively. These are compared to the true energy spectra as measured directly in FLUKA (dashed lines). Only energies above ≈1.4 GeV appear in the constructed energy spectrum as this corresponds to the edge of the scintillator screen farthest from the main gamma axis. The low energy particles below this threshold apparent in the true spectra are distributed across the detector and are evidently not part of the signal. Furthermore, the fictitious signal above ≈10 GeV occurs due to the presence of noise within the small spatial range 2.5 cm to 7.5 cm when transformed to energy space. However, within the true signal region, 1.4 GeV to 10.0 GeV, the converted and true spectra agree remarkably well both in shape and absolute scaling. It is vital to obtain the correct spectral shape as this contains information on the location of the Compton edge(s) when deconvolved.

The effect of propagation through the GRS setup can be inferred from Fig. 4.9b by comparing the energy spectra of the electrons and positrons at the exit of the converter target and incident on the scintillator screens. Above the detection threshold of the spectrometer (1.4 GeV), the energy spectra are identical within the statistical fluctuations of the Monte-Carlo simulation. Hence, the signal is minimally disrupted during propagation and additionally, noise generated within the set up has a negligible effect on the extraction of the electron and positron signals.

The final step is to reconstruct the incident photon spectrum using the converter positron spectrum in Fig. 4.9b; the choice between electron and positron is arbitrary due to the symmetry of the signals. Additionally, the true converter signal was chosen in order to observe the reconstruction below the threshold of 1.4 GeV. This would not be possible using the measured spectrum, and instead the deconvolved spectrum would be cut off at this threshold. Figure 4.10a shows the reconstructed photon signal compared to the input along with the 95% HPDI. As can be seen, the reconstruction is remarkably accurate, with the edge feature located precisely. At higher energies, the uncertainty in reconstruction increases due to the decrease in signal over several orders of magnitude. Furthermore, a similar analysis and reconstruction of the photon spectrum for the case of $a_0 = 7$ also results in an extremely similar result.

While the Compton edge can be located by eye from Fig. 4.10a, a more rigorous numerical

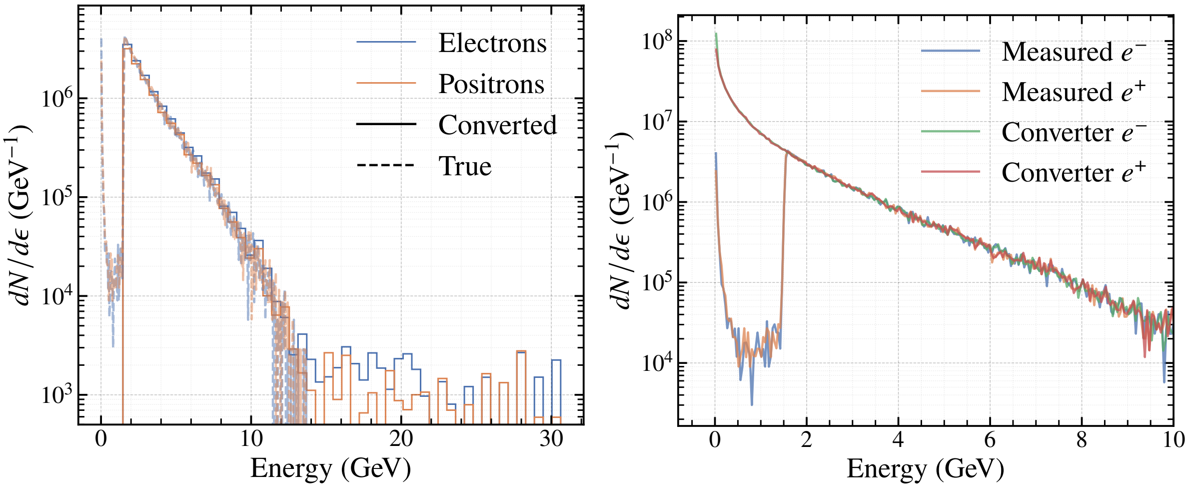

(a) **(b)**

Figure 4.9: (a) Comparison of the electron (blue) and positron (orange) energy spectra found by converting the position-space distributions in Fig. 4.7 (solid) and that measured directly by FLUKA (dashed). (b) Comparison of the electron and positron spectra generated at the converter and after propagation to the scintillator screens.

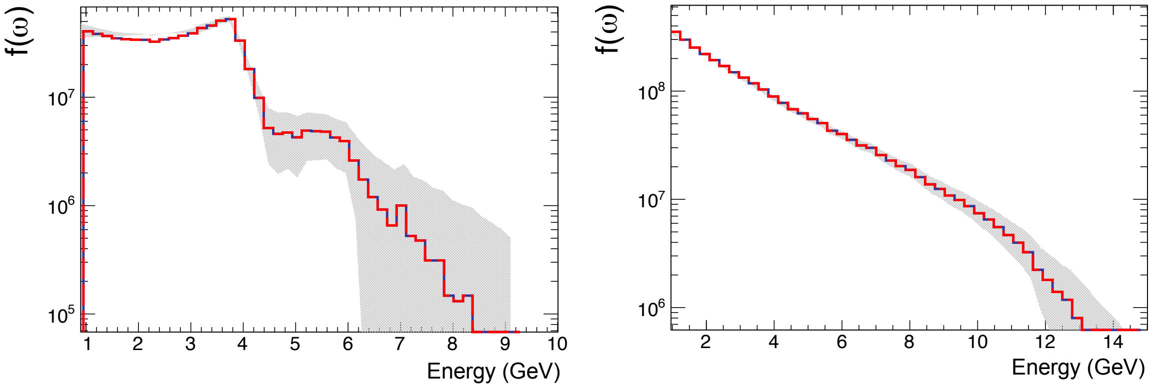

(a) **(b)**

Figure 4.10: Resulting deconvolved spectra for the (a) $a_0 = 0.5$ and (b) $a_0 = 7$ incident photon spectra in GeV^{-1}. The reconstructed spectra are shown in blue with grey shading representing the 95% HPDI. The original input spectrum is shown in red. Reproduced from [21] under the terms of the Creative Commons CC-BY license.

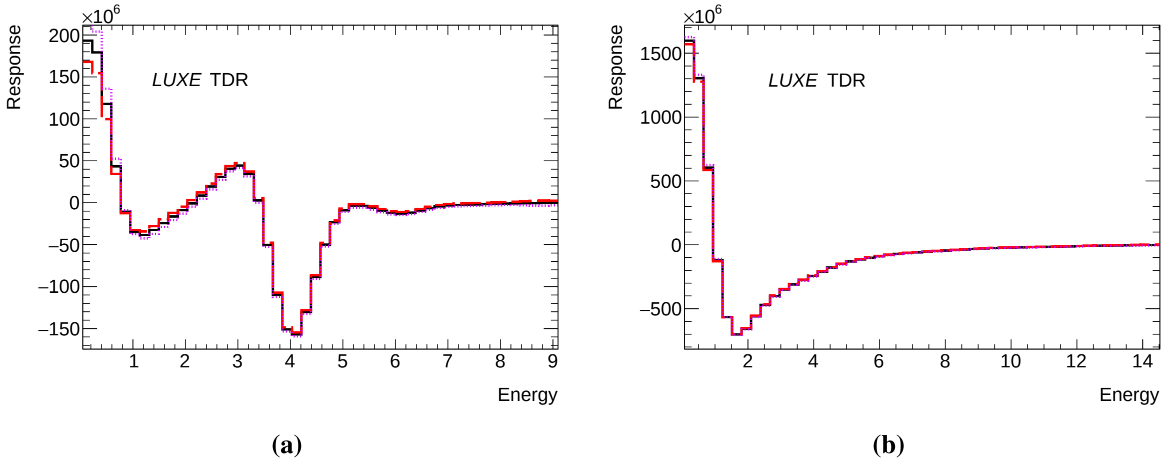

Figure 4.11: Response of the deconvolved photon spectra (blue, solid) to an FDOG FIR filter for (a) $a_0 = 0.5$, and (b) $a_0 = 7$. The response of the lower and upper bounds of the HPDI (red, dashed and purple, dotted respectively) are also shown. Reproduced from [21] under the terms of the Creative Commons CC-BY license.

approach is beneficial for more precise quantification of the edge, as well as automating the process. One method utilises the properties of finite impulse response (FIR) filters, with a rough argument for their operating principle given below. A more detailed discussion of the application of FIR filters to edge finding is discussed in [21, 133]. Consider a signal function $g(x)$ with some edge-like feature, and a filtering function $h(x)$. The convolution of these functions is deemed the response function, $R(x)$, and is given by

$$R(x) \equiv (h * g)(x) = \int_{-\infty}^{\infty} h(\zeta)\, g(x - \zeta)\, \mathrm{d}\zeta\, . \tag{4.36}$$

Taking the derivative of the response filter and evaluating at a specific point, x_0, introduces the derivative $g'(x - \zeta)$ into the integrand of Eq. (4.36). If, within the neighbourhood of an edge at $x = a$, the function $g(x)$ behaves like a step function, the derivative will take the form $g'(x) = \delta(x - a)$, a shifted Dirac-delta function. Hence, the integral above evaluates to $R'(x_0) = h(x_0 - a)$. If the filter function is chosen such that $h(x)$ has a root at $x = 0$ only, then the requirement $R'(x_0) = 0$ is satisfied only if $x_0 = a$. Hence, the response function has an extremum at the location of the edge in $g(x)$. This principle applies even to functions with edges that may not be considered "sharp" - i.e. discontinuous - as in Fig. 4.10a. The use of a discrete filter rather than a continuous one is from the binned nature of the spectral data.

[133] suggests that an optimal filter choice is the first derivative of a Gaussian (FDOG),

which satisfies the $h(0) = 0$ property mentioned above. Figure 4.11 shows the response function, $R(x)$, when such a filter is applied to the reconstructed photon spectra for $a_0 = 0.5$ and $a_0 = 7$ in Fig. 4.10. For the $a_0 = 0.5$ case, the Compton edge is located at 4.1 ± 0.1 GeV, where the uncertainty is given by the width of the energy bin as the lower and upper bounds of the HPDI give the edge location to within the same bin. This value is in agreement with the prediction of Eq. (2.17). Interestingly, although no edge is discernible to the naked eye in Fig. 4.10b, the FIR filter produces a minimum value in the response at 1.8 ± 0.1 GeV. This would correspond to the $\ell = 14$ harmonic, according to Eq. (2.17).

4.3 Experimental Testing

The first experimental characterisation of the GRS was performed at Apollon Laser Facility as part of a laser-wakefield experiment [26]. The facility enabled the delivery of laser pulses with an on-target energy of 12.5 ± 2.5 J in a 37.6 ± 12.5 fs FWHM pulse duration at a repetition rate of 1 shot/min. Laser pulses were focused to a 66 µm FWHM waist focal spot, which contained 37% of the energy, using an $f/60$ spherical mirror, corresponding to a peak intensity of $(2.8 \pm 1.1) \times 10^{18}$ W cm^{-2}. GeV-scale, high-charge electron beams were generated via LWFA by focusing the laser onto a gas cell target of variable length between 10 mm and 25 mm. The resultant beam charge and peak energy were optimised for a plasma composed of 98% H, 2% N, resulting in an electron density of 10^{18} cm^{-3}. By directing electron beams onto a wedged tantalum converter, high-energy and high-flux photons were generated via bremsstrahlung. The exact properties of the photon beam could be controlled by altering the target thickness by translating the converter. For the data used to characterise the GRS, the electron density was kept constant at the stated value and the converter thickness at 1 mm, 69 mm from the rear of the gas cell.

Two lead walls with 10 cm thickness and on-axis bore diameter of 1 cm were positioned behind the converter for shielding. The bore dimension was chosen to give an angular acceptance of 12.6 mrad which minimised noise while not obstructing the gamma-ray beam. A dipole magnet, with 0.46 T m integrated field strength, was located behind the shielding to deflect

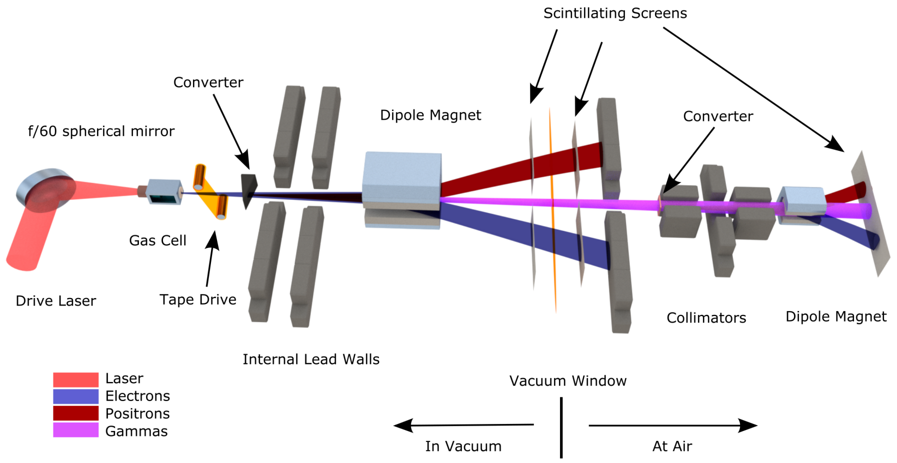

Figure 4.12: Top-view schematic of the Apollon experimental setup. Reproduced from [26] under the terms of the Creative Commons CC-BY license.

electrons and positrons out of the main gamma-ray beam path for further analysis. The gamma-ray beam then exited the vacuum chamber through a 200 µm Kapton window with a 4 mm Perspex supporting layer, before traversing x mm in air and reaching the spectrometer. The thicknesses of the layers forming the window were less than 1% of radiation length respectively, so minimal distortion of the the gamma-ray beam was anticipated; this was corroborated by simulation.

For the spectrometer itself, it consisted of a 225 µm tantalum foil, converting $\sim 4\%$ of the photon beam into electron-positron pairs. Two lead collimators with apertures of 4 mm and 5 mm in the transverse dispersion axis respectively, giving an acceptance angle of 16 mrad, were placed immediately behind the converter target. Following this, generated electron-positron pairs were dispersed onto a LANEX scintillator screen using a dipole magnet with integrated field strength of 4.25×10^{-2} T m. Finally, a scintillator screen placed 650 mm after the rear of the dipole, along with an Andor camera, was used to image the electron-positron signal within a light- and radiation-shielded box to reduce noise.

Examples of typical electron spectra are shown in Fig. 4.13. The average spectrum over the eight shots had a total charge of 207 ± 62 pC above 200 MeV (lowest detectable energy by the electron dignostics) and a maximum energy of 1.71 ± 0.05 GeV. Additionally, the average electron divergence was fitted as a function of energy over the eight shots, and found to be δ [mrad] $= {}^{0.6}/_{(E\ [\mathrm{GeV}])^{1.4}}$. Statistical uncertainties in quoted values were dominated by shot-to-shot fluctuations in the laser and plasma conditions and are accounted for in following

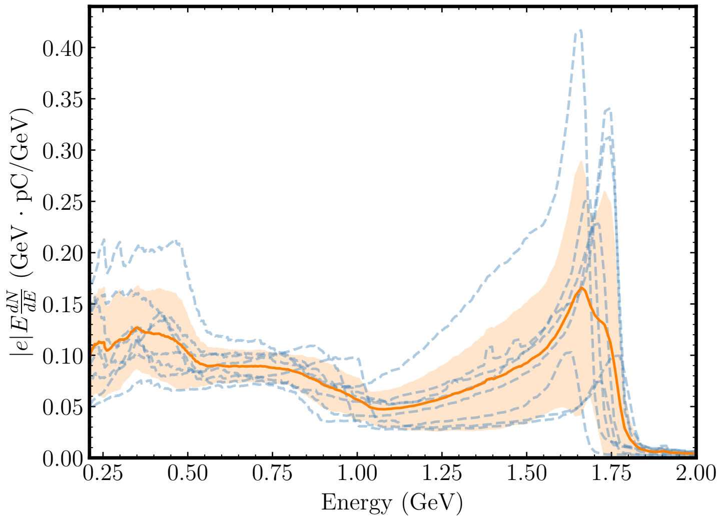

Figure 4.13: Examples of spectral intensity of laser-wakefield electrons generated within the gas cell target for eight consecutive shots (blue, dashed), their mean spectral intensity (orange, solid) and one standard deviation from the mean (orange, shaded). Reproduced from [26] under the terms of the Creative Commons CC-BY license.

simulations. The electron spectra were recorded before the converter target was inserted and bremsstrahlung radiation subsequently generated.

The entirety of the experimental setup in Fig. 4.12 was modelled in GEANT4, including the bremsstrahlung photon spectrum and the e^+e^- pairs generated in the spectrometer. The average electron spectrum from Fig. 4.13 was used to sample 1×10^8 primary particles as input for the simulations. Primary particle divergence was calculated using the fitted function stated above, and the azimuthal angle was sampled randomly in $[0, 2\pi)$.

In order to determine any scattering effects, the photon spectra immediately after the converter and at the entrance to the spectrometer are compared. As is typical of bremsstrahlung, the photon spectrum is monotonically decreasing up to a maximum energy of $\approx$1.7 GeV, containing $(2.21 \pm 0.66) \times 10^9$ photons with energy greater than 1 MeV and 22 ± 7 mJ of energy.

The scattering effect of the Kapton-Perspex window and the air gap can be identified from Fig. 4.14. Only photons with energy $\lesssim 0.6$ GeV are scattered away from the main gamma-ray beam, showing a reduction in the spectrum. Above this energy, the spectra before and after propagation are identical, with $(1.49 \pm 0.44) \times 10^9$ photons entering the spectrometer, resulting in a total beam energy of 16 ± 5 mJ.

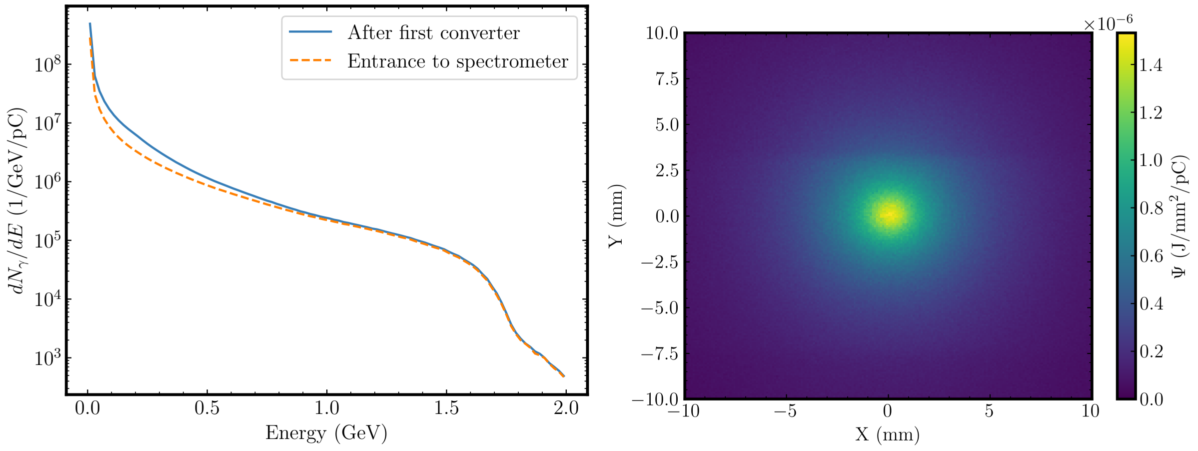

(a) **(b)**

Figure 4.14: (a) Simulated energy spectra per pC of electron beam charge of photons exiting the 1 mm converter (blue, solid) and of photons incident on the gamma spectrometer (orange, dashed). (b) Energy fluence per pC of electron beam charge of the photons incident on the 225 µm GRS converter. Reproduced from [26] under the terms of the Creative Commons CC-BY license.

The survivability of the converter target can also be estimated from simulations. For tantalum, the threshold energy fluence is ~0.016 J cm^{-2} for sustained radiation at 30 Hz [134]. Simulations indicate a peak energy fluence between 0.02 J cm^{-2} to 0.03 J cm^{-2} and a mean energy fluence of 0.016 ± 0.005 J cm^{-2} on the converter. This is between one and two orders of magnitude less than the quoted threshold, indicating minimal degradation of the converter over course of the campaign. No evidence of ablation was observed in experimental findings either, corroborating the simulation results. This is indicative that the GRS is capable of long-term operation on a shot-to-shot basis at this level of energy fluence.

Electron-positron pairs generated by the 300 µm tantalum converter of the spectrometer were also simulated. Their energy spectra and energy-position dispersion map are shown in Fig. 4.15. The energy spectra exhibit a symmetric production of electrons and positrons, except at the high energy edge. This region is sampled less frequently than the lower energies resulting in the mismatch. As positrons can only be produced in this energy regime by pair production, their spectrum is taken as more faithful. The dispersion map shows the relation between the measured transverse position on the scintillator screen and the particle energy due to the dipole magnet. Equation (4.3), the dispersion function, for positrons is plotted in red and overlaid as well. The highest density of positrons can be seen to lie along this curve, with low energy positrons spread across the entire screen. This is attributed to the divergence imparted by the pair production

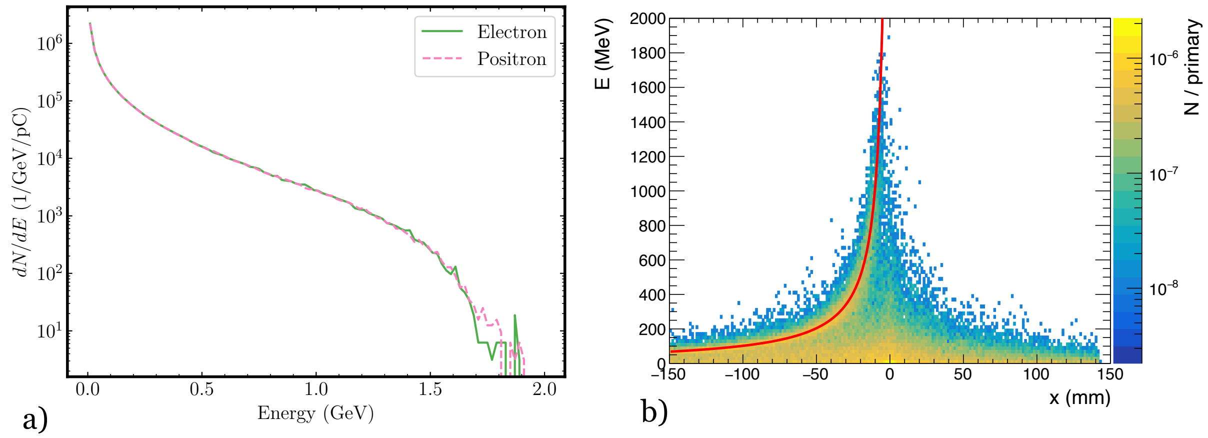

Figure 4.15: (a) Simulated energy spectra of the electrons (green, solid) and positrons (pink, dashed) produced within the GRS converter which reach the LANEX detector. (b) Positron dispersion map indicating the energy and transverse position along dispersion axis on LANEX screen. The deflection function Eq. (4.3) is overlaid in solid red. Reproduced from [26] under the terms of the Creative Commons CC-BY license.

process, which is larger for lower energy particles. As the highest density of positrons lies along the dispersion curve, its functional inverse is used to transform the position space to energy space in the following analysis.

The dispersed electron-positron pairs were incident on a LANEX scintillator screen which was imaged by an Andor camera. Due to the experimental configuration, a mirror was used to direct the scintillation photons onto the camera, which was placed off-axis to protect it from the remaining unconverted gamma beam. To extract the electron and positron spectra from the image, standard processing and background subtraction techniques were employed. The spatial scale was calculated such that one image pixel corresponds to 255 µm. To account for background, five consecutive shots were taken without the GRS converter in place; these data from these shots were then averaged and subtracted from the eight signal shots. The signal was defined to be contained in the central region corresponding to depicted in Fig. 4.16.

To obtain the position-space spectra, the images were integrated along the non-dispersion axis within this defined signal region. Using the inverse of Eq. (4.3), the position values are converted to the corresponding energy and then binned onto a linear energy scale, as outlined in Section 4.2.

The resulting energy spectra for each of the eight shots are shown in Fig. 4.17 with the simulated positron spectrum from Fig. 4.15 also shown for comparison. A monotonically

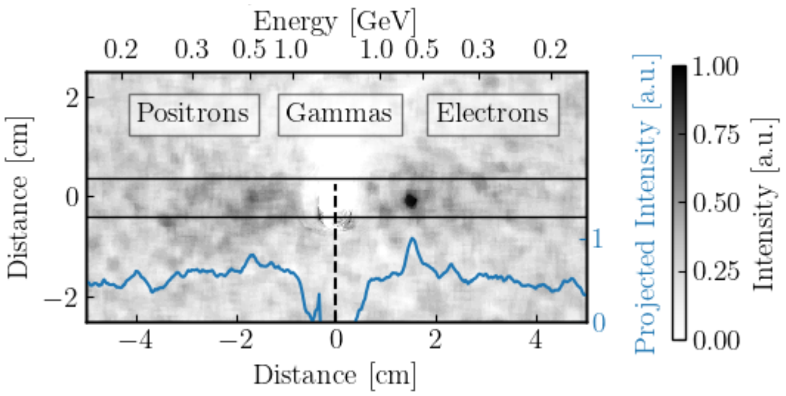

Figure 4.16: Example of a single-shot, background-subtracted image recorded by the scintillator/camera in the gamma-ray spectrometer. The black rectangle defines the signal region, with the integrated lineout in this region overplotted in blue. Reproduced from [26] under the terms of the Creative Commons CC-BY license.

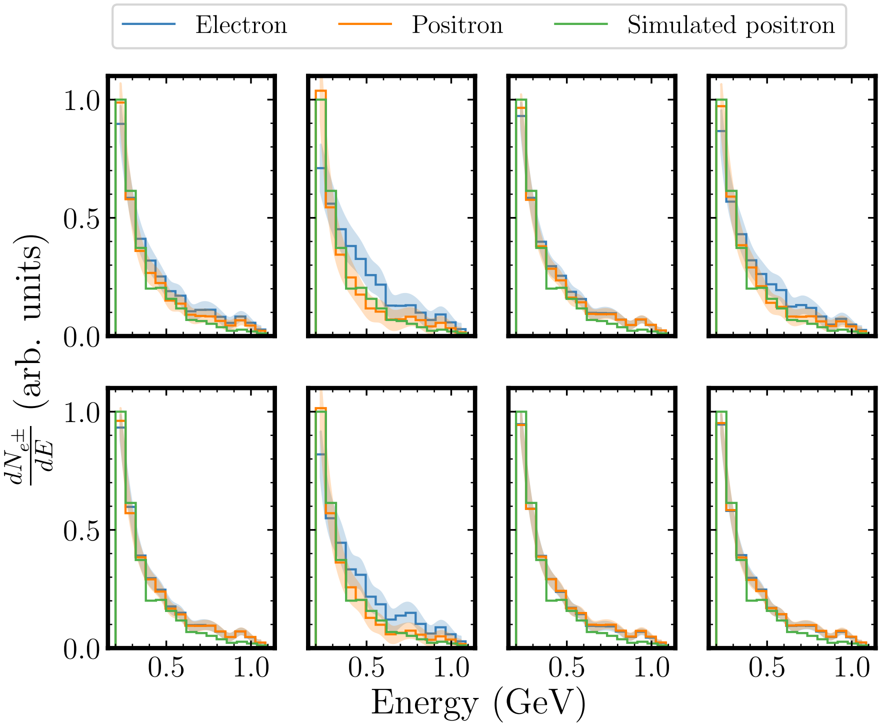

Figure 4.17: Energy spectra of the e^+e^- pairs measured at the back of the spectrometer with corresponding uncertainty (shaded). Experimental results are compared to the positron energy spectrum extracted from simulations (green). Reproduced from [26] under the terms of the Creative Commons CC-BY license.

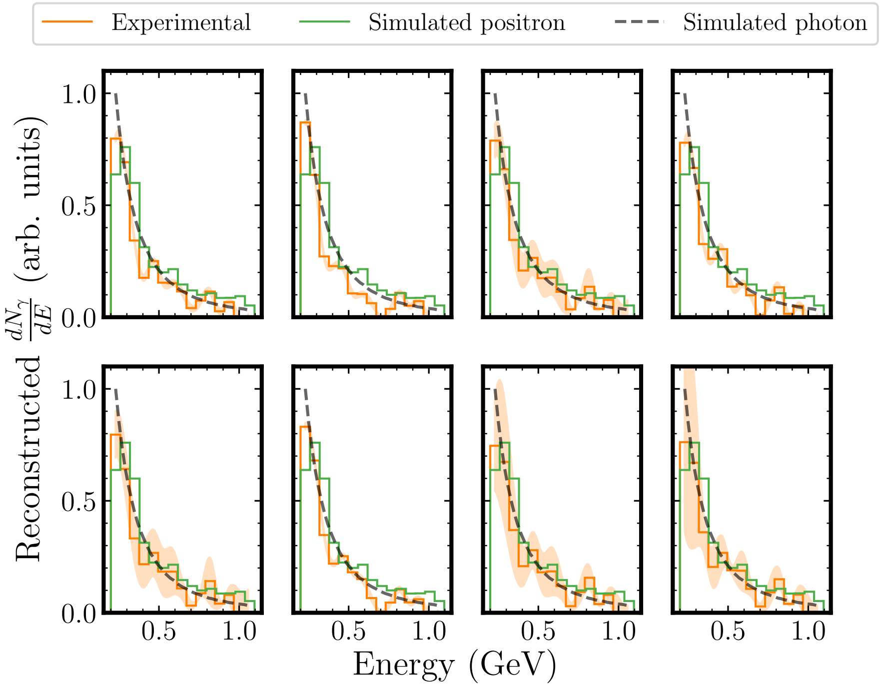

Figure 4.18: Reconstructed photon spectra obtained by applying the deconvolution algorithm to the experimental (orange) and simulated (green) positron spectra in Fig. 4.17. The overlaid dashed line shows the photon spectrum incident on the spectrometer from simulation, as in Fig. 4.14(a). Shaded bands represent the 95% HPDI calculated by the algorithm. Reproduced from [26] under the terms of the Creative Commons CC-BY license.

decreasing shape for the spectrum is as expected, originating from a bremsstrahlung source. The lower limit of 200 MeV is the lowest possible energy that can be measured by dispersion, while the upper limit of 1.1 GeV corresponds to the smallest dispersion on the scintillator screen which lies outside of the central region containing the unconverted gamma beam and hence be resolved as signal.

Using the extracted electron and positron signals in Fig. 4.17, the reconstruction of the photon spectrum follows the procedure outlined in Section 4.1.3. As pair production is symmetric for electrons and positrons, the analysis focuses on positrons, as electrons are susceptible to increased noise due to additional potential generation or scattering mechanisms. Electron data is, however, useful for cross-checking results and ensuring consistency. For the prior mean, $\mathbf{x}_0$ in Eq. (4.24), the "naive" solution to Eq. (4.11) is used. This is then regularised by the statistical approach.

Figure 4.18 compares the deconvolution of the experimental positron spectra with the deconvolution of the simulated positron spectra and the simulated bremsstrahlung spectrum. The shaded orange region depicts the 95% HPDI of the experimental deconvolution result. The results agree well and are consistent with simulations within this uncertainty region. Although the reconstructed spectrum fluctuates, it exhibits the general shape of the bremsstrahlung spectrum within the energy interval used.

The first experimental test of the spectrometer has been completed, demonstrating promising results. This GRS design is able to resolve the shape of the photon spectrum within the uncertainty, while the absolute scaling can be obtained from additional measurements, for instance total photon flux. A clear algorithm has been developed for analysing the data obtained from the spectrometer, with the mathematical principles highlighted in Section 4.1.3. Unfortunately, the full spectral range of photons could not be measured, which consequently affects the reconstruction. This can be mitigated by improving the energy resolution; which can be done by using a dipole with larger integrated field strength, since $^{\Delta E}/_{E} \sim {}^{1}/_{B}$.

4.4 Conclusions

A novel gamma ray spectrometer design for measuring high-flux, high-energy photon beams which operates on the principle of Bethe-Heitler pair production within a high-Z solid target has been presented. Necessary characteristics of the converter target, as well as the magnetic spectroscopy component have been highlighted in order to effectively produce electron and positron signals which can be measured. A statistically-motivated Bayesian deconvolution algorithm to reconstruct the incident photon spectrum has also been outlined, with simple toy models provided as benchmarking of the method.

As the GRS has been developed with the purpose of being a key system in future SFQED experiments, its implementation within the LUXE experiment to measure the energy spectra of photons produced by non-linear Compton scattering during the interaction of an intense laser pulse and a high energy electron beam. Using PTARMIGAN, the photon signal is simulated assuming LUXE parameters, which is then used as input for FLUKA simulations of the GRS implementation envisioned at LUXE. Estimates of the signal-to-noise for the separate electron and positron detectors are given, as well as a systematic methodology for extracting the electron and positron spectra from the magnetically dispersed spatial signal that can be used for experimental data. After extracting the electron and positron spectra, the deconvolution algorithm was applied to each, demonstrating its capability to reproduce the spectral features present in the original photon source such as Compton edges which could be found using an FIR filter technique.

Finally, it was possible to perform the first experimental characterisation of the GRS at a campaign in Apollon. Here, an LWFA electron beam acted as a source to produce a broadband bremsstrahlung photon beam after interaction with a solid target. Although there are no structural features in this bremsstrahlung spectrum like in the LUXE application, the analysis of the GRS data along with the subsequent application of the deconvolution algorithm demonstrated that it was possible to reconstruct the archetypal shape of the bremsstrahlung spectrum within the given energy limits. Unfortunately, due to the experimental setup, it was not possible to measure the entirety of the electron and positron spectra, which was a source of uncertainty in the reconstruction. However, in future implementations, this can be overcome by using an appropriately sized detector and a magnet with higher integrated field strength, which will provide an increased resolution of the detection system.

Chapter 5

Characterisation of Angular Profiles of Gamma Beams

From Chapter 2, it is evident that the parameter a_0, or equivalently the laser intensity, is a crucial parameter describing the non-linear behaviour of SFQED processes in intense electromagnetic fields. Since the formulation and calculation of an accurate first-principles theory describing charged particle dynamics in such fields is still an outstanding problem, experimental investigation is vastly important for developing insight into these complex interactions. Reliable measurements of a_0 are therefore required in order to provide a meaningful benchmark between experimental results and various, sometimes competing, theoretical models.

Typically, the intensity of focused high-power lasers are indirectly inferred from separate measurements of its energy, pulse duration and focal spot size [135], where the latter is frequently measured only at reduced power. This method, however, is prone to significant uncertainties and usually neglects important factors such as the presence of longitudinal fields within the tight laser focus [136] or potential electron-laser spatiotemporal misalignment. Alternative approaches utilising photoionisation of low-density gases [137, 138], or measurement of the spatial profile of Thomson-scattered electrons [139, 140] have also been investigated, but are of limited applicability for on-shot measurements in SFQED experiments.

A recent proposal discussed the viability of using the characterisation of the transverse angular profile of Compton-scattered photons as a method to estimate the laser intensity at the interaction point [95, 52, 141]. The disadvantage of this approach is the a priori dependency on a specific model for radiation reaction, the aptness of which is in turn determined by a_0. This makes this method less applicable in situations where the underlying physics is to be investigated, for example probing the transition regimes of SFQED. The idea was further developed in [142] to be model-independent, where the intensity was inferred from the energy-weighted angular distribution within a few-percent uncertainty. Unfortunately, at high energy and flux, the direct measurement of this energy-weighted profile is challenging, bearing similarity to the measurement of the photon spectrum in this regime discussed in Chapter 4. This chapter details an analogous procedure using the number-weighted profile of the Compton-scattered photons, which has been published in [143], showing that it is possible to use a single formula involving only a measurement of the transverse profile size, along with the initial and final electron energy spectra, to infer the intensity at interaction over a large range of parameters. Additionally, this method was shown to be valid for different radiation reaction models, adopting the same model-independent approach as [142].

This chapter focuses on the details of this inference method, along with discussions of its applicability to focused lasers including spatial misalignment, and its potential limitations for high-χ dynamical regimes. Going further, the use of the gamma beam profiler, proposed within the context of LUXE [20, 21], to extract a measurement of the transverse spatial profile of the Compton-scattered photons is shown and some estimates on its ability to estimate the intensity at interaction are presented.

5.1 Inference of Laser Intensity

5.1.1 Emission Profile for Electrons in a Plane Wave

An electron colliding head-on with a linearly polarised plane wave electromagnetic field will undergo fast quiver motion in the direction of the field polarisation. This oscillatory motion induces the emission of radiation which forms a cone with size proportional to the electric field and inversely proportional to the electron energy.

More explicitly, consider this case for an electron with energy, γm, and the plane wave field

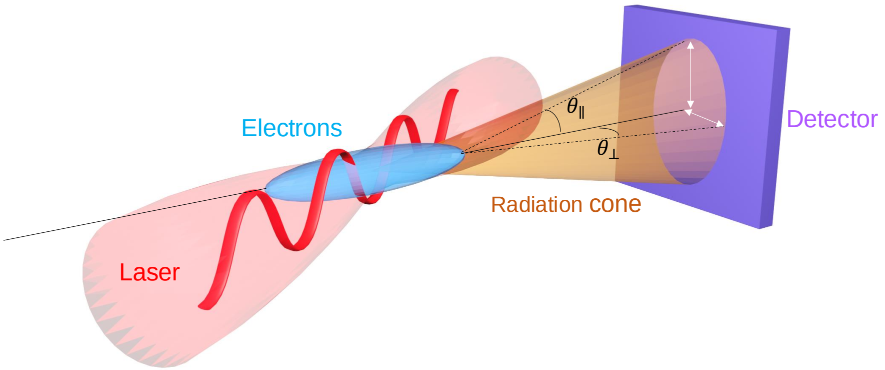

Figure 5.1: Visualisation of an electron bunch (blue) interacting with a linearly polarised laser (red). Here the laser is veritcally polarised with the electron bunch propagating in the horizontal plane. The resultant radiation cone and its transverse profile on a detector plane (purple) are shown as well as the parallel and perpendicular emission angles, $\theta_{\parallel}$ and $\theta_{\perp}$ (marked). Reproduced from [143] under the terms of the Creative Commons CC-BY license.

given by the normalised potential, $a_\mu(\varphi) = a_0 g(\varphi)\varepsilon_\mu \sin(\varphi)$, where a_0 is the peak normalised amplitude, φ is the phase, $g(\varphi)$ is the pulse envelope and ε_μ is the polarisation vector. The field is also monochromatic with frequency, ω_0. The electron's instantaneous momentum makes an angle $\theta(\varphi) = a_0 {}^{\sin\varphi}/_{\gamma}$ with the laser propagation axis and photon emission is assumed to occur predominantly in this direction [33]. Additionally, from Chapter 2, the photon emission rate is $W_\gamma \propto a_0|\cos\varphi|$ for $\chi \ll 1$. Therefore, the mean square (MS) emission angle for one cycle can be calculated as

$$\langle\theta^2\rangle = \frac{\int_C \theta^2(\varphi)\,\mathrm{d}W_\gamma}{\int_C \mathrm{d}W_\gamma} = \frac{a_0^2}{3\gamma^2}, \tag{5.1}$$

where C is any continuous interval of length 2π. The mean square angle, or variance of the radiation profile, parallel to the polarisation axis is then defined to be

$$\sigma_{\parallel}^2 = \frac{a_0^2}{3\gamma^2} + \sigma_{\perp}^2. \tag{5.2}$$

The $\sigma_{\perp}^2$ term represents the mean square emission angle in the direction orthogonal to the laser polarisation and accounts for angular broadening of the beam due to the fact that emission is not exactly coincident with the electron momentum. This term also accounts for divergence in the case of an electron beam rather than a single electron.

Including the pulse envelope and the energy loss of the electron due to recoil upon emission amounts to replacing Eq. (5.2) with

$$\sigma_\parallel^2(\varphi) = \frac{a_0^2 g^2(\varphi)}{3\gamma^2(\varphi)} + \sigma_\perp^2, \tag{5.3}$$

where the electron Lorentz factor is now a function of the laser phase. The total difference in the variances is determined by integrating Eq. (5.3) over the entire pulse weighted by the emission rate, which is now $W_\gamma \propto g(\varphi)$, i.e.

$$\sigma_\parallel^2 - \sigma_\perp^2 = \left(\int_{-\infty}^{\infty} \frac{a_0^2 g^2(\varphi)}{3\gamma^2(\varphi)} \frac{\mathrm{d}W_\gamma}{\mathrm{d}\varphi}\,\mathrm{d}\varphi\right)\left(\int_{-\infty}^{\infty} \frac{\mathrm{d}W_\gamma}{\mathrm{d}\varphi}\,\mathrm{d}\varphi\right)^{-1}. \tag{5.4}$$

Using the Landau-Lifshitz solution for $\gamma(\varphi)$ as in Chapter 2, Eq. (5.4) is generally intractable however closed-form solutions do exist for flat-top and Gaussian envelopes,

$$\sigma_\parallel^2 - \sigma_\perp^2 = \frac{a_0^2}{3\kappa_1}\left[\frac{1}{\gamma_i\gamma_f} + \kappa_2\left(\frac{1}{\gamma_i} - \frac{1}{\gamma_f}\right)^2\right], \tag{5.5}$$

where $\kappa_1 = 1$ ($\sqrt{3}$) and $\kappa_2 = {}^1\!/_3$ (0.315) for a flat-top (Gaussian) envelope respectively, and $\gamma_f = \gamma(\varphi \to \infty)$ is the final electron Lorentz factor after propagating through the pulse.

For a beam of electrons with an initial energy spectrum, ${}^{\mathrm{d}N_e}\!/_{\mathrm{d}\gamma_i}$, the electrons with larger γ_i have a higher emission power and so contribute more to the photon signal. To account for this, Eq. (5.5) can be weighted by $(\gamma_i - \gamma_f){}^{\mathrm{d}N_e}\!/_{\mathrm{d}\gamma_i}$ and integrated over all γ_i. Additionally, Eq. (5.5) was derived using a classical radiation reaction model however for $\chi \gtrsim 1$, quantum effects will become important. The average energy loss of the electrons become reduced by the Gaunt correction factor and stochastic emission results in γ_f not being a single-valued function of γ_i. Under similar assumptions to [142], Eq. (5.5) can be adapted for the initial energy spread and quantum effects by using an average over the initial and final electron energy distributions,

$$\sigma_\parallel^2 - \sigma_\perp^2 = \frac{a_0^2}{3\kappa_1}\mathcal{F}(\gamma_i, \gamma_f; \kappa_2), \tag{5.6}$$

$$\mathcal{F}(\gamma_i, \gamma_f; \kappa_2) \equiv \langle\gamma_i^{-1}\rangle\langle\gamma_f^{-1}\rangle + \kappa_2\Big[\langle\gamma_i^{-2}\rangle + \langle\gamma_f^{-2}\rangle - 2\langle\gamma_i^{-1}\rangle\langle\gamma_f^{-1}\rangle\Big]. \tag{5.7}$$

$\mathcal{F}$ is defined in such a way as to reflect the effects of the electron dynamics on the profile

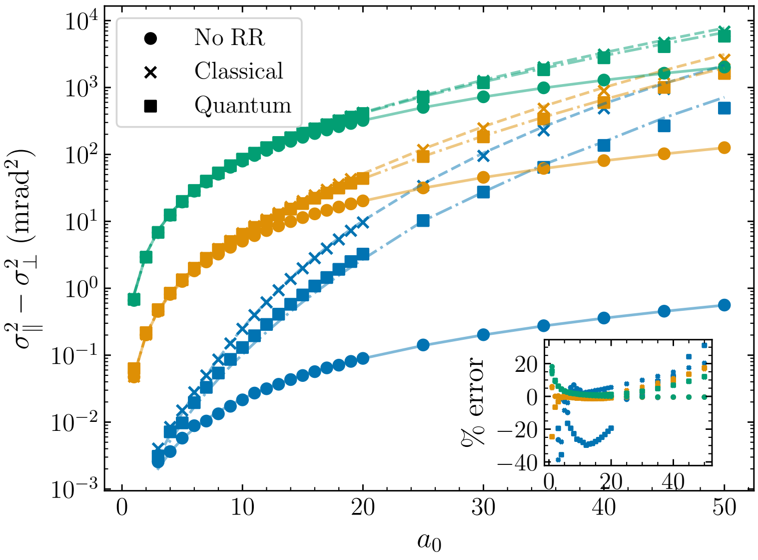

Figure 5.2: Difference in the variance parallel and perpendicular to the laser polarisation axis of the emitted radiation profile by an electron beam with central energy, $\gamma_i m$, 1% RMS energy spread and divergence $\delta = 1$ mrad for: $\gamma_i m = 250$ MeV (green); 1 GeV (orange); and 15 GeV (blue) as predicted by Eq. (5.6) (lines) and calculated from LCFA simulations (points). Different radiation reaction models are considered: no (dots), classical (crosses), and quantum (squares) radiation reaction. The laser is modelled as a plane wave with a Gaussian envelope with FWHM duration, $\tau = 40$ fs and the threshold in emitted photon energy was $\omega_{\text{min}} = 1$ MeV. The inset shows the relative difference between the numerical and analytical results. Reproduced from [143] under the terms of the Creative Commons CC-BY license.

"ellipticity", $\sigma_\parallel^2 - \sigma_\perp^2$.

To determine the accuracy of Eqs. (5.5) and (5.6), the analytical expressions are compared to numerical simulation results in Fig. 5.2. Using Ptarmigan, the head-on collision of an electron beam with a plane wave laser field with a Gaussian temporal profile with FWHM duration $\tau = 40$ fs, wavelength $\lambda = 800$ nm and a range of intensities, $2 \leq a_0 \leq 50$. The electron beam was modelled as cylindrically symmetric with radius $r_b = 0.5$ µm, an RMS divergence $\delta_e = 1$ mrad and a 1% energy spread ($\Delta\gamma_i$) for different initial energies $\gamma_i m = 250$ MeV, 500 MeV and 15 GeV. No appreciable effects were seen in additional simulations, with $\Delta\gamma_i$ ranging up to 10%. Additionally, different radiation reaction models were considered: no radiation reaction (electrons do not lose energy upon emission); the classical Landau-Lifshitz model with continuous energy loss along the electron trajectory; and a fully quantum model including the reduced emission power and stochastic events along the trajectory. The emission rates are determined in the LCFA framework here and pair production in the laser field was neglected, the consequences of which are discussed later.

A good agreement of the simulated results (points) and the predicted results from Eq. (5.6) (lines) can be seen in Fig. 5.2 across six orders of magnitude for $\sigma_{\parallel}^2 - \sigma_{\perp}^2$ for each initial electron energy and radiation reaction model with a relative error of less than $\sim 25\%$. It should be noted that errors of this magnitude occur at the more extreme values of a_0 ($a_0 \lesssim 5$ and $a_0 \gtrsim 20$) for the no RR and classical RR models, however in the intermediate range, the error is much smaller, on the order of a few percent. The source of this increased error in the extremes is discussed in further detail in Section 5.1.3. For $\gamma_i m \lesssim 1\,\mathrm{GeV}$, the classical and quantum RR models give quite similar results but for large electron energies and hence χ, the broadening of the gamma profile is overestimated by the classical model compared to the quantum. This is due to the "Gaunt-modified" emission spectrum of the quantum model, where the average radiated energy is lower by a factor $\langle g(\chi)\rangle$ than the classical Landau-Lifshitz prediction. Further, for $\chi \gtrsim 0.1$, the probabilistic nature of RR becomes non-negligible and radiation is no longer continuous, allowing for both straggling and quenching effects [64, 65, 66].

In order to calculate the variances $\sigma_{\parallel}^2 - \sigma_{\perp}^2$ from the simulation results, an energy cut, $\omega_{\min} = f_{\min}\gamma(\varphi)m$ with $f_{\min} \in [0, 1]$, is required to remove the divergent behaviour of the low-energy, high-angle photons that are emitted, particularly for $a_0 \sim \mathcal{O}(1)$. For the results shown above, a nominal value of 1 MeV was chosen as representative of an experimentally imposed threshold. For example, [21] describes a setup with a 0.5 mm aluminium window crossing the photon beam path resulting in photons with energy $\omega \lesssim 1\,\mathrm{MeV}$ being sufficiently absorbed or scattered out of the photon cone that is to be measured and negligible effect on high energy photons ($\omega \gtrsim 100\,\mathrm{MeV}$). In general, the precise value of an energy cut is experiment specific however the results shown here are robust over a wide range of detection thresholds (four orders of magnitude).

Figure 5.3 shows the application of a range of energy cuts from 0.1 keV to 1 MeV in extracting the variance information from the transverse photon profile using the $\gamma_i m = 1\,\mathrm{GeV}$ electron beam with a quantum RR model. Without an energy threshold applied (black points), $\sigma_{\parallel}^2 - \sigma_{\perp}^2$ does not exhibit a well-defined behaviour for $a_0 \lesssim 20$; however, introducing a cut produces a monotonic trend in $\sigma_{\parallel}^2 - \sigma_{\perp}^2$ which is independent of the exact value of $\omega_{\min}$ across the tested range. Looking at the orthogonal variances separately, applying an energy cut to calculate $\sigma_{\perp}^2$

amounts to multiplying by some factor that is dependent on ω_{min} but not on a_0. Conversely, $\sigma_\parallel^2$ has a more complicated dependence on ω_{min} which also varies with a_0; for $a_0 \gtrsim 20$, this dependence becomes independent of ω_{min}.

Figure 5.4 provides insight into this "cancellation" behaviour upon calculating the difference in these variances. As expected for a linearly polarised field, the shape of the angle-energy distribution perpendicular to the polarisation is largely independent of a_0, with the maximum emission angle at a given photon energy $\left|\theta_{\perp,\mathrm{max}}(\omega)\right| \propto \omega^{-l}$ for some constant l. As a rough estimate, $\sigma_\perp^2 \sim \left|\theta_{\perp,\mathrm{max}}(\omega)\right|^2 \propto \omega^{-2l}$, which explains the scaling behaviour of $\sigma_\perp^2$ with ω_{min} as seen in Fig. 5.3. In the plane parallel to the polarisation of the field, the angle-energy phase space distribution changes shape with increasing a_0, such that above a specific energy, ω_C, a plateau forms with the maximum emission angle remaining constant with increasing photon energy. For small a_0, this plateau is small and so changing ω_{min} has a similar effect to $\sigma_\perp^2$. As a_0 becomes larger, the plateau grows and all $\omega_{\mathrm{min}} > \omega_C$ give the same $\sigma_\parallel^2$ and for $\omega < \omega_C$, $\left|\theta_{\parallel,max}(\omega)\right|^2 \sim \left|\theta_{\perp,\mathrm{max}}(\omega)\right|^2$. Hence, upon evaluation of $\sigma_\parallel^2 - \sigma_\perp^2$, the similar contributions from $\omega_{\mathrm{min}} < \omega < \omega_C$ cancel and the difference in the variances is independent of the choice of energy cut.

Moreover, as a_0 increases, the electrons lose more energy as radiation which subsequently reduces the typical photon emission energy over the interaction, i.e. the peak (instantaneous) synchrotron energy $\omega_{\mathrm{peak}} = 0.44\gamma m \chi$ [144]. If the energy threshold is comparable to this mean emission energy, a non-negligible fraction of the photon distribution is removed by the selection and the accuracy of Eq. (5.6) is reduced, as can be seen in the lower right pane of Fig. 5.3. An estimate for the range of a_0 for which the mean emission energy is greater than the energy cut and hence Eq. (5.6) is accurate can be obtained as follows. Requiring that $\langle\omega_{\mathrm{peak}}\rangle \gtrsim 2\omega_{\mathrm{min}}$ and using the definition of the electron quantum parameter, this is equivalent to $\gamma^2 a_0 \gtrsim 2.27\,{}^{\omega_{\mathrm{min}}}\!/_{\omega_0}$. Using the Landau-Lifshitz solution to account for RR for a Gaussian envelope with FWHM duration, τ, with $\mathcal{I}(\infty) = \omega_0 \tau \sqrt{{}^{\pi}\!/_{4\ln 2}}$, this intensity range depends on the selected energy cut as

$$a_0 \lesssim 860 \frac{\lambda\ [\mu\mathrm{m}]}{\tau^{2/3}[\mathrm{fs}]\,\omega_{\mathrm{min}}^{2/3}[\mathrm{MeV}]}. \tag{5.8}$$

For the same parameters as used in the above simulations, a 1 MeV energy cut implies that Eq. (5.6)

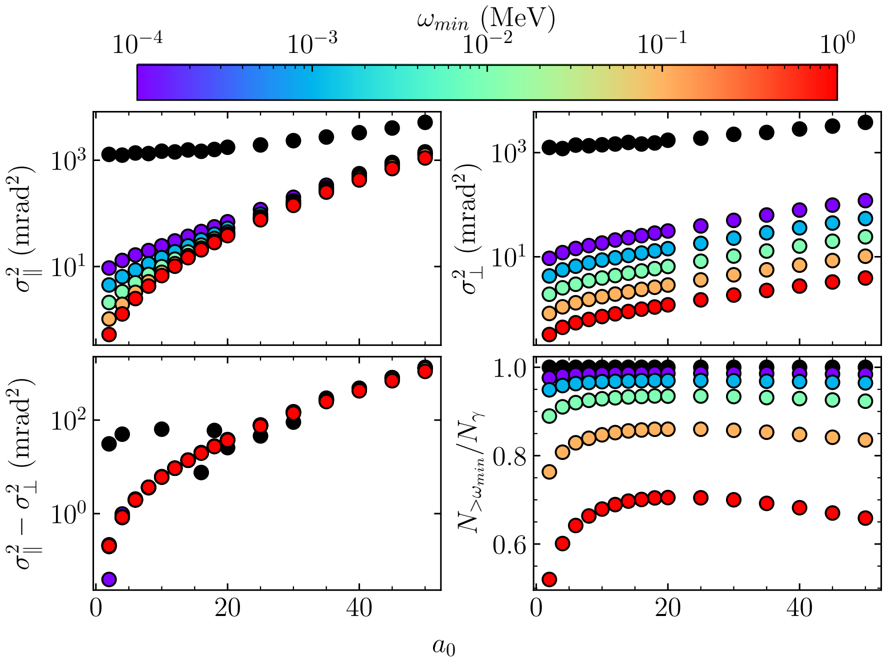

Figure 5.3: Evaluation of the transverse variances, $\sigma_{\parallel}^2$ (top left), $\sigma_{\perp}^2$ (top right) and $\sigma_{\parallel}^2 - \sigma_{\perp}^2$ (bottom left) implementing different energy thresholds $\omega_{\min}$ for the interaction case $\gamma_i m = 1$ GeV across a range of a_0 compared to the corresponding values without an energy threshold (black points). The fraction of the photon beam contained within the selection region is also shown (bottom right).

is accurate for $a_0 \lesssim 70$. Above this intensity, Eq. (5.6) is not necessarily invalidated, rather the measured $\sigma_{\parallel}^2 - \sigma_{\perp}^2$ value may deviate from its predicted value due to the artificially enhanced removal of the signal due to the energy cut. Decreasing ω_{min} to 0.01 MeV increases the range to $a_0 \lesssim 350$. It is important to note that, especially for low a_0, the energy cut cannot be decreased ad infinitum, as per Fig. 5.3, the monotonic behaviour of $\sigma_{\parallel}^2 - \sigma_{\perp}^2$ is lost as $\omega_{\min} \to 0$.

The derivation of Eq. (5.5) and subsequently Eq. (5.6) made some tacit assumptions that are worth addressing. Firstly, the emission rate $W_\gamma \propto a_0 |\cos\varphi|$ is valid only for $\chi \ll 1$ where $W_\gamma \propto \alpha\chi$; whereas in the opposing regime, $\chi \gg 1$, the emission rate scales as $W_\gamma \propto \alpha\chi^{2/3}$. However, due to the normalisation factor in Eq. (5.1), the resulting scaling of the mean-square angle is unaffected except by a constant factor, i.e. $\sigma_{\parallel}^2 \sim a_0^2/\gamma^2$.

A more stringent assumption arises from the neglecting pair production within the field. For $\chi \ll 1$, Breit-Wheeler production is exponentially suppressed and the formation of the radiation cone occurs as above. If pair pair production becomes non-negligible, this will affect the dynamics of photon emission. As higher energy photons are more likely to undergo pair production in the field, there will be a decrease in the high-energy part of the spectrum, resulting

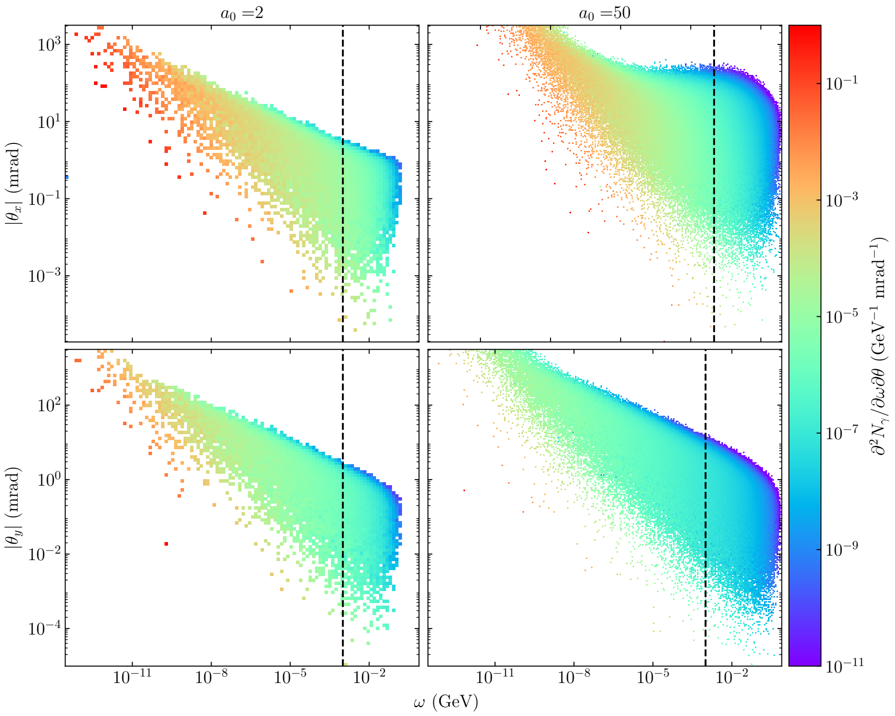

Figure 5.4: The angle-energy phase spaces in the physical plane parallel (top) and perpendicular (bottom) to the laser polarisation for $a_0 = 2$ (left) and 50 (right). A photon energy of $\omega = 1$ MeV is marcated by a black, dashed line.

in a shift in the mean energy. Additionally, if the pulse is sufficiently long, these pairs act as new sources for Compton scattered photons, increasing the size of the radiation cone compared to that predicted by Eq. (5.6). If the number of positrons becomes significant, their contribution must also be accounted for by adjusting the definition of $\mathcal{F}$. Due to this complex interaction, an exact analytical description of the resultant photon profile is currently unattainable; this is discussed further in Section 5.1.3.

5.1.2 Inference of the Laser Intensity

Since $\mathcal{F}(\gamma_i, \gamma_f; \kappa_2)$ contains only dynamical information, Eq. (5.6) is a monotonic function of a_0 meaning that it can be inverted, making it possible to infer the laser intensity from the shape of the photon transverse profile and the electron dynamics:

$$a_0^2 = \frac{3\kappa_1}{\mathcal{F}(\gamma_i, \gamma_f; \kappa_2)}(\sigma_\parallel^2 - \sigma_\perp^2) \tag{5.9}$$

Under the assumption of a cylindrically symmetric electron beam, the effect of the divergence δ_e is removed upon subtraction of the two variance terms. An additional indirect effect on the overlap of the electron beam and focal spot of a focused laser beam is considered later.

Using the same electron-laser configuration as in the previous section, the inferred a_0 by applying Eq. (5.9) to the numerical simulations is compared to the nominal simulations a_0 in Fig. 5.5, again for different initial electron energies and RR models. Across the investigated range of parameters, Eq. (5.9) works remarkably well as an estimation for the nominal intensity, in particular, within 10% of the true value across the entire a_0 range and each RR model except for low intensities ($a_0 < 5$) and high electron energy $\gamma_i m \gtrsim 10\,\mathrm{GeV}$. The inference is most precise for the case of no radiation reaction, as expected since the electron dynamics are trivial with $\gamma_f = \gamma_i$, and reproduces a value of a_0 within $\sim 1\%$ accuracy. For the classical and quantum RR models, Eq. (5.9) still works extremely well but begins to underpredict the correct value as the nominal a_0 increases. Furthermore, for large a_0, radiative cooling of the electron beam may result in sufficient energy loss such that the assumption $\gamma \gg a_0$ no longer holds. Here, the inference becomes less accurate as the average emitted photon energy is of the same order as the employed energy threshold, ω_{min}. The simulations also show that, in order to have accurate inference, the required detection range for the photon cone is $|\theta| \lesssim {}^{2a_0}/_{\gamma_f}$. This is critical for the discussions in Section 5.2.

Since $\sigma_\parallel^2 - \sigma_\perp^2$ and $\mathcal{F}$ are ultimately quantities that are determined by experimental measurement, it is useful to consider the influence of systematic uncertainties on the inference of a_0. Applying the standard error propagation formula to Eq. (5.9), the uncertainty in inferring a_0 can be expressed as

$$\left(\frac{\delta a_0}{a_0}\right)^2 = \frac{(\sigma_\parallel^2 + \sigma_\perp^2)\delta\sigma^2}{(\sigma_\parallel^2 - \sigma_\perp^2)^2} + \frac{1}{4}\left(\frac{\delta\mathcal{F}}{\mathcal{F}}\right)^2, \tag{5.10}$$

$$(\delta\mathcal{F})^2 = (1 - 2\kappa_2)^2 A + \kappa_2^2 B, \tag{5.11}$$

$$A = \Gamma_{i,1}^2 \delta\Gamma_{i,1}^2 + \Gamma_{f,1}^2 \delta\Gamma_{f,1}^2, \tag{5.12}$$

$$B = \delta\Gamma_{i,2}^2 + \delta\Gamma_{f,2}^2, \tag{5.13}$$

where $\Gamma_{\ell,n} \equiv \langle\gamma_\ell^{-n}\rangle$ are the negative moments of the initial and final electron gamma factors.

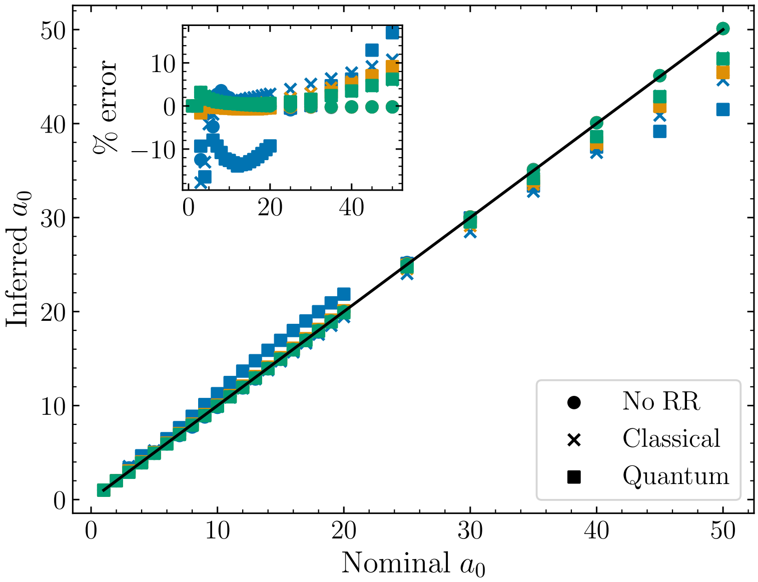

Figure 5.5: Inferred a_0 calculated from the simulation results using Eq. (5.9) vs nominal a_0 (and percentage error, inset) for different radiation reaction models. Simulations assume an electron beam with a $\delta = 1$ mrad RMS divergence, a 1% energy spread, and different initial mean energies: $\gamma_i m = 250$ MeV (green), 1 GeV (yellow) and 15 GeV (blue). Laser pulse was modelled as a plane wave with a Gaussian envelope of FWHM duration $\tau = 40$ fs. The inset shows the relative difference between the numerical and analytical results. The solid black line is shown as a guide for perfect inference. Reproduced from [143] under the terms of the Creative Commons CC-BY license.

$\delta\sigma$ is the uncertainty in measuring the width of the profile and is assumed to be the same in both orthogonal directions. For $a_0 \sim O(1)$, the dominant source of uncertainty comes from the measurement of the transverse variances. In this intensity range, $\sigma_{\parallel}^2 - \sigma_{\perp}^2$ can become very small, resulting in the term containing $\delta\sigma^2$ diverging. For $a_0 \gtrsim 10$, the ellipticity of the profile becomes more pronounced with increasing intensity and since $\sigma_{\parallel}^2 - \sigma_{\perp}^2 \sim a_0^2$ from Eq. (5.6), ${}^{\delta a_0}/_{a_0} \sim \frac{\delta\sigma}{a_0^2}$, i.e. the uncertainty decreases approximately quadratically with a_0. Hence, the measurement of the initial and final electron energy distributions becomes the limiting factor in the precision.

So far, the results presented have been for the idealistic case of a plane wave laser with a Gaussian temporal profile and a pencil-like electron beam. A more realistic scenario requires the consideration of the more complex spatiotemporal structure of a focused laser as well as the finite size of the electron beam. This correction to Eq. (5.6) can be determined using geometrical arguments of the electron-laser configuration. For example, if the laser is focused to a ${}^{1}/_{e^2}$ spot size, w_0, comparable to or smaller than the transverse RMS radius of the electron beam, r_b, the electrons will experience a distribution of intensities. Therefore, the inferred a_0 will be reduced compared to the true nominal peak value by some geometrical factor as the intensity is effectively averaged over the electron spatial distribution. To determine this geometrical factor, β, the laser and electron beam, which is also assumed to be cylindrically symmetric, have the Gaussian profiles:

$$a(x, y) = a_0 \exp\left(-\frac{x^2 + y^2}{w_0^2}\right), \qquad f_e(x, y) = \frac{1}{2\pi r_b^2} \exp\left[-\frac{(x - x_b)^2 + y^2}{2r_b^2}\right], \tag{5.14}$$

where the prefactor of $f_e(x, y)$ is chosen such that its integral over all space is unity. x_b represents a transverse offset that is, without loss of generality, assumed to be along the x direction. The n-th spatial moment, found by averaging over the electron profile, is defined as

$$\langle a^n \rangle = \int_{-\infty}^{\infty} \mathrm{d}x \int_{-\infty}^{\infty} \mathrm{d}y \, a^n(x, y) f_e(x, y) = \frac{a_0^n}{2\pi} \frac{1}{1 + 2n\rho^2} \exp\left(-\frac{n\zeta^2}{1 + 2n\rho^2}\right), \tag{5.15}$$

where $\rho = {}^{r_b}\!/_{w_0}$ and $\zeta = {}^{x_b}\!/_{w_0}$. Since $\sigma_\parallel^2 - \sigma_\perp^2 \sim a^2$ and $W_\gamma \sim a$, the inferred intensity from Eq. (5.9), $(a_0^{\text{inf}})^2$, is given by the average ${}^{\langle(\sigma_\parallel^2 - \sigma_\perp^2) W_\gamma\rangle}\!/_{\langle W_\gamma\rangle}$, i.e. $a_0^{\text{inf}} = \sqrt{{}^{\langle a^3\rangle}\!/_{\langle a\rangle}}$ to lowest order in α. Using Eq. (5.15), the inferred a_0 is then reduced by the geometrical factor $\beta = {}^{a_0^{\text{inf}}}\!/_{a_0}$,

$$\beta = \sqrt{\frac{P}{Q}} \exp\left(-\frac{\zeta^2}{PQ}\right), \tag{5.16}$$

where $P = 1 + 2\rho^2$ and $Q = 1 + 6\rho^2$. This correction is similar in form to that found in [142], only with differences in the numerical factors of P and Q which arise due to the different scalings in the photon number and power emission rate (proportional to a_0 and a_0^2 respectively). In the limit of large r_b and finite x_b, $\beta \to {}^1\!/_{\sqrt{3}}$ independently of the transverse misalignment, therefore the inference of a focused field is predicted to be no worse than $\sim 40\%$ of the true peak value.

The reduction in inferred intensity estimated by Eq. (5.16) was checked against simulations using the 250 MeV and 1 GeV electron beams used in previous simulation studies, except the transverse profile is now given by Eq. (5.14) with $0 < r_b \leq 2w_0$ rather than a pencil-like distribution. This was done for two nominal peak intensities at focus, $a_0 = 10$ and $a_0 = 20$, with

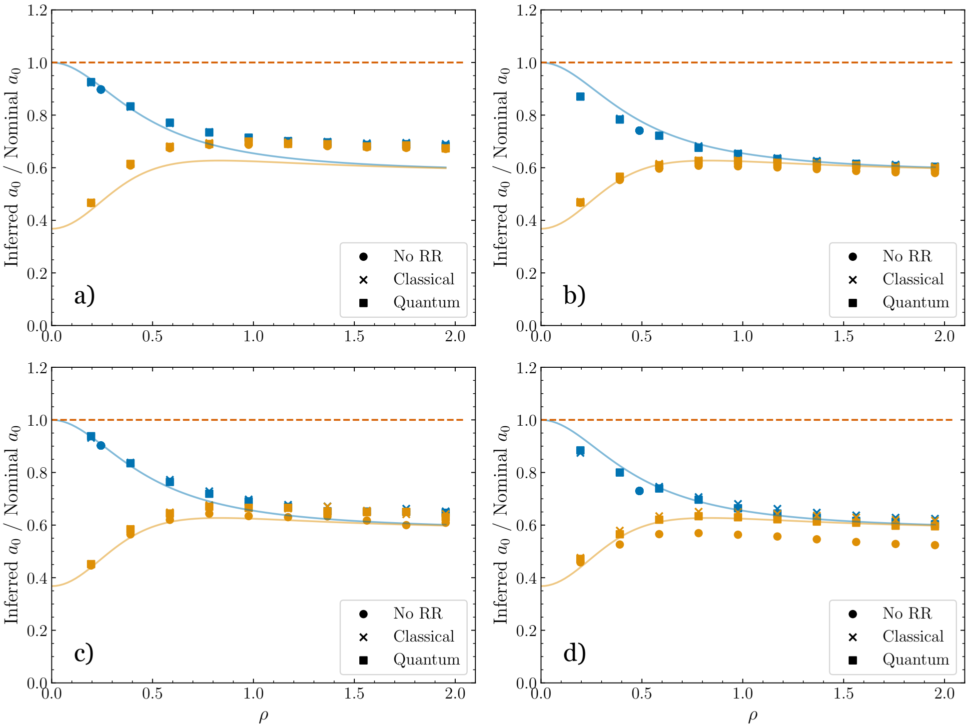

Figure 5.6: Fraction fo the inferred a_0 to the true value as a function of increasing electron beam size for $x_b = 0$ (blue) and $x_b = w_0$ (yellow). The simulated electron beam has a mean initial energy $\gamma_i m = 250\,\text{MeV}$ (a,b) and $\gamma_i = 1\,\text{GeV}$ (c,d) with a 1% RMS spread. The laser pulse was modelled as with peak intensities $a_0 = 10$ (a,c) and $a_0 = 20$ (b,d) and a Gaussian spatiotemporal profile with waist given by Eq. (5.17) and FWHM duration $\tau = 40\,\text{fs}$. Different RR model were also considered. The red dashed line corresponding to perfect inference is plotted as a guide. Reproduced from [143] under the terms of the Creative Commons CC-BY license.

the corresponding focal spot size given by

$$w_0 = 147.839\sqrt{\frac{\mathcal{E}_L\ [\mathrm{J}]}{\tau\ [\mathrm{fs}]}}\frac{\lambda}{a_0}, \tag{5.17}$$

where $\mathcal{E}_L$ is the laser energy (taken here to be 1.2 J) and τ is the FWHM duration (40 fs) of the pulse. The head-on collision of the specified electron and laser beams was simulated for the case of perfect alignment ($x_b = 0$) and moderate misalignment ($x_b = w_0$) with the results shown in Fig. 5.6. It can be seen that increasing the size of the electron beam has an observable effect on the inference using Eq. (5.9), with a reduction by $\sim 30 - 40\%$ as r_b becomes large. This is consistent with the limiting behaviour of Eq. (5.16) for large ρ.

In contrast, for beams with a misalignment, increasing r_b improves the inferred a_0 value as progressively higher intensity regions of the laser field will be experienced by the electrons. As r_b becomes large, a larger fraction of the electron beam interacts with the low-intensity fringes of the laser field where the local, instantaneous χ will be small resulting in the emission of low-energy, high-angle photons. These photons will then be removed by the energy threshold resulting in an under-representation of the angular profile and hence an underestimated value of a_0. For both classical and quantum RR, the increased ponderomotive scattering as electrons lose energy acts to compensate for this underestimation and the inference is subsequently improved compared to the no RR case.

The advantage that the misalignment and finite size of the electron beam compared to the focused laser field can be accounted for by a relatively simple geometrical correction to Eq. (5.9) is that if the peak laser intensity is measured by some alternative means, any spatial offsets can be estimated from the reduction in the inferred intensity with respect to the true nominal value. Additionally, producing a distribution of a_0^{inf} over different shots is sufficient to monitor imperfect pointing stability and systematic effects such as a finite electron beam size can be extrapolated.

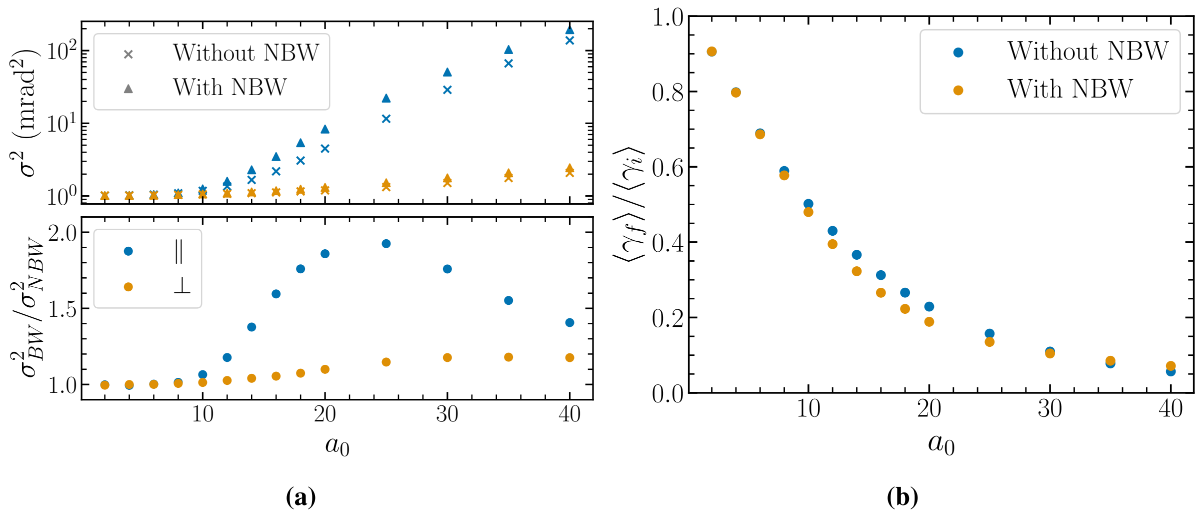

Figure 5.7: (a) Top: profile variances $\sigma^2_{\parallel}, \sigma^2_{\perp}$ (blue, yellow respectively) of the emitted photon profile both without (crosses) and with (circles) pair production enabled in the simulation. Bottom: the relative increase in the profile variances between the disabled and enabled modes. (b) The mean final electron Lorentz factor without (blue) and with (yellow) pair production across a range of intensities. The simulation parameters used were identical to that in Fig. 5.2 for the $\gamma_i m = 15$ GeV and quantum RR case.

5.1.3 Effect of Pair Production on the Transverse Profile

As discussed at the end of Section 5.1.1, pair production by photons in the laser field was neglected in both the derivation of Eq. (5.6) and the simulations to validate it. However, for the $\gamma_i m = 15$ GeV case, $\chi \sim 1$ already for $a_0 \sim 10$, and pair production becomes non-negligible. It is then important to qualify the effect of pair production on the transverse profile and hence the intensity inference, as an analytical description is not currently possible.

Using identical parameters to the simulation of the 15 GeV electron beam from Section 5.1.1 and using a fully quantum model of radiation reaction, an additional series of simulations was performed with pair production enabled in Ptarmigan (NLBWe; non-linear Breit-Wheeler enabled). The variances $\sigma^2_{\parallel}$ and $\sigma^2_{\perp}$, with the 1 MeV energy threshold included, were extracted and are shown in Fig. 5.7a with the no pair-production results also shown for comparison (NLBWd; non-linear Breit-Wheeler disabled). Over the range of a_0 examined, the profile size perpendicular to the laser polarisation, $\sigma^2_{\perp}$, is only weakly affected by the inclusion of pair production, with an increase in size of up to 20% compared to the NLBWd result. In contrast, the NLBWe $\sigma^2_{\parallel}$ deviates from the NLBWd value by as much as 200% at $a_0 \approx 20$ with the deviation decreasing at higher intensities. The disproportionate increase in $\sigma^2_{\parallel}$ compared to $\sigma^2_{\perp}$ can be attributed to the preferential emission of radiation along the laser polarisation direction,

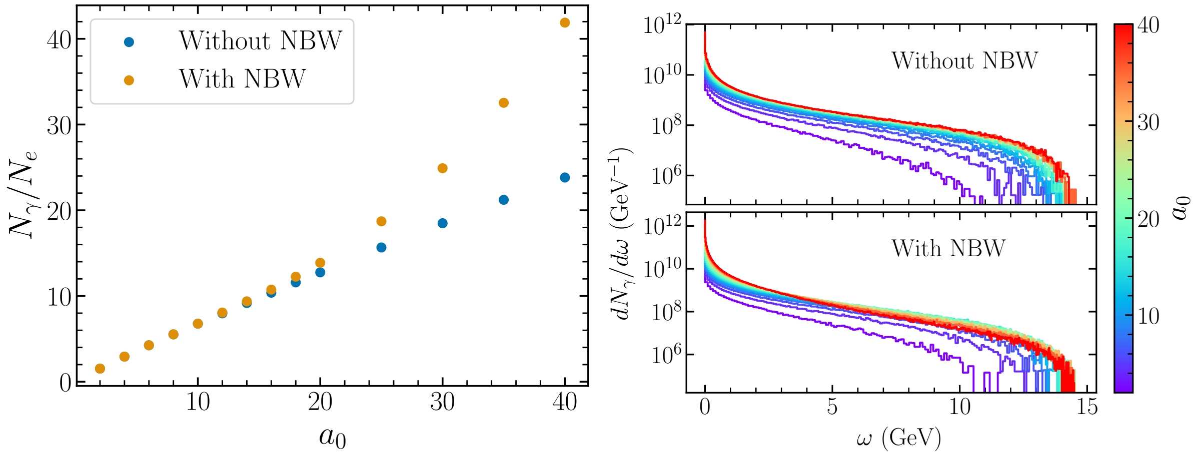

(a)

(b)

Figure 5.8: (a) Number of photons emitted per primary electron for the same simulation parameters as Fig. 5.7 both without (blue) and with (yellow) pair production enabled over a range of intensities. (b) Evolution of the emitted photon spectrum as a_0 increases for the NLBWd (top) and NLBWe (bottom) cases.

which is increased due the increased presence of electrons and positrons which act as additional radiators as well as the incident electron beam. As the intensity increases, the energy loss of the radiators becomes significant, as in Fig. 5.7b, and the local instantaneous χ value drops, reducing the quantum effects of both pair production and radiation reaction. Hence, the electrons and positrons radiatively cool to a quasi-classical state and the emission profile resembles that in the NLBWd case. Additionally, as the instantaneous χ decreases, more photons are produced with lower energies, comparable or less than the energy threshold resulting in an increased removal of photon signal. However, this is compensated for by the exponential increase in the photon number due to formation of a QED cascade at large initial χ. This is clearly seen in Fig. 5.8a, where the photon number increases approximately linearly with a_0 in the absence of pair production but for $a_0 \gtrsim 20$ or equivalently $\chi \gtrsim 2$, the photon number rises exponentially indicating the prolific generation of electron-positron pairs and Compton-scattered photons.

Figure 5.9 shows then the relative error in inferring a_0 for both the NLBWd and NLBWe cases. As expected, for $\chi \ll 1$, pair production is negligible and both simulation modes yield identical inference capabilities. For χ above $\mathcal{O}(1)$, the inference becomes less accurate both with and without pair production as discussed in Section 5.1.1 however the effect of pair production generally increases the relative error by a few percent at most. Evidently, the increase in the profile size seen in Fig. 5.7a is somewhat counteracted by the enhanced radiative cooling and

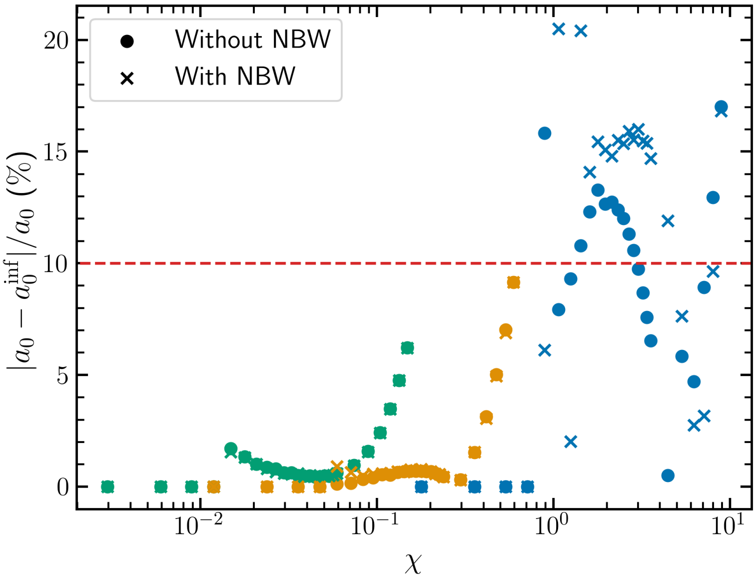

Figure 5.9: Relative error in the inferred a_0 value for the same parameters as Fig. 5.5 with a quantum RR model. Simulations were performed for $\gamma_i m$ = 250 MeV (green), 1 GeV (yellow) and 15 GeV (blue), both with and without non-linear Breit-Wheeler pair production (NBW) enabled. The red, dashed line represents a nominal relative uncertainty of 10% between the true and inferred a_0. Reproduced from [143] under the terms of the Creative Commons CC-BY license.

lower $\langle \gamma_f \rangle$ in the NLBWe case compared to the NLBWd. Nonetheless, as the relative error is only of a few percent order, this is indicative that in this regime, it is difficult to distinguish effects due to stochastic radiation of the electron beam even without additional electron-positron pairs being generated.

The three main assumptions in deriving Eq. (5.6) can be visualised as in Fig. 5.10, where the shaded regions represent the areas of (a_0, χ) parameter space where these assumptions are not met. The emission rates used to derive Eq. (5.6) are calculated using the LCFA framework, which is applicable when $a_0 \gtrsim \mathcal{O}(10)$ with the commonly referenced criterion, $a_0 \gtrsim 5$, depicted here. Additionally, as discussed in Section 5.1.1 with Eq. (5.8), the choice of energy cut limits the maximum a_0 that Eq. (5.6) provides an accurate prediction for. Finally, neglecting pair production, which incurs an uncertainty in inference of a similar order to the quantum stochastic emission effects, is precluded for $\chi \gtrsim 1$. Despite these assumptions not being met in these parameter regions, Eq. (5.9) still provides a reasonable estimate of the nominal intensity within $\sim 20\%$. The adequacy of this uncertainty is strongly case-dependent, however having an error of at most this magnitude over a large parameter range is promising.

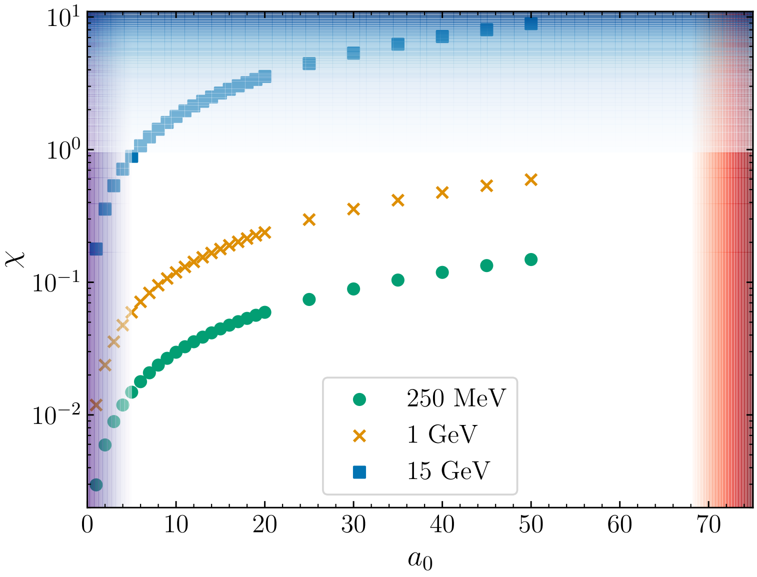

Figure 5.10: Plot showing the regions of (a_0, χ) parameter space where the assumptions used to derive Eq. (5.6) are less accurate due to: the use of LCFA-calculated rates (purple); neglecting pair production (blue); and introducing an energy cut-off in the photon detection (red). Simulated parameters are marked as points for $\gamma_i m = 250\,\mathrm{MeV}$ (green), $1\,\mathrm{GeV}$ (yellow) and $15\,\mathrm{GeV}$ (blue). Reproduced from [143] under the terms of the Creative Commons CC-BY license.

5.2 Measurement of the Transverse Spatial Profile

5.2.1 Propagation of the Photon Profile

In order to measure $\sigma_\parallel, \sigma_\perp$ of the angular profile, the transverse spatial distribution of the photon beam at a known distance from the source can be used to determine the angular information. Consider a photon emitted by an electron at a position $\mathbf{r}_0$ and with momentum $\boldsymbol{k}$ that propagates without obstruction to a detector plane centered on the main propagation axis (assumed to be the z axis), located at $z = D$. Assuming $k_z \gg k_x, k_y$ and $z_0 \approx 0$, the photon trajectory is almost parallel to the propagation axis and $\mathbf{r} \approx \mathbf{r}_0 + D\hat{\boldsymbol{n}}$ is the point at which the photon intersects the detector plane. $\hat{\boldsymbol{n}}$ is a unit vector in the direction of $\boldsymbol{k}$. In particular, the position in the plane of the detector, transverse to the propagation axis, is

$$\mathbf{r}_\perp \approx \mathbf{r}_{\perp,0} + \frac{D}{k_z}\boldsymbol{k}_\perp, \tag{5.18}$$

where the approximation $|\boldsymbol{k}| \approx k_z$ has been used. From a measurement of the transverse location on the detector screen, and assuming $\left|\mathbf{r}_{\perp,0}\right| \ll D$, the momentum direction can be estimated as

$$\begin{cases} \frac{x}{D} & \simeq \frac{n_x}{n_z} = \frac{k_x}{k_z} \equiv \tan\theta_x \\ \frac{y}{D} & \simeq \frac{n_y}{n_z} = \frac{k_y}{k_z} \equiv \tan\theta_y \end{cases} \tag{5.19}$$

For large detector distances, the small angle approximation applies and $x/D \sim \theta_x, y/D \sim \theta_y$.

By measuring the distribution of x, y for the entire photon beam, the variance of the angular distributions can be determined as $\mathrm{Var}[X] = D^2\mathrm{Var}[\Theta_x]$. Hence, a measurement of the transverse spatial profile provides sufficient information to extract the angular variances, and, using Eq. (5.9), the intensity at the interaction can be estimated. This is the principle of the Gamma Beam Profiler (GBP) to be implemented at LUXE; two sapphire-based spatial detectors that are segmented into strips in order to measure the transverse profile of the produced gamma beam in two orthogonal directions [145]. The general functionality of the detector is similar to that of conventional silicon-strip detectors, however sapphire has a higher radiation resistance compared to silicon which is critical at LUXE due to the high-energy, high-flux nature of the photon beam.

With the ultimate aim of using Eq. (5.9) to infer a nominal value for the a_0 of a typical electron-laser interaction anticipated at LUXE, a start-to-end series of simulations were performed for three selected intensities: $a_0 = 5$, 10, and 20 with LUXE parameters for the electron beam and other laser properties. These values were chosen to be representative of the entire range of intensities LUXE will be able to achieve, as well as testing the capabilities of both the detector, at measuring the profile of a high-ellipticity signal, and the intensity inference method, where quantum effects are influential. It is henceforth assumed that the laser is polarised along the x axis, with the laser propagating in the negative z direction. Therefore, the x axis is referred to as the parallel plane, containing the laser polarisation and wavevector, with y denoted as the perpendicular plane. The laser propagation axis is still referred to as the z axis. Using Ptarmigan, the electron beam - laser interaction was simulated for these a_0 and the radiated photons (above an energy threshold of 1 MeV) were recorded and their transverse profiles are shown in Fig. 5.11, normalised to their maximum value. As expected, the increased elongation

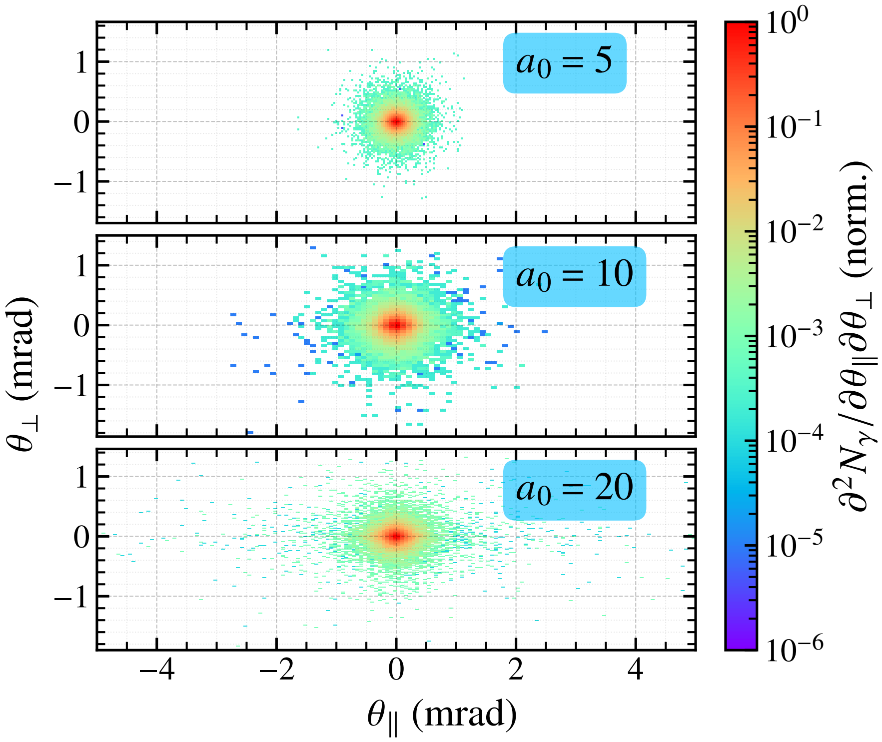

Figure 5.11: Transverse profiles of the photons generated by Ptarmigan for intensities: $a_0 = 5$ (top), $a_0 = 10$ (middle), and $a_0 = 20$ (bottom) with LUXE interaction parameters. The double-differential profiles are normalised to their maximum value for comparison.

of the profile in the direction parallel to the polarisation of the laser is clearly visible.

In Fluka, the photon output in Fig. 5.11 is propagated through the LUXE geometry (see Fig. 4.5) to the GBP plane, located a distance $D = 11.5$ m from the electron-laser interaction point, centred on the propagation axis. Additionally, the profiler has a transverse size of 2 cm × 2 cm, corresponding to an angular detection range of $|\theta| \leq 0.82$ mrad from Eq. (5.19). Figure 5.12 shows the central portion of the profile, expressed as an angle using Eq. (5.19), for each intensity. Here, the elongation does not seem as prominent as in Fig. 5.11; this is due to the restricted angular range that the profiler is able to measure. From Fig. 5.11 for $a_0 = 20$, the maximum angle of the profile is approximately 4 mrad which is ~ 5 times larger than the profiler range. Therefore, the full elongation is not apparent from this profile; the consequences of this are discussed in Section 5.2.2.

During propagation, the photon beam also passes through the 10 µm tungsten converter of the GRS and a 200 µm Kapton window which ends the beam pipe. By comparison to the angular profiles at source, Fig. 5.13 indicates that during the traversal of the LUXE setup, the

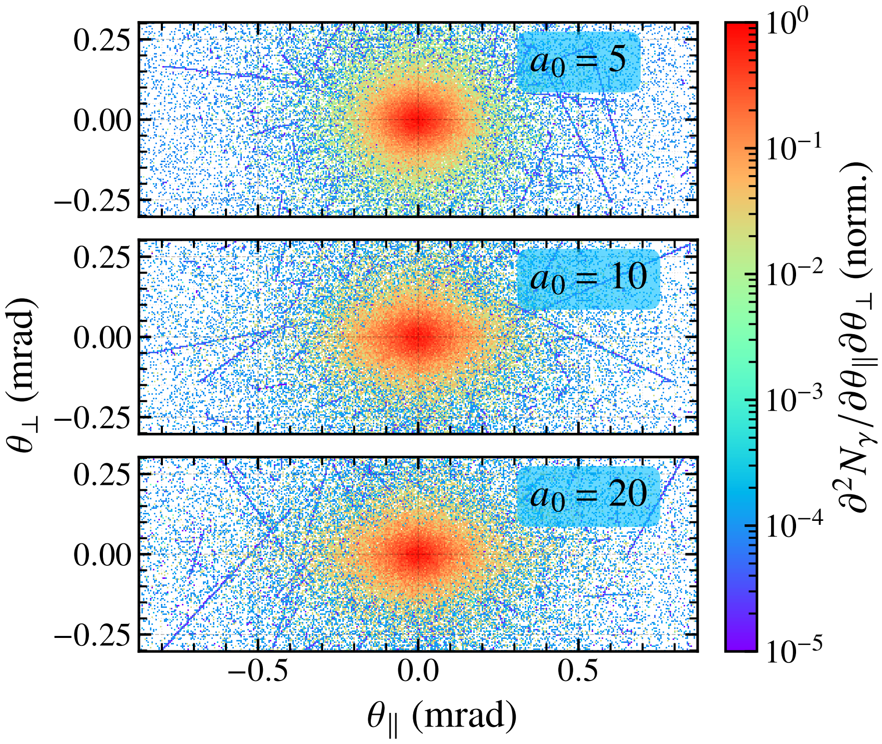

Figure 5.12: Transverse photon profiles as measured in FLUKA simulations of the LUXE geometry, using the distributions from Fig. 5.11 for interaction point intensities: $a_0 = 5$ (top), $a_0 = 10$ (middle), and $a_0 = 20$ (bottom). Double differential profiles are normalised to their maximum values for comparison.

photon beam undergoes minimal distortion with the shape of the profile well maintained. The overall magnitude of the signal may decrease however due to losses via pair conversion in the GRS converter for example, however as discussed in Section 4.2, only a fraction of a percent of the beam is lost to conversion. Additionally, as described in [21], the presence of the Kapton window acts as a natural implementation of the energy cut used to evaluate the variance from the angular distributions in PTARMIGAN, attenuating or scattering the low energy ($\omega < 1$ MeV) photons out of the main photon beam.

5.2.2 Extracting the Transverse Variances

From the distributions in Fig. 5.13, the variances can be determined and then application of Eq. (5.9), along with supplemental information on the electron initial and final spectra, can be used to infer the laser intensity at interaction. The geometric factor in Eq. (5.16) is also required to account for the laser focusing. However, as seen by comparing Figs. 5.11 and 5.13, the profiles measured by the GBP detector are truncated due to the limited detection range. The profiles

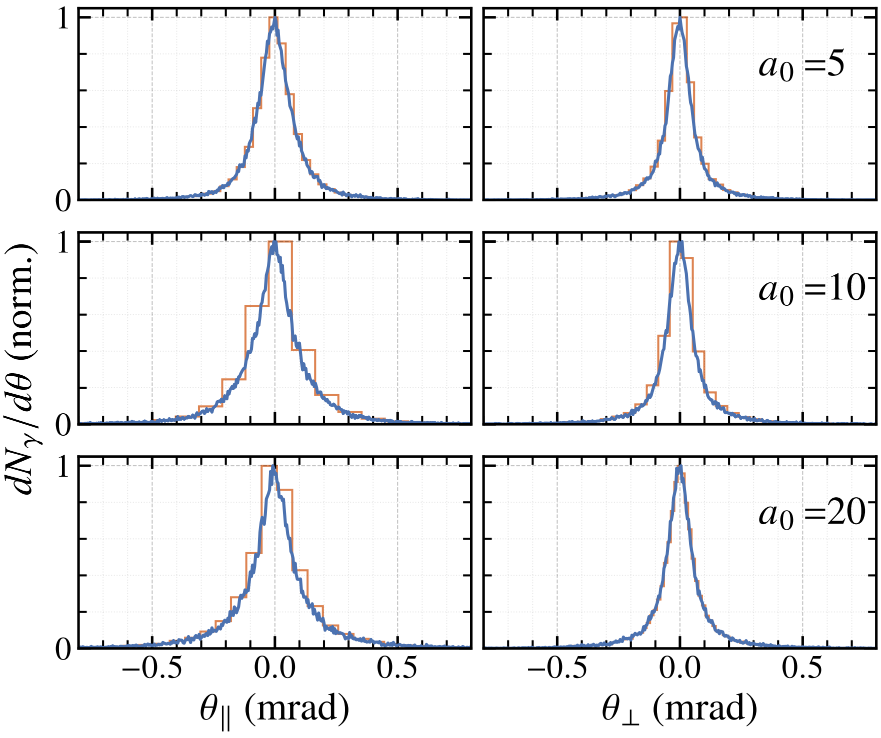

Figure 5.13: Projections of the transverse profile onto the axes parallel (left) and perpendicular (right) to the laser polarisation for each simulated interaction intensity; $a_0 = 5$ (top), $a_0 = 10$ (middle), and $a_0 = 20$ (bottom). The profiles extracted from Fluka simulations (blue) are compared to the original Ptarmigan output (orange) and are normalised to their maximum values.

in Fig. 5.13 are strongly peaked at the centre, and dropping off over several orders of magnitude towards the edges of the profile. Although the tails of the distribution are much smaller than the central region, they are still considered heavy and have a non-negligible contribution to the calculation of distribution moments. Therefore, the truncation due to the detector range will incur some error when used to estimate the variance compared to a full measurement of the transverse profile. This can be resolved by either increasing the detector size, or placing it closer to the source.

Therefore, it is prudent to consider how the maximum detection angle affects the extracted variance of the profile compared to the true maximum angle of the profile, $\theta_{\max}$. Let $f \in [0, 1]$ be the reduction factor such that $\sigma^2(f)$ is the variance of the profile measured within the angular limits $-f\theta_{\max} \leq \theta \leq f\theta_{\max}$. Using the full photon transverse profiles presented in Fig. 5.11, projected into the parallel and perpendicular axes, Fig. 5.14 shows how well $\sigma^2(f)$ estimates the true profile variance, σ^2_{true}, when $f = 1$. In each case, it can be seen that at least 50% of the distribution width must be used in order to estimate the complete variance to within

20% error. Additionally, almost complete accuracy (to within the percent-level error) can be achieved by including greater than ~ 60% of the distribution. It is also worthy to note that this behaviour is true of each distribution for each intensity and projection axis, indicating it is a property of the underlying distribution rather than being explicitly dependent on a_0. Using Fig. 5.11, the approximate θ_{max} in each direction are determined to be: (1 mrad, 1 mrad) for $a_0 = 5$; (2 mrad, 1.8 mrad) for $a_0 = 10$; and (9 mrad, 2 mrad) for $a_0 = 20$ in the parallel and perpendicular axes respectively. Taking 0.82 mrad to be the maximum detectable angle for the GBP, the variance calculated from the $a_0 = 5$ profiles will be the most accurate, with approximately 80% of the profile widths included. For the $a_0 = 10$ case, the coverage reduces to ~ 40%, indicating an estimate of the variance which is only accurate to within $\lesssim$ 25%. Due to the extreme elongation in the parallel direction, only a small fraction (approximately 1/10) of the transverse profile for $a_0 = 20$ is measured in the axis parallel to the laser polarisation. This results in computing a variance which is only 10% accurate, therefore the GBP is of limited utility in this instance for inferring the intensity at interaction as the values of $\sigma_{\parallel}^2, \sigma_{\perp}^2$ will be the dominant source of error. The estimations of the error are corroborated by the calculated results shown in Table 5.1, with the variances extracted from the FLUKA GBP profiles having a relative error matching the predicted magnitude, except for $\sigma_{\perp}^2$ at $a_0 = 20$. In this case, due to the large truncation of the profile in the parallel axis, this affects the resulting projection of the profile onto the perpendicular axis. However, this can be easily solved in principle, either by using a larger detector or by decreasing the distance from the source.

	$a_0 = 5$	$a_0 = 10$	$a_0 = 20$
Full $\sigma_{\parallel}^2$ (mrad)	0.0164	0.0329	0.0894
GBP $\sigma_{\parallel}^2$ (mrad)	0.0167	0.0280	0.0336
% error	-1.95	15.02	62.40
Full $\sigma_{\perp}^2$ (mrad)	0.0136	0.0190	0.0229
GBP $\sigma_{\perp}^2$ (mrad)	0.0142	0.0177	0.0184
% error	-4.31	6.67	19.62

Table 5.1: Summary of the profile variances estimated from projections parallel and perpendicular to the laser polarisation axes for each simulated interaction intensity, both for the full transverse profile as generated by PTARMIGAN (full) and those measured from FLUKA simulations (GBP). The relative error to the true variance from the full profile is also included.

For LUXE, the electron and laser parameters are such that $\chi \gg 1$ even for $a_0 \sim 1$, and

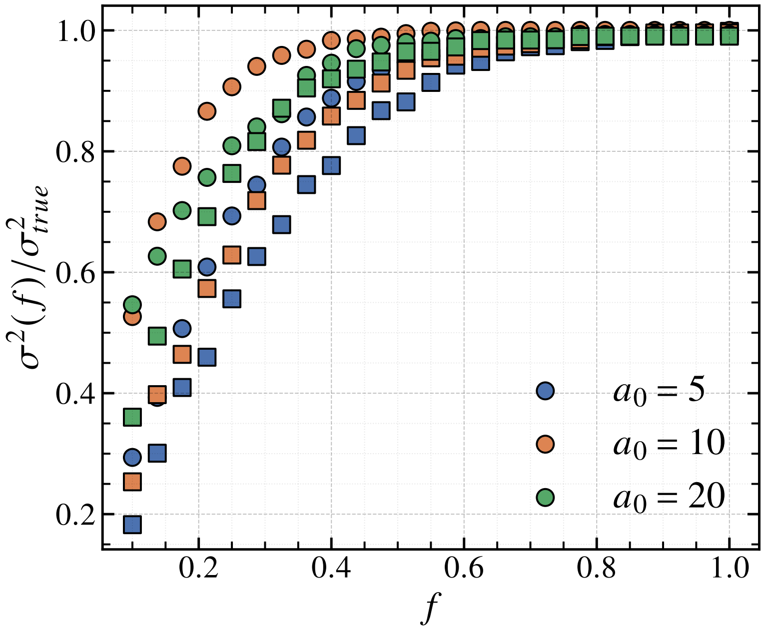

Figure 5.14: Estimation of the profile variances parallel (circles) and perpendicular (squares) to the laser polarisation for different truncation fractions, f, relative to the true variance determined from the entire distribution. Variances are calculated using the PTARMIGAN-generated profiles from Fig. 5.11 for each simulated intensity: $a_0 = 5$ (blue), $a_0 = 10$ (orange), and $a_0 = 20$ (green).

quantum effects are appreciable. From Fig. 5.10, the inference of intensity using Eq. (5.9) is expected to be less accurate here. However, since the parameters of LUXE are well-documented, it is possible to obtain a simulated parameterisation of the behaviour of $\sigma^2_\parallel$ and $\sigma^2_\perp$ which may improve the intensity retrieval. However, this approach will still suffer from the truncation effect in measuring the profile variances. In Fig. 5.15, the profile variances are plotted over a range of a_0 and fitted with a power law function of the form $ax^b + c$. The fitting parameters where found to have the values

$$\begin{cases} \sigma^2_\parallel &= ((1.1300 \pm 0.0002) \times 10^{-5}) a_0^{(2.23\pm0.01)} + ((1.1500 \pm 0.0003) \times 10^{-2}), \\ \sigma^2_\perp &= ((8.59 \pm 0.05) \times 10^{-3}) a_0^{(0.40\pm0.04)} + ((-1.91 \pm 0.08) \times 10^{-3}). \end{cases} \tag{5.20}$$

The predicted intensities using Eq. (5.20) and the variances taken from the FLUKA GBP simulations in Table 5.1 are compared with results calculated using the inference technique, Eq. (5.9) in Fig. 5.16b. In order to utilise the inference formula, the reciprocal moments of the electron initial and final gamma factors are needed; these are extracted from the spectra depicted in Fig. 5.16a. For a quantification of the uncertainty in the inference, by Eq. (5.10), the errors in

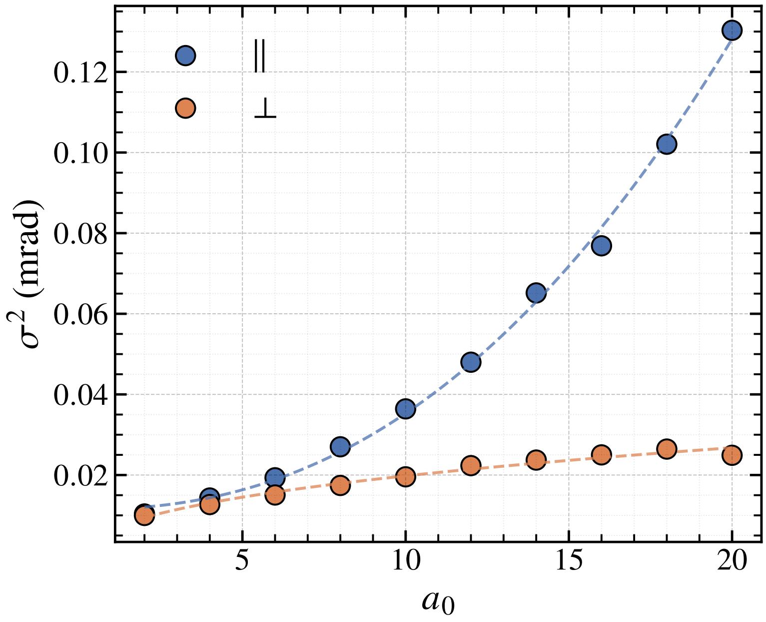

Figure 5.15: Variance of the transverse profile for projections parallel (blue) and perpendicular (orange) to the laser polarisation over a range of a_0 using LUXE simulation parameters. The fitted power laws (dashed lines) Eq. (5.20) are also depicted.

calculating the moments and the profile variances is required also. This is done using a standard result from statistics, invoking the "Law of the Unconscious Statistician",

$$\langle g(X)\rangle = \frac{1}{N}\sum_{i=1}^{N} w_i g(x_i), \quad \sigma_{\bar{g}}^2 \equiv \mathrm{Var}[\langle g(X)\rangle] = \frac{1}{N}\mathrm{Var}[g(X)], \quad \mathrm{Var}[g(X)] = \langle g^2(X)\rangle - \langle g(X)\rangle^2, \tag{5.21}$$

where the w_i are respective weights that sum to N. Essentially, this defines the error in the expectation value of some function, $g(x)$, calculated using a sample of size N, as estimated from the sample mean and variance. From this, the associated uncertainty is $\delta\langle g\rangle \equiv \sigma_{\bar{g}} = {}^{\delta g}/_{\sqrt{N}}$. Going farther, the error in the profile variance, assuming a mean of zero, is calculated following the definition

$$\sigma^2 = \frac{1}{N}\sum_{i=1}^{N} w_i x_i^2 \qquad \Rightarrow \qquad \delta(\sigma^2) = \frac{2\sigma\delta x}{N}, \tag{5.22}$$

where δx is the common uncertainty in measuring each x value. Furthermore, since ${}^{\delta(\sigma^2)}/_{\sigma^2} = 2{}^{\delta\sigma}/_{\sigma}$, the uncertainty in measuring the standard deviation is $\delta\sigma = {}^{\delta x}/_{N}$. These results can also be verified using the Central Limit Theorem.

In Fig. 5.12, the GBP profiles are measured using 400 bins within the angular range −0.82 mrad to 0.82 mrad, giving an uncertainty in the standard deviation of $\delta\sigma \sim 1\times10^{-5}$ mrad.

The final result of applying the inference formula, Eq. (5.9), along with the geometrical correction Eq. (5.16), is shown in Fig. 5.16b with the associated error. Despite the non-negligible quantum dynamics expected for the LUXE interactions, the inference formula still estimates the nominal intensity remarkably well, and within the prescribed uncertainty for a nominal $a_0 \lesssim 10$.

For the case of $a_0 = 20$, two effects limit the accuracy of the inference method. As discussed in Section 5.1.3, for high χ, the inference model becomes less accurate due to the increased quantum effects on the electron dynamics such as non-linear pair production. An additional effect, which also influences the calculation of a_0 from the empirical fitting, is the truncation of the photon profiles due to the size of the detector screen. Clearly, the error of $\sim 60\%$ will have a pronounced effect on using the empirical fitting to estimate a_0 due to its monotonic nature, resulting in it underestimating the nominal a_0 more than the inference method.

The error bars in Fig. 5.16b are calculated without including the truncation error, instead only representing the uncertainty from the inference method Eq. (5.10), and the uncertainty in the empirical fitting Eq. (5.20). At $a_0 = 10$, the uncertainty due to the 15% truncation error is smaller than the uncertainties in the determination of a_0, however, at $a_0 = 20$, the $\sim 60\%$ truncation error becomes the dominant source of error, increasing the depicted uncertainty by a factor of ~ 10. Hence, measuring as much of the angular profile within the $\sim {}^{2a_0}/_{\gamma}$ interval is crucial for accurate inference of the nominal a_0.

5.3 Conclusions

Electrons oscillating in a linearly polarised electromagnetic wave emit Compton radiation with an angular profile that is characteristic of both the electron's dynamics and the field configuration. By extending this theory to include radiation reaction, temporal envelopes and focusing effects of the spatial distribution of the field, it has been possible to develop a method to infer the a_0 of the background field using the size of the photon angular profile and the initial and final electron energies. This technique is analogous to one presented in [142], however the one detailed here utilises the number-weighted photon profile; this is more readily measured at high energies and fluxes than the energy-weighted profiles examined in [142].

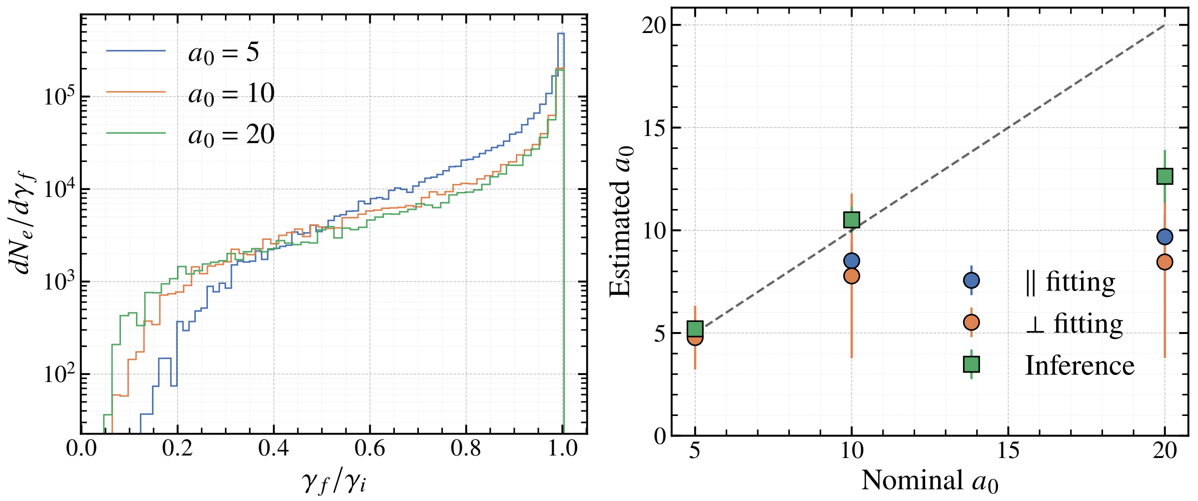

(a) **(b)**

Figure 5.16: (a) Final electron energy spectra after the LUXE electron-laser interaction for $a_0 = 5$ (blue), $a_0 = 10$ (green) and $a_0 = 20$ (red) in terms of the electron Lorentz gamma factor, with $\gamma_i m = 16.5\,\mathrm{GeV}$. (b) Estimation of the interaction intensity for each nominal a_0 using the power law fittings (circles) and the inference formula Eq. (5.9) (squares) with associated errors. Exact inference of the nominal a_0 is marked by a dashed, grey line as a guide for the eye.

Here, the rationale behind this technique has been presented, starting with a plane wave model before considering effects of a focused field, along with supporting simulations to demonstrate its accuracy for a range of nominal a_0 values and radiation reaction models. We demonstrated that within the a_0, χ parameter range that satisfies the undderlying assumptions, this inference technique is accurate to within 10%. Outside of this range, the inference still performs adequately with $\lesssim$ 20% accuracy. The decreased applicability in these regions of parameter space are attributed to the inaccuracy of the LCFA at low intensities and the presence of quantum effects such as pair production at $\chi > 1$.

By considering a particular implementation of a spatial profiler for the gamma ray beams that are to be produced within LUXE, we analysed the application of the inference method to this setup. By using start-to-end simulations of the LUXE geometry, the photon profile measured by the detector is generated for different nominal a_0; these spatial profiles are then extracted similarly to a true in situ approach. From this analysis, it was shown that for a_0 up to 10 (above the range envisioned for LUXE), the inference technique is able to estimate the nominal a_0 with good accuracy, despite a truncation in the measured profile due to the detector size. This was compared to an alternative approach mentioned in [21], using simulations to form an empirical formula for the profile size, which turned out to be more sensitive to the truncation error than the inference method.

Chapter 6

Improving Conditions for Observing Elastic Photon-Photon Processes

It was demonstrated in [79, 105] that the configuration proposed by [104], adapted to form a laser-plasma setup, has substantial potential for measuring both linear Breit-Wheeler and elastic photon-photon scattering events as discussed in Section 3.1. However, for both of these processes, particularly the much rarer elastic scattering, improvements are needed in order to obtain a statistically significant number of scattering events. From [79], the number of scattering events can be approximated as $N_s \approx N_\gamma n_x L_{\mathrm{eff}} \sigma$, where n_x is the x-ray density, L_{eff} is the effective length of the x-ray field, N_γ is the number of bremsstrahlung photons and σ is the scattering cross section. For the parameters used in [79]: $N_\gamma \sim 4 \times 10^7$, $n_x \sim 1.4 \times 10^{12}\,\mathrm{mm}^{-3}$, $L_{\mathrm{eff}} \sim 3\,\mathrm{mm}$ and $\sigma \sim 10^{-30}\mathrm{cm}^2$, the approximate number of scattering events per shot is $N_s \sim 1.7 \times 10^{-8}$. Operating at a repetition rate of 1 Hz, a continuous run time of 32 years is required to generate a single scattering event. This setup is evidently limited in achieving the statistics needed to place meaningful confidence limits on the photon-photon scattering cross section. With optimisations to the input beam configuration, it is possible to significantly improve the yield for both elastic scattering and linear pair production events by up to several orders of magnitude. In this chapter, an example configuration is presented on how to achieve this increase in yield, demonstrating the properties of the input beams that are required. This is compared to the original experimental results presented in [79, 105], indicating that similar setups can be used at current and future

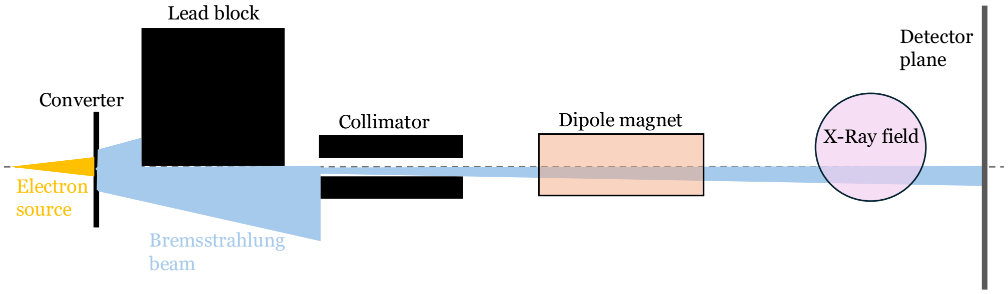

Figure 6.1: Simplified sketch of the simulation geometry to investigate photon-photon scattering events. Distances are not to scale and the electron and positron beams after the converter are not shown but are deflected out of the plane by the dipole magnet.

PW-class facilities to achieve the most stringent upper bound on the photon-photon scattering cross section to date.

6.1 Simulation of the Scattered Signal

6.1.1 Benchmarking Simulations

As a base case for comparison, the electron and x-ray parameters discussed in [105] are used as the input for a Geant4 simulation of the setup from the same experiment. A simplified sketch of the simulation geometry is shown in Fig. 6.1. The bremsstrahlung beam is generated by interaction of an LWFA electron source with a 1 mm bismuth converter, as detailed in Section 2.5. The average electron beam achieved during commissioning was broadband; modelled here as a Gaussian distribution with mean energy 430 MeV and an FWHM energy spread of 220 MeV. Additionally, the average charge in the electron beam is 22 pC and the average RMS divergence is 2.3 mrad. From these parameters, the electron beam forms the primary source within the Geant4 simulation by randomly sampling the Gaussian energy distribution. The momentum direction of the primary is generated from the angle pair (θ, ϕ) according to

$$\begin{cases} \beta_x &= \sin\theta\cos\phi, \\ \beta_y &= \sin\theta\sin\phi, \\ \beta_z &= \cos\theta, \end{cases} \tag{6.1}$$

where $\beta_i = {}^{p_i}/_{|\mathbf{p}|}$ is the corresponding direction cosine. The momentum polar angle, θ, is randomly sampled from a Gaussian centred on zero with standard deviation equal to the RMS divergence and the momentum azimuthal angle, ϕ, is uniformly sampled on the interval $[0, 2\pi)$. A simplistic model for the x-ray field is used for convenience here, since the corrections due to inclusion of spatial gradients in the photon density and a more accurate energy spectrum are expected to be much smaller than the order of magnitude estimate to be taken from these simulations. The photon density is implemented as a uniform distribution with $n_x = 1.4 \times 10^{12}\,\mathrm{mm}^{-3}$ within a cylindrical volume of length 3 mm [79]. The radius of the cylinder is not as important as the effective interaction length and the density, so it is chosen to be sufficiently large to contain the bremsstrahlung beam. Although the exact x-ray energy spectrum contains multiple peaks, the simplified model assumes a uniform spectrum within the interval 1.35 keV to 1.55 keV as from [105], there is no variation of the spectrum significantly greater than half an order of magnitude in this range. Following the setup of [105], the x-ray field is located 1.05 m after the converter target.

Using the photon processes extension to Geant4 (see Chapter 3 for details), the yield for photon scattering and linear pair production processes can be estimated. Since the cross sections for linear Breit-Wheeler and, particularly, photon-photon scattering are small, they are biased by a constant factor within the simulation in order to reduce the primary load required to simulate a statistically significant number of events. For all results shown within this chapter, this weighting is accounted for in post-processing.

Using 10^7 primary electrons and a weighting factor of 10^8 and 10^{14} for Breit-Wheeler and photon-photon scattering processes respectively, the results of the simulated photon-photon events are shown in Figs. 6.2 and 6.3. Specifically, Fig. 6.2 presents the yield of particles as

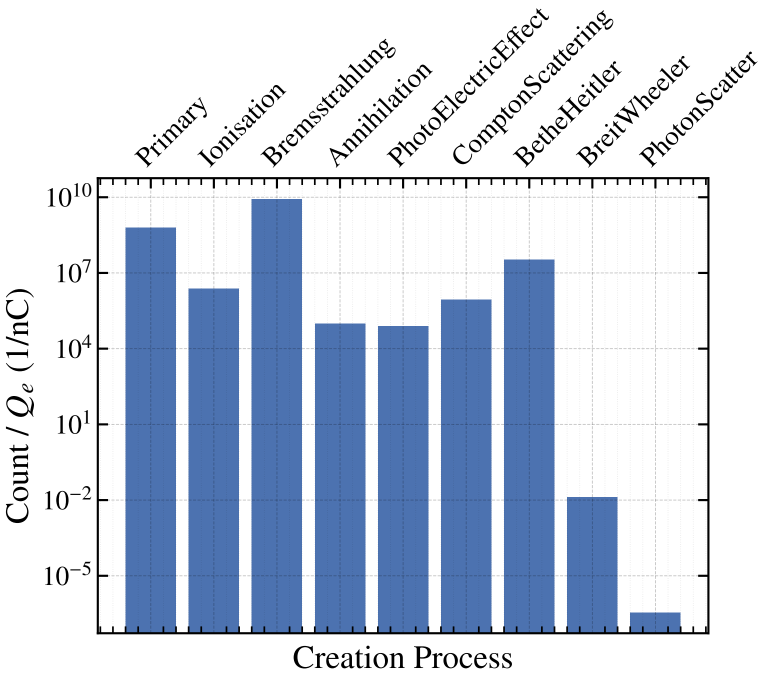

Figure 6.2: Number of simulated particles reaching a virtual detection plane according to their creation process. Count is normalised to the primary electron beam charge in nC. The "primary" creation process indicates that the particle is a simulation primary.

produced by a specific process, such as bremsstrahlung emission, pair production or photon scattering, per incident primary electron. The rarity of Breit-Wheeler and elastic scattering processes in comparison to the other electromagnetic processes is clearly evident. Dividing by half to account for double-counting (elastic scattering produces two secondary photons at each occurrence) and scaling by the 22 pC primary beam charge, the simulation predicts approximately 4×10^{-9} scattering events per shot, in agreement with the earlier estimate from $N_s \approx n_x L_{\text{eff}} N_\gamma \sigma$. Moreover, the scaling factor of 10^{14} for the photon-photon scattering cross section used here aligns with the findings of [79]; that such a biasing factor is required in order to measure scattering events with statistical significance. Similarly, the number of pair production events is estimated in the same way as 3×10^{-4} per shot, which is within the range presented in [105].

Figure 6.3 shows the phase space properties of the scattered photons (a-c) and the positrons generated by linear Breit-Wheeler production (d-f). Both the scattered photons and the generated positrons are similarly distributed in angle, exhibiting two peaks centred on $\delta = \pm 5$ mrad with a width of $\Delta\delta \approx 9$ mrad. The presence of the two peaks is due to the symmetry between the

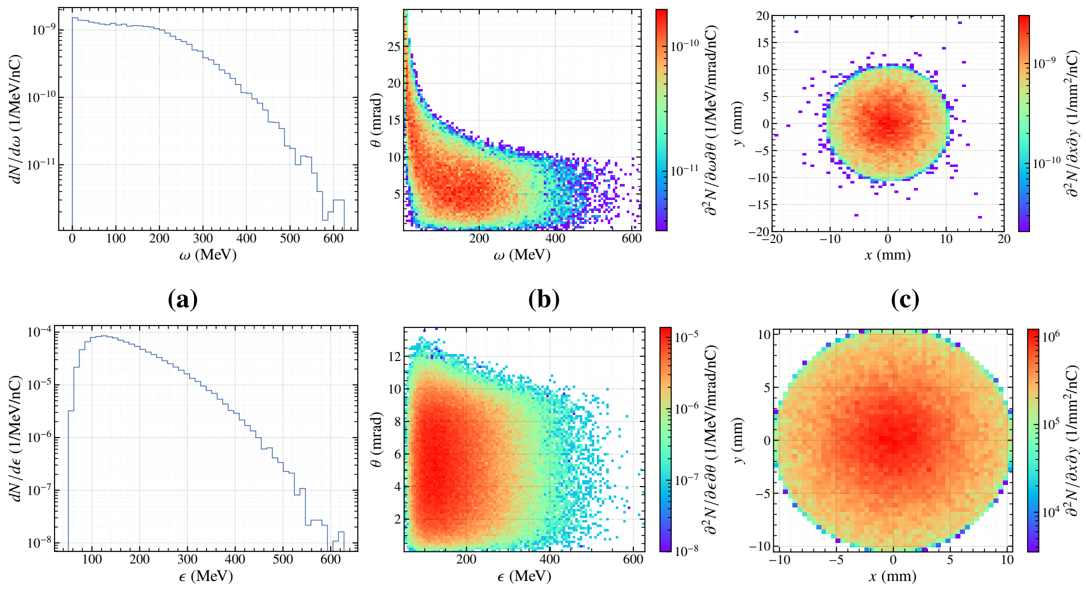

(a) **(b)** **(c)**

(d) **(e)** **(f)**

Figure 6.3: Simulated phase space information for the elastically scattered photons (top row) and Breit-Wheeler produced positrons (bottom row) using the benchmarking parameters. (a), (d) shows the energy spectra of the corresponding particles, (b), (e) the energy-angle double differential distribution and (c), (f) the spatial profile transverse to the bremsstrahlung beam direction.

outgoing particles in both the Breit-Wheeler production and photon-photon scattering processes. Additionally, the spatial profiles of both photons and positrons are almost identical, with the signal forming a disk of $^1/_{e^2}$ radius 10 mm. The angle-integrated energy spectra however are markedly different; the positrons exhibit a distinct peak energy at ≈130 MeV, whereas the photon spectrum is dominated by the scattering to lower energies.

6.1.2 Optimisation of the Photon Beams

Since the cross section is fixed and the effective length of the x-ray field will remain on the same order of magnitude, the most viable method of increasing the scattering yield is to increase the number of bremsstrahlung photons per shot, and also the x-ray density. The bremsstrahlung is directly tied to the efficiency in producing LWFA electrons within the plasma, and hence to the driver laser for this interaction. Similarly, the x-ray conversion efficiency and hence density are determined by the driving laser as well. Table 6.1 shows various facilities that have available multi-PW and kJ-class lasers. The facilities with dual-beam capabilities are the most appropriate for the laser-plasma platform to investigate photon-photon processes.

Facility	Laser	Power (PW)	Energy (kJ)	Duration (fs)	Wavelength (nm)	Rep. Rate (Hz)
Omega	NSF OPAL	25	0.5	20	1053	$^1/_{300}$
	OMEGA-EP	0.02	2.3	1×10^5	1053	$^1/_{300}$
CLF	VULCAN 20-20	20	0.4	20	530	$^1/_{300}$
	Long-pulse beam	2×10^{-4}	<2.6	$<1 \times 10^6$	1053	$^1/_{1800}$
SULF	SULF-10PW	10	0.3	30	800	$^1/_{60}$
ELI-BL	L4 (short-pulse)	10	1.5	150	1057	$^1/_{60}$
	L4 (long-pulse)	2×10^{-4}	1.2	$<5 \times 10^6$	1053	$^1/_{60}$
ELI-NP	10 PW-line	10	0.20	20	800	$^1/_{60}$
CoReLS	PW-line	4.2	0.083	19.4	800	0.1

Table 6.1: Table of example PW- and kJ-scale capable facilities with key laser parameters. Parameters are taken from [12, 146, 147, 148].

Bremsstrahlung Beam

It has been demonstrated that PW-scale lasers have been able to produce GeV-scale LWFA electron beams [149, 150], which will generate a large amount of bremsstrahlung photons as discussed in Section 2.5. As discussed in Section 2.5, the choice of converter target affects the quality of the generated bremsstrahlung beam, both in terms of energy content and angular spread. In order to maximise both the energy contained in the beam and the areal density, the target material and thickness need to be selected appropriately. If the target is too thin, an insufficient amount of photons is produced; too thick and the outgoing beam suffers multiple scattering, which increases the angular size and also reduces the mean energy. Figure 6.4 shows the results of a set of Geant4 simulations of a monoenergetic 5 GeV pencil-like electron beam interacting with a converter target of various materials and thicknesses. In order to determine the optimum material and thickness, the energy density of the outgoing beam is chosen as the figure of merit; this combines the need for a high energy content and fluence, similar to a previous optimisation study at lower electron energies [151]. The energy density is calculated by determining the total energy included within the $^1/_{e^2}$ radius of the beam. From Fig. 6.4, the optimum thickness for a converter target, regardless of material, is within the range of 5-15% of the radiation length. Additionally, the choice of converter is largely unimportant, offering at most a 20% increase in the energy density. In the Kettle et al. experiment [105], a 1 mm bismuth converter was used, which is consistent with a 15% X_0 thickness.

For the 10 PW beam-line at ELI-NP in Table 6.1, the anticipated properties of generated LWFA electrons were presented in detail in [152] and are used here as a case study for bremsstrahlung production. Using quasi-3D PIC simulations, [152] state that it is possible to produce a quasi-monoenergetic electron beam of central energy $E = 4.2\,\text{GeV}$ (15% FWHM spread), an RMS divergence $\delta_{\text{rms}} = 3\,\text{mrad}$ and a charge $Q_e \gtrsim 12\,\text{nC}$. A Geant4 simulation using such an electron beam as input and an iron converter target with a thickness of 4.4 mm (25% of X_0, where the optimum in Fig. 6.4 is seen), the resultant bremsstrahlung beam was scored as shown in Fig. 6.5.

In Fig. 6.5a, both the energy spectrum of the bremsstrahlung and the complementary cumulative spectrum (CCS) are shown together with a total number of photons of 1.7 ×

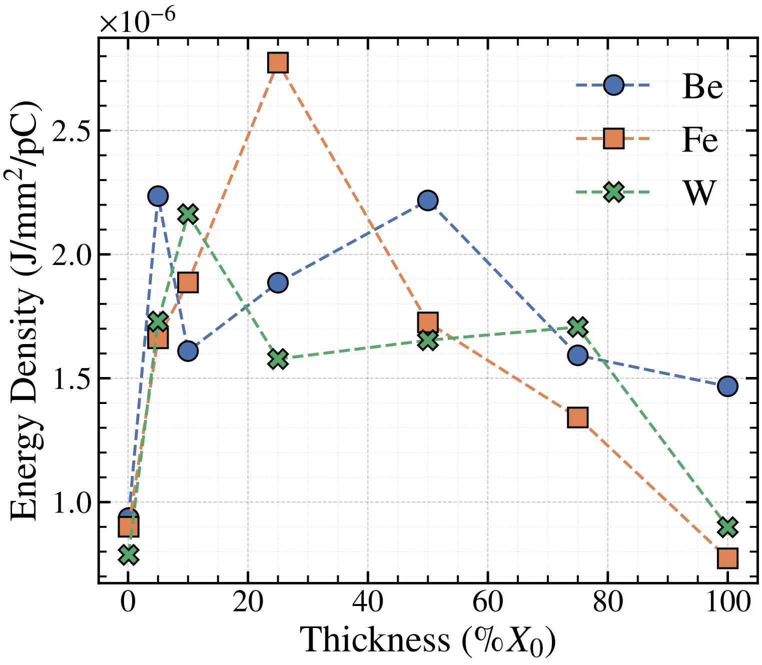

Figure 6.4: Simulated energy density of a bremsstrahlung beam produced by a monoenergetic 5 GeV electron beam impinging a target of various thicknesses and tungsten (blue, circle), iron (orange, square), and beryllium (green, cross) composition. Target thicknesses are given as a percentage of the material radiation length, X_0.

10^{11} nC^{-1}. From the CCS, approximately 10% of the photon beam has energy greater than 1 GeV, corresponding to $N_\gamma \approx 4 \times 10^{11}$, which is desirable for reaching a ZMF energy, $\sqrt{s} \gtrsim 1$ MeV where the photon-photon scattering cross section is maximised. Additionally, the divergence and size at a distance 1.05 m from the converter of the beam have also been shown as a function of energy. This was done by partitioning the phase space of the bremsstrahlung output into discrete energy bins, then determining the corresponding statistic for each bin. As can be seen from Figs. 6.5b and 6.5c, both the beam size and divergence are uniform across the energy spectrum, with some statistical fluctuations at the high energy end of the spectrum. Therefore, the mean value of these distributions can be taken as the representative dimensions of the beam, resulting in a bremsstrahlung beam of transverse $^1/_{e^2}$ radius 4.3 mm and RMS divergence 3.5 mrad. A half-block of lead shielding, as in [105], is set into the beam after the converter, reducing the beam to half-circle. This prevents the bremsstrahlung photons from interacting with the target used to generate the x-ray field, which would otherwise produce a significant amount of noise.

Since all energies are, approximately, equally contained within this beam size, a range of

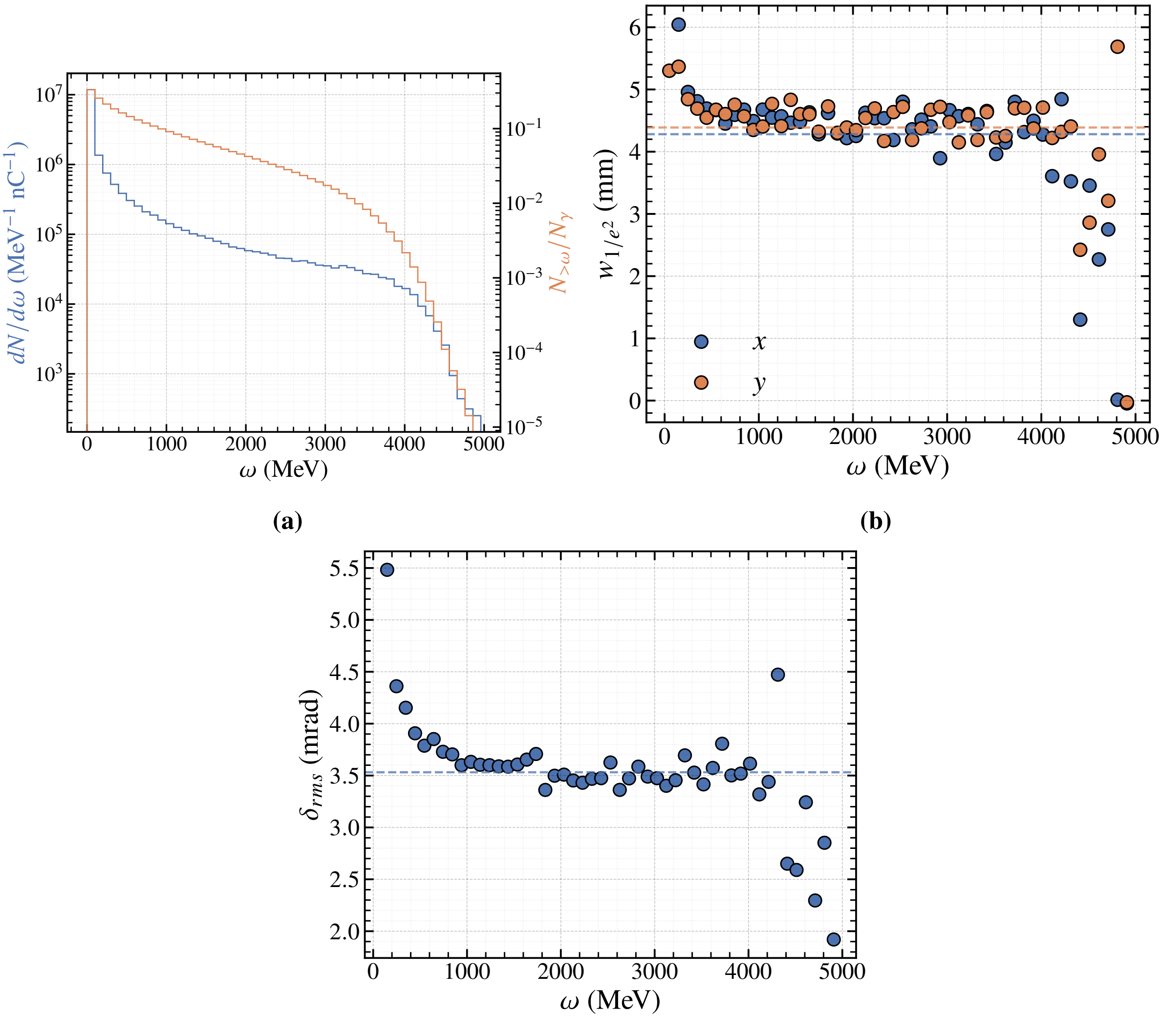

(a)

(b)

(c)

Figure 6.5: Properties of the bremsstrahlung beam generated using the ELI-NP electron beam incident on a 4.4 mm iron target. (a) shows the energy spectrum of the photons (blue) and the CCS (orange). (b) shows the $^1/_{e^2}$ size in x (blue) and y (orange) for each energy of the beam, at a distance of 1.05 m from the target. (c) shows the RMS angular divergence for the same energy divisions. For (b) and (c), the mean values of the quantities are represented by dashed horizontal lines.

ZMF energies will be possible upon collision with the x-ray field. Therefore, an effective $\sqrt{s}$ can be defined as

$$\sqrt{s}_{\mathrm{eff}} \equiv \langle\sqrt{s}\rangle = \int \mathrm{d}\omega_1\, f_1(\omega_1) \int \mathrm{d}\omega_2\, f_2(\omega_2) \int \mathrm{d}\theta\, \sqrt{2\omega_1\omega_2(1-\cos\theta)} \qquad (6.2)$$

where the $f_j(\omega_j)$ are the energy spectra of the bremsstrahlung ($j = 1$) and x-rays ($j = 2$), normalised to unit integral. A flat distribution is assumed for the x-ray spectrum, $f_2(\omega_2)$, between 1.3 keV and 1.5 keV; the angular distribution is limited by the extent of the x-ray field, which is assumed to be constant in the interval $\theta \in [\phi, \pi - \phi]$ where $\phi = \arctan {}^{1}/_{1.5} = 0.58\,\mathrm{rad}$, the effective ZMF energy using the spectrum shown in Fig. 6.5a is $\sqrt{s}_{\mathrm{eff}} = 1.7\,\mathrm{MeV}$.

X-Ray Field

The x-ray field affects the number of scattering events according, approximately, to the combination $n_x L_{\mathrm{eff}} = {}^{N_x}/_{AL_{\mathrm{eff}}} L_{\mathrm{eff}}$, where A is the transverse interaction area. Hence, the quantity to consider optimising is the areal density of the x-ray field, which is independent of the effective length. Since the transverse interaction area is determined primarily by the bremsstrahlung beam, the areal density can be optimised by increasing the produced x-ray yield. A comprehensive study is provided in [153] of the x-ray emission of irradiated foils which are particularly useful for extracting some estimates of scaling for the photon density with laser energy and duration.

The quantity of interest in [153] is the x-ray conversion efficiency, ξ_x, measured in photons per unit of incident laser energy; an additional normalisation to solid angle is given, however this amounts to a factor of 4π as emission is assumed to be isotropic. The number of emitted x-ray photons is then $\xi_x \mathcal{E}_L$, where $\mathcal{E}_L$ is the laser energy. For laser energies up to 40 J, with the range increased to 120 J in [154], [153] demonstrates a linear relationship between the conversion efficiency and the laser energy, and hence $\xi_x \mathcal{E}_L \propto \mathcal{E}_L^2$.

The laser pulse duration, τ_L, also has been found to influence the x-ray production. Generally, longer pulses generate a longer plasma which allows for more efficient coupling of the laser energy via inverse bremsstrahlung [154, 155]. This is shown in Fig. 6.6, where ξ_L is highest for a combination of both higher laser energy and longer duration pulses. For higher intensities, where $a_0 \gg 1$, plasma heating by inverse bremsstrahlung becomes less efficient due to the increase in

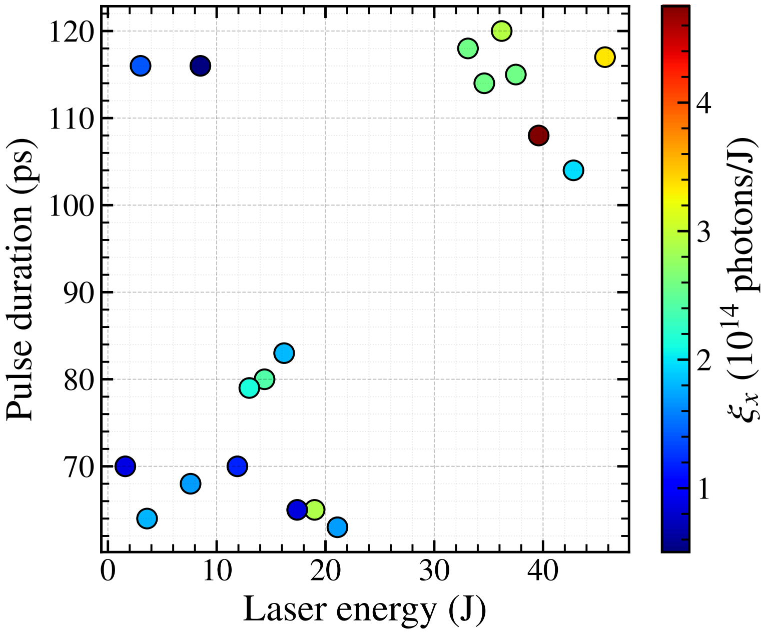

Figure 6.6: Conversion efficiency for producing M-L transition x-rays by irradiating palladium targets for different pulse durations and laser energies for a laser wavelength of 530 nm. Representation of data extracted from [153].

the relativistic mass of the oscillating electrons and occurrence of non-linear effects. Hence, if the laser energy is increased with a compensatory increase in the pulse duration to maintain a non-relativistic intensity ($\sim 10^{15}$W cm^{-2}), the scaling of the x-ray yield up to $\mathcal{E}_L \sim 1$ kJ can be assumed to be at most quadratic. Therefore, scaling from the 10 J to 1 kJ gives an order of magnitude estimate for a best-case achievable x-ray areal density as $n_x L_{\text{eff}} \sim 10^{16}$mm^{-2}.

6.1.3 Simulations using Enhanced Sources

Since the ELI-NP electron beam with an optimised converter target can produce a bremsstrahlung beam with $\sim 10^{11}$ photons of energy greater than 1 GeV, this results in a factor of 10^4 increase in N_γ compared to the original experiment in [105]. Similarly, assuming the best case scaling of the x-ray generation with laser energy, a factor of 10^4 in the combination $n_x L_{\text{eff}}$ could be achieved. Combining these, this gives a new number of scattering events 10^8 times higher than the benchmarking case, corresponding to 0.1 events per shot. With this substantial increase in the event rate, it would be possible to achieve a statistically significant data sample within a typical experimental time frame. In fact, if the x-ray source remains identical to that in [105] and only the electron source is upgraded, a factor of 10^4 increase in the scattering yield reduces the minimum required continuous run time at 0.02 Hz to see a single scattering event to approximately 60 days. While impractical for current facilities, this is an extremely encouraging advancement for future QED experiments as such electron sources from LWFA at multi-PW facilities are becoming more and more routine to produce.

These two cases are simulated as examples of the potential signal that could be generated with such electron and x-ray parameters. The electron beam discussed in Section 6.1.2 is used as the primary particle source in the simulations, with the x-ray field modelled similarly to the benchmarking case. The simplified implementation of a cylinder of radius 10 mm with the areal density, $n_x L_{\mathrm{eff}}$, scaled by the appropriate amount as in Section 6.1.2. This density is taken to be the average value within the effective interaction volume, 1 mm from the x-ray source, as for the benchmarking simulations. For the purposes of these simulations, the same interaction length of 3 mm as in the benchmarking simulations is used, assuming a similar rate of isotropic expansion for the x-ray field; only the photon density is then scaled by the stated factor.

The number of events are seen in Fig. 6.7, normalised to the incident electron charge. As predicted from the simplistic order-of-magnitude estimate, there is a factor of $10^5 \cdot 5 \times 10^2 \sim 10^8$ increase between the fully scaled case and the benchmark for the photon-photon scattering yield, with a $10 \cdot 5 \times 10^2 \approx 10^4$ increase in the electron-scaled case. Additionally, the Breit-Wheeler process benefits from a similar improvement as expected, with $\approx 10^3$ events per shot using the fully-scaled configuration.

Due to the higher maximum, and hence mean, energy of the bremsstrahlung source, the phase space distribution of the positrons and photons are consequently different to the benchmarking case. The energy distribution of both the Breit-Wheeler positrons and scattered photons retains the broadband bremsstrahlung-like shape up to ≈5 GeV. The angular distribution is also affected, with the cones of radiation centred on $\delta \approx \pm 2$ mrad with an asymmetric width of $\Delta\delta \approx 5$ mrad. This narrowing of the radiation cone is typical of QED scattering processes as it is an effect of the Lorentz contraction when transforming from the ZMF frame to the laboratory frame. The spatial distribution is also much more confined than the benchmarking case, with Figs. 6.3c and 6.3f showing a quasi-uniform distribution of the signal within the 10 mm radius circle. With the higher energy source, the signal is distributed more like a Gaussian within a disk of $^1/_{e^2}$

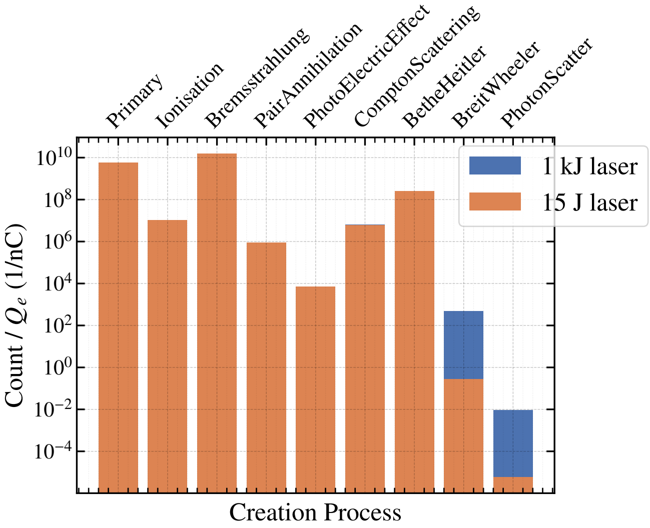

Figure 6.7: Number of simulated particles reaching a virtual detection plane according to their creation process using the ELI-NP electron beam source and: the x-ray field described in [105] (orange); and the best-case scaled x-ray field (blue). Count is normalised to the primary electron beam charge in nC. The "primary" creation process indicates that the particle is a simulation primary.

radius 5 mm.

6.2 Feasibility of Future Investigations

From the simulations detailed in the previous section, it is evident that with current PW-scale and higher power future facilities, there is a strong feasibility to measure the rare elastic photon-photon processes directly in experiment for the first time. While the discussion in Section 6.1 is rather general, assuming order-of-magnitude scalings for the producible x-ray fields and bremsstrahlung beams, they demonstrate that experimental run-times to observe these events could be reduced to the order of a minutes or hours if single-event observation is possible. If a particular facility with known configuration and parameters is chosen, a more precise modelling of the signal and background could be achieved, including hydrodynamic simulations of the x-ray generation and the achievable LWFA electron source.

The value of a few days for the required experimental run time to observe a single event is an absolute minimum for any particular configuration. Fluctuations in the background, as well as the capability of the selected detectors to resolve the signal, will generally increase the necessary run time in order to achieve sufficient statistics. Following the definition of the signal to noise

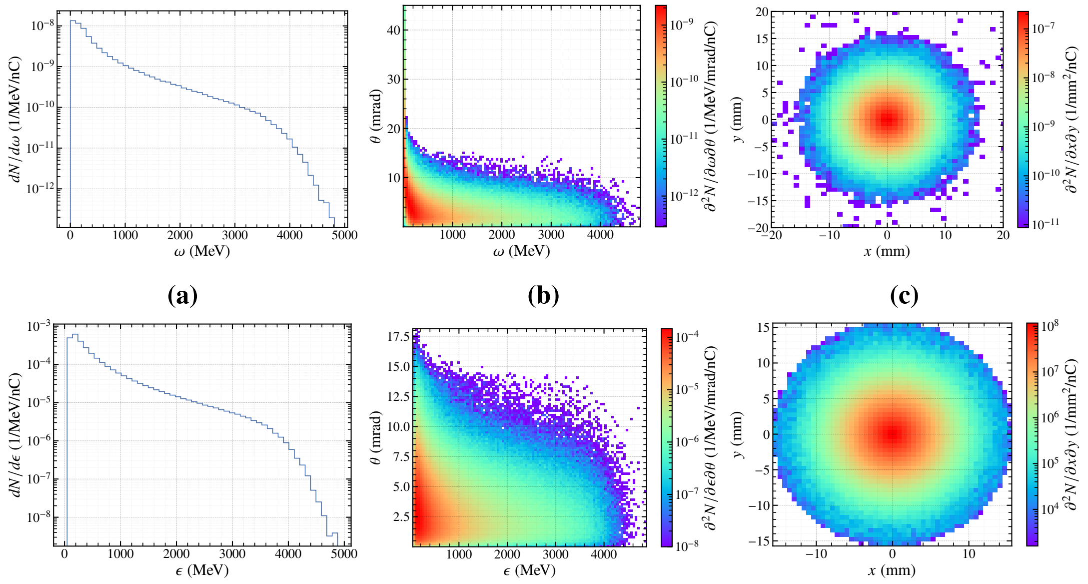

(a) **(b)** **(c)**

(d) **(e)** **(f)**

Figure 6.8: Simulated phase space information for the elastically scattered photons (top row) and Breit-Wheeler produced positrons (bottom row) using the ELI-NP electron beam parameters and the x-ray field described in [105]. (a), (d) shows the energy spectra of the corresponding particles, (b), (e) the energy-angle double differential distribution and (c), (f) the spatial profile transverse to the bremsstrahlung beam direction.

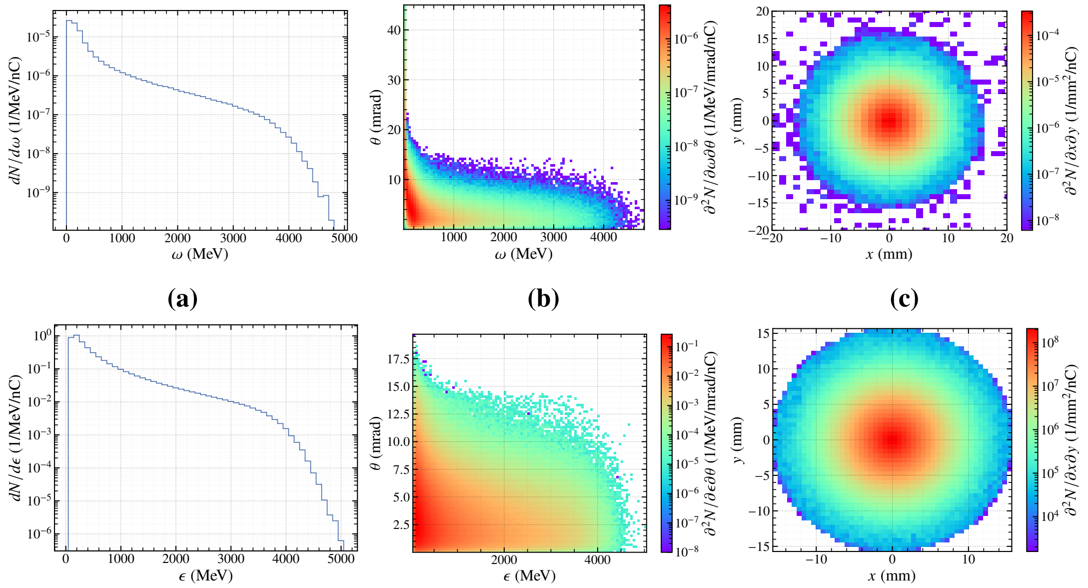

(a) **(b)** **(c)**

(d) **(e)** **(f)**

Figure 6.9: Simulated phase space information for the elastically scattered photons (top row) and Breit-Wheeler produced positrons (bottom row) using the ELI-NP electron beam parameters and best-case scaling for the x-ray field. (a), (d) shows the energy spectra of the corresponding particles, (b), (e) the energy-angle double differential distribution and (c), (f) the spatial profile transverse to the bremsstrahlung beam direction.

in [99] as the mean-to-variance ratio $\mathrm{SNR}_\sigma = {}^{\mu}/_{\sigma}$, an estimate of number of shots required to measure the signal with statistical significance can be made. μ is the mean value for the signal over the multiple shots and σ^2 is the signal variance, which is related to the uncertainty due to the detector and the background as $\sigma^2 = \sigma_{\mathrm{det}}^2 + \sigma_{\mathrm{bkg}}^2$. Since $N_{\mathrm{det}} = N_{\mathrm{sig}} + N_{\mathrm{bkg}}$, $\sigma_{\mathrm{det}}^2 = \sigma_{\mathrm{sig}}^2 + \sigma_{\mathrm{bkg}}^2$ as the background and signal are independent. Therefore, the total variance in $N_{\mathrm{sig}} = N_{\mathrm{det}} - N_{\mathrm{bkg}}$ is $\sigma^2 = \sigma_{\mathrm{sig}}^2 + 2\sigma_{\mathrm{bkg}}^2$. The background variance, σ_{bkg}^2, requires full-scale simulations in order to be estimated appropriately, however the signal variance, σ_{sig}^2, can be estimated using the results of the simulations from the previous section. For the following, the ideal case of a constant, well-defined background is assumed such that $\sigma_{\mathrm{bkg}}^2 = 0$.

If a simple counting detector is used to observe the elastic scattering or linear Breit-Wheeler signal (either positrons or electrons), the observed signal obeys Poissonian statistics with a variance $\sigma_{\mathrm{sig}}^2 = N_{\mathrm{sig}}$; if the detector has an efficiency, η, then $N_{\mathrm{sig}} \longrightarrow \eta N_{\mathrm{sig}}$. In this case, the mean-to-variance SNR takes the form $\mathrm{SNR}_\sigma = \sqrt{\eta N_{\mathrm{sig}}}$. Using the values from Fig. 6.7, with the ELI-NP electron source and scaled laser/x-ray density parameters, the observed signal particles is 2900 for Breit-Wheeler positrons and 0.1 for elastically scattered photons. Hence, for a perfectly efficient detector, this results in an SNR_σ of 53.9 and 0.32. For a detector such as the GBP discussed in Chapter 5, the response of the detector is proportional to the photon flux incident on it, and so could be used to infer the number of scattering events by measuring the photon beam with and without the x-ray field present. [145] estimate an efficiency $\eta \approx 0.14$, resulting in $\mathrm{SNR}_\sigma \approx 0.12$.

Using a detector that provides resolution in energy, such as the GRS from Chapter 4, the signal-to-noise ratio becomes a function of energy. For an energy interval of width ΔE, the number of particles contained in this interval is then $\frac{\mathrm{d}N}{\mathrm{d}E}\Delta E$; again assuming a Poisson distribution for the content of each interval, the signal-to-noise is analogously given by

$$\mathrm{SNR}_\sigma(E) = \sqrt{\eta(E)\frac{\mathrm{d}N}{\mathrm{d}E}\Delta E} \tag{6.3}$$

For the GRS, the efficiency is determined by several factors: first is the conversion of the photon beam to electron-positron pairs, which determines how much of the photon spectrum is sampled and "made known" to the detector and reconstruction algorithm. After conversion,

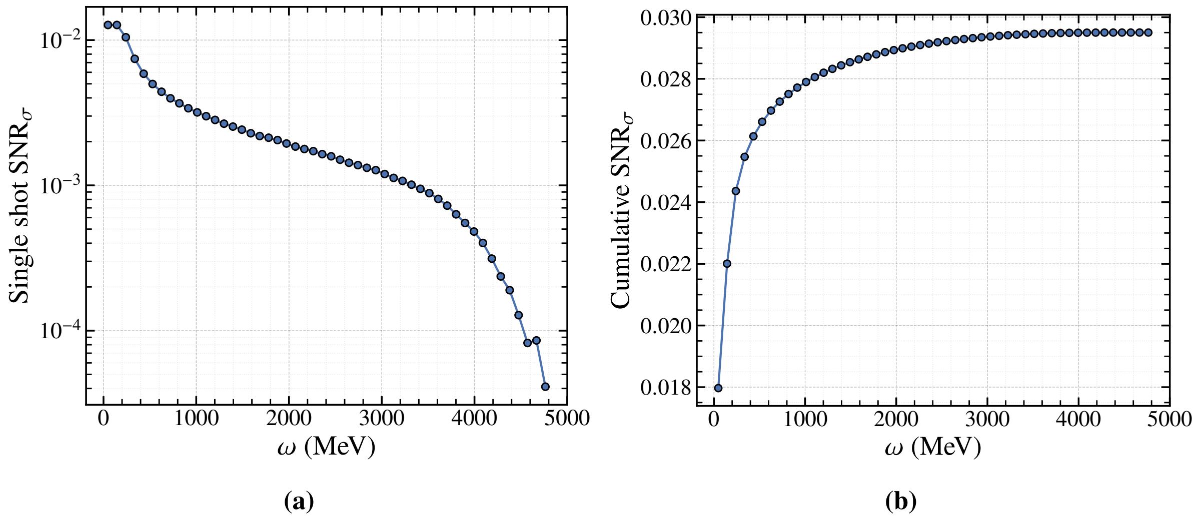

Figure 6.10: The (a) SNR$_\sigma$ for a single shot using the GRS and (b) the cumulative SNR$_\sigma$, calculated using Eq. (6.3), using the detector efficiency described in the text and the energy spectrum of the elastically scattered photons as shown in Fig. 6.9a.

the dispersion of the electron-positron pairs, and their collection, in the magnetic spectrometer component also affects the performance of the reconstruction as a better resolved spectrum will produce a more faithful reconstruction. Since these latter points are determined by the precise configuration of the GRS and can, in principle, be optimised to increase efficiency as much as possible, the conversion of the photon beam is the limiting factor. From Eq. (2.43), the conversion efficiency, defined to be the ratio of the number of converted photons to those incident, is $\eta(\omega) = 1 - \mathrm{e}^{-\mu(\omega)t}$, where $\mu = {}^{N_A X_0 \sigma}/_{A}$ is the attenuation factor and t is the converter thickness in units of the material radiation length. Using the corrected Bethe-Heitler cross section model employed by GEANT4, and the energy spectrum of the scattered photons from Fig. 6.9a, the SNR$_\sigma$ from Eq. (6.3) is shown in Fig. 6.10 for a tungsten converter target of nominal thickness $t = 1\%$ ($X_0 = 6.76\,\mathrm{g\,cm^{-2}}$). The SNR$_\sigma$ has a very similar shape to the scattered photon spectrum, due to the weak logarithmic dependence of the Bethe-Heitler cross section on photon energy up to $\omega \sim 1$ GeV, where the cross section becomes approximately constant.

It is also productive to consider what energies in the bremsstrahlung source are most likely to be scattered in the x-ray field. This can be done by weighting the incident bremsstrahlung spectrum in Fig. 6.5 with the photon-photon scattering cross section Fig. 6.11a and averaging

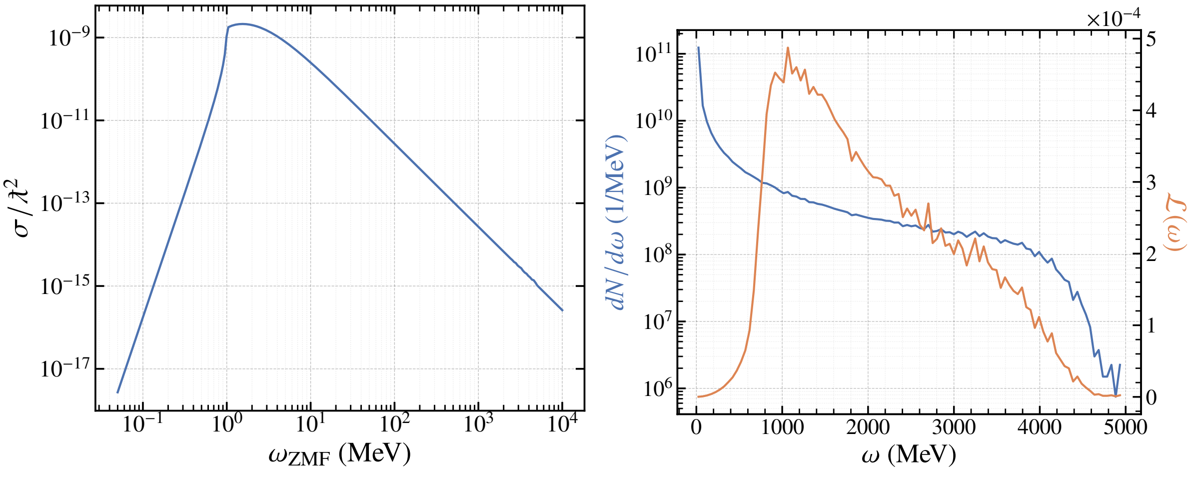

(a) **(b)**

Figure 6.11: (a) The photon scattering cross section, in units of the (reduced) electron Compton wavelength, as a function of the ZMF photon energy, (b) the normalised scattering likelihood (orange) for the bremsstrahlung spectrum in Fig. 6.5a (shown for reference in blue), calculated using Eq. (6.4).

over x-ray photon energies and collision angles:

$$\mathcal{L}(\omega) \propto \int \mathrm{d}E_x\, f(E_x) \int \mathrm{d}\theta\, \frac{\mathrm{d}N_\gamma}{\mathrm{d}\omega} \sigma[s(\omega, E_x, \theta)]. \tag{6.4}$$

The normalisation of this weighted spectrum, or scattering likelihood, is chosen such that $\int \mathcal{L}(\omega)\ \mathrm{d}\omega = 1$. $f(E_x)$ is x-ray energy spectrum, which is assumed here to be uniform in 1.3 keV to 1.5 keV. The resulting likelihood is depicted in Fig. 6.11b, which the bremsstrahlung spectrum for reference as well. Due to the peak in the scattering cross section at a ZMF energy $\omega_{\text{ZMF}} = \sqrt{s}/2 \approx 1\,\text{MeV}$, there is a distinct peak in the scattering likelihood; for the given bremsstrahlung spectrum, this corresponds to an approximate range of 0.8 GeV to 1.6 GeV. Therefore, photons within this energy range in the bremsstrahlung source are more likely to undergo elastic scattering in the x-ray field. Since the scattered photons occupy the interval $[0, \omega_\gamma + \omega_x] \simeq [0, \omega_\gamma]$, where ω_γ is the energy of the bremsstrahlung photon and ω_x the x-ray photon energy, the signal interval could be focused on photon energies up to ≈1.6 GeV. Additionally, since the photons are scattered symmetrically into this interval, the range could be further reduced to 0.8 GeV to 1.6 GeV. This will half the number of signal photons, however the background count will also be further reduced in this region, in principle improving the SNR_σ further.

The above values of the SNR_σ are calculated using the statistics of a single shot. By repeating measurements over k shots, the mean signal is $\langle N_\mathrm{sig}\rangle \approx {}^{kN_\mathrm{sig}}/_{k} = N_\mathrm{sig}$, with the signal variance determined by the standard error $\langle\sigma^2_\mathrm{sig}\rangle = {}^{\sigma^2_\mathrm{sig}}/_{k}$; this results in an amended signal-to-noise of $\mathrm{SNR}^{(k)}_\sigma = \sqrt{k\cdot\eta N_\mathrm{sig}}$. Defining a $\mathrm{SNR}^{(k)}_\sigma \gtrsim 10$ as sufficient to statistically resolve signal, only one shot is required to observe the Breit-Wheeler positron signal assuming the detector has an efficiency greater than 0.03. If the elastically scattered photons are measured using the GBP, as an example, approximately 6900 shots must be taken to meet this requirement on the signal-to-noise. For the GRS, using Fig. 6.10, the cumulative signal-to-noise is calculated by the quadrature sum of each $\mathrm{SNR}_\sigma(\omega)$; the total integrated SNR_σ over all photon energies is 3.0×10^{-2}. The number of shots required to achieve a total integrated signal-to-noise greater than 10 is then $\sim 1.5\times10^5$; at a repetition rate of a shot per minute, this is equivalent to an experimental run time of approximately 63 weeks, assuming operation at 8 hours per day, 5 days a week.

The above estimates for the signal-to-noise have assumed that the background is constant and well-known with $\sigma^2_\mathrm{bkg} = 0$. We now consider the allowed level of fluctuations in the background which minimally affect the signal-to-noise. Including the background in the calculation, $\sigma^2 = \sigma^2_\mathrm{sig} + 2\sigma^2_\mathrm{bkg}$, and so defining $\mathrm{SNR}_\mathrm{true}$ as the true signal-to-noise with the background fluctuations included and $\mathrm{SNR}_\mathrm{opt}$ as the optimum considered previously with $\sigma_\mathrm{bkg} = 0$, their ratio is given by

$$\varepsilon \equiv \frac{\mathrm{SNR}_\mathrm{true}}{\mathrm{SNR}_\mathrm{opt}} = \left[1 + 2\frac{\sigma^2_\mathrm{bkg}}{\sigma^2_\mathrm{sig}}\right]^{-1/2}. \tag{6.5}$$

Hence, for a given reduction in the signal-to-noise, $0 < \varepsilon \leq 1$, the allowed variance in the background is $\sigma^2_\mathrm{bkg} = {}^1/_2\cdot\left(\varepsilon^{-2} - 1\right)\sigma^2_\mathrm{sig}$. This holds for both the signal shot variance and for the average over k shots. As an example, consider an experimental campaign that has one week of total run time. With a repetition rate of one shot per minute, the signal is then accumulated over $\approx 10^4$ shots. Using the GBP with $\eta = 0.14$, the variation in the signal is $\sigma^2_\mathrm{sig} = {}^{\eta N_\mathrm{sig}}/_{k} \approx 1.4\times10^{-6}$; this results in an optimal signal-to-noise of $\mathrm{SNR}_\mathrm{opt} \approx 12$. If the true signal-to-noise, accounting for the non-constant background, is to be at worst a factor of ten smaller than the optimal, i.e. $\varepsilon = {}^1/_{10}$, the background variance can then be at most $\sigma^2_\mathrm{bkg} \approx 7\times10^{-5}$ over the 10^4 shots. For a single shot, this corresponds to a background variance of 0.7. Using the same value of ε, the allowed variation in the positron background to ensure an $\mathrm{SNR}_\sigma^{(k)} \gtrsim 10$ over 10^4 shots when observing Breit-Wheeler production is $\sigma_{\mathrm{bkg}} \sim 0.27$, following the same calculation as above; $\sigma_{\mathrm{bkg}} \sim 2700$ is the corresponding single-shot variation in the positron background.

Even if the required number of shots or the consistency of the background cannot be reached to obtain an $\mathrm{SNR}_\sigma \gtrsim 10$, it is still possible to place a constraint on the magnitude of the cross section. Since $N_{\mathrm{sig}} \propto \sigma$, then if the cross section is scaled by some bias factor, λ_B, then $\sigma \longrightarrow \lambda_B \sigma$ and so $\mathrm{SNR}_\sigma \longrightarrow \sqrt{\lambda_B}\mathrm{SNR}_\sigma$. Then, in order to reach the requirement for the signal-to-noise, the cross section enhancement needs to be

$$\lambda_B \gtrsim \left(\frac{10}{\mathrm{SNR}_\sigma}\right)^2. \tag{6.6}$$

If $\mathrm{SNR}_\sigma \geq 10$, then clearly the cross section does not need biased. To connect the value of λ_B to an upper bound on the cross section, consider the following: if the true cross section were larger than $\lambda_B \sigma$, then the signal-to-noise would be greater than 10 and signal could be resolved. Hence, $\lambda_B \sigma$ represents the largest possible value the cross section could have that is consistent with not observing signal in a statistically significant manner.

Figure 6.12 shows the bounding biasing factor as a function of the number of shots taken, and for different levels of background fluctuation. In Fig. 6.12a, the single-shot SNR_σ is taken as 0.12, accounting for the efficiency of the GBP. Similarly in Fig. 6.12b, the quoted single-shot signal-to-noise value is taken as the integrated value up to 1.6 GeV in Fig. 6.10. As is expected, increasing the number of shots allows for a tighter constraint to be placed on the scattering cross section. Assuming a constant background, even a single shot is sufficient to bound the scattering cross section to within a factor of $\sim 10^4$ using the GBP; this is seven orders of magnitude smaller than the current best bound in [79]. Even with background fluctuations (σ_{bkg}^2) that are 10^6 times greater than the signal variance, it is still possible to constrain the cross section to the same level as in [79] with a single shot. The performance of the GRS is similar, however the tightness of the constraint is reduced due to the comparatively lower efficiency of the spectrometer than the GBP.

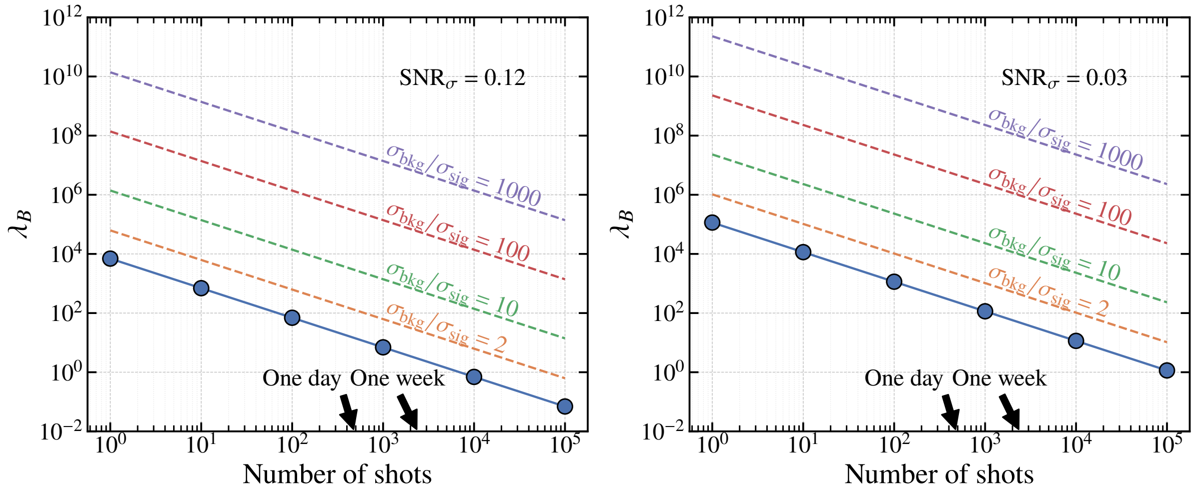

(a) **(b)**

Figure 6.12: Cross section scaling factor that would give an SNR$_\sigma$ = 10 for (a) the GBP and (b) the GRS, as in Eq. (6.6), assuming a constant background (blue, circles). The values for the true single-shot SNR$_\sigma$ are shown inset for each. Different amounts of background fluctuation are shown in coloured, dashed lines as $^{\sigma_{\rm bkg}}/_{\sigma_{\rm sig}}$: 2 (orange), 10 (green), 100 (red), and 1000 (purple). The number of shots equivalent to one day and one week of operation are also marked; assuming a rate of one shot per minute and 8 hours × 5 days as a standard working week.

6.3 Conclusions

The measurement of rare processes such as linear Breit-Wheeler pair production and elastic photon-photon scattering present a large challenge, even with modern technology and experimental means. Here, a configuration detailed and implemented in [104, 105] was considered, using typical electron beam parameters that could be readily obtained at current and next-generation PW-scale facilities, such as ELI-NP or NSF OPAL. Additionally, physical arguments were given to support the use of a kJ-class laser to generate a higher density x-ray scattering field than that achieved in [79, 105]. By using the high power laser to produce a high-yield, high energy bremsstrahlung beam via LWFA electrons impinging a solid target, it has been demonstrated using simulations that it is possible to increase the rate of these rare processes by several orders of magnitude. With this configuration, it is possible to produce $\sim 10^3$ Breit-Wheeler positrons per shot and a single elastic photon-photon scattering event within $\sim$ 10 shots. Under the assumption of a constant, well-defined background, it is possible to achieve a signal-to-noise ratio (defined as in terms of the mean-to-variance dispersion index) of $\sim$ 50 for the Breit-Wheeler positron signal and $\sim$ 0.3 for the scattered photon signal, assuming perfect detector efficiency. In order to achieve an $\mathrm{SNR}_\sigma \gtrsim 10$, $\sim 10^2 - 10^3$ shots are required for analysis of the photon signal; a signal shot is sufficient for the positron signal. These values represent an absolutely efficient configuration with constant background; if the background also fluctuates on a shot-to-shot basis, this increases the number of required shots to achieve the same signal-to-noise level. This constraint on the background fluctuations is rather strict, with a simple estimate indicating that the background variance must be $\sigma^2_{\mathrm{bkg}} \lesssim 1.0$ per shot, in order for the signal-to-noise to be within a factor of ten of its optimal value. Although this may preclude a direct observation of elastic photon-photon scattering, it could still be used to constrain the cross section within the smallest bound to date, four orders of magnitude smaller than [79]. Even with significant fluctuations, it is still possible to constrain the cross section within a single shot to at least the same magnitude as [79]. By accumulating data over many shots, the upper limit on the cross section can be greatly reduced.

With a specific choice of facility, and precise knowledge of the laser parameters, it is possible to perform more detailed simulations, including more accurate modelling of the x-ray scattering fields to account for spatial gradients and distribution. For instance, from Table 6.1, the most viable facilities that currently exist are ELI-BL and ELI-NP, where it is possible to have both a ~ 10 PW and ~ 1 kJ dual-beam configuration. The NSF OPAL facility at University of Rochester, USA is currently under development, aiming to provide a dual-25 PW beam as well.

Additionally, it is possible to develop an experimental setup which can further decrease the background by careful choice of detector systems, configuration and shielding; this knowledge is also required to more precisely simulate the background levels and its shot-to-shot fluctuations. The configuration presented in [104, 105] with a source typical of multi-PW facilities is well-suited to investigating two-photon or linear Breit-Wheeler pair production, with a large signal-to-noise ratio per shot. In an extended campaign over many shots, while observing Breit-Wheeler production, measurements of the resultant photons allows for investigation of the elastic photon-photon scattering process simultaneously. Although the signal is much smaller in yield than the Breit-Wheeler positrons, inferences on the observations can be made to bound the scattering cross section tighter than the current best [79]. Hence, the simplified investigation performed here demonstrates that experimental observation of elastic photon-photon processes is becoming increasingly more feasible with next-generation facilities.

Chapter 7

Outlook and Future Work

7.1 Improvements to the GRS Reconstruction Algorithm

The deconvolution algorithm presented in Section 4.1 was the second iteration of a reconstruction method designed to retrieve the photon spectrum from the Bethe-Heitler produced electron/positron spectrum. The first version of this algorithm was based on a back-substitution approach, mathematically equivalent to matrix inversion. While this was demonstrated in [25] to reconstruct the photon spectrum and edge-like features with the required accuracy for Compton-scattered sources, an analysis of the error propagation within the method revealed that the error would exponentially at each step; a problem that is well-known to occur for ill-conditioned problems. This lead to the current iteration of the deconvolution algorithm, which utilises a statistically-motivated Bayesian approach to the reconstruction. As such, error quantification is better defined and mitigates the exponential explosion the back-substitution approach suffered.

It is envisioned that the algorithm could be further improved, by combining the Bayesian nature of the method with machine learning (ML) techniques. Within recent years, ML techniques have grown in popularity for data reconstruction and retrieval problems due to their "black box" approach; once trained, they can operate on data with minimal supervision [156, 157, 158]. ML has already been successfully utilised in the context of SFQED experiments, for example, inferring collision parameters in a radiation reaction experiment from electron spectra [159]. In fact, an ML approach has already been discussed for a pair spectrometer at FACET-II, SLAC [160], which is similar in operation the one described here and in [25, 26]. By upgrading the current deconvolution algorithm to include such ML techniques, it could be possible to have a live, self-learning diagnostic within experiments that has improved robustness to shot-to-shot fluctuations.

7.2 Further Developments to the GBP

The gamma beam profiler (GBP) is a sapphire-strip type detector, capable of measuring the spatial profile of high-energy, high-flux photons in two orthogonal directions. Measurements from such a detector are designed to be complementary to the intensity inference method detailed in Chapter 5, extracting the profile size of a Compton-scattered photon beam to estimate the a_0 at the interaction of an electron beam with an intense laser pulse.

The theory developed in Section 5.1 made use of results calculated within the LCFA framework, particularly the photon emission rate. One limitation of the LCFA is that it is only valid for $a_0 \gg 1$, and for $a_0 \sim \mathcal{O}(1)$, effects such as interference are not included. The LMA framework circumvents this problem, and has been shown to accurately produce spectral effects which are present in full QED calculations that the LCFA is unable to capture. This improvement in modelling is important for $a_0 \sim \mathcal{O}(1)$, tending to the LCFA results as a_0 becomes large. However, results obtained using the LMA typically have intractable or even non-analytical forms, meaning it is difficult to directly integrate the LMA into existing theory without numerical or first-principles approaches.

For low $a_0 \lesssim 1$, the LMA predicts that the emission profile of Compton-scattered photons produced by electrons in a linearly polarised background has the characteristic shape of dipole radiation - with emission parallel to the polarisation of the field suppressed compared to the orthogonal axis; this is the reverse behaviour seen at large a_0 in Chapter 5. Clearly, the inference method cannot be used in such a regime as the combination $\sigma_{\parallel}^2 - \sigma_{\perp}^2$ will be negative, resulting in a non-physical, complex-valued inferred intensity. Hence, there is the challenge of including LMA effects into the inference technique, so that it can also be used in the $a_0 \lesssim 1$ regime.

Even without the LMA corrections, the intensity inference technique and the GBP have great potential in SFQED experiments. This detector has been proposed to be used in an upcoming experiment at ELI-BP, Czechia to measure photons produced in non-linear QED processes, with one objective to observe the transition between LMA and LCFA models. As the inference technique functions under the same assumptions as the LCFA, deviations of the inferred intensity relative to the nominal value could point to inaccuracy of the LCFA at low a_0. Additionally, further experimental testing of the detector performance, particularly its response to a photon source, is also envisioned following the results [145], which utilised an electron beam at CLEAR, CERN to characterise the charge collection efficiency of the detector over periods of irradiation.

7.3 Next-Generation Facilities for Elastic Two-Photon Processes

Direct observation of two-photon processes such as linear Breit-Wheeler pair production and elastic photon-photon scattering present an outstanding challenge for experimental physics as outlined in Section 2.4. A recent experiment [79, 105] used an experimental configuration proposed in [104], involving the interaction of a high-energy bremsstrahlung beam with a dense x-ray field, to give the tightest bound on the photon-photon scattering cross section to date. Chapter 6 quantifies the potential gain the same configuration can produce using a high-energy LWFA electron source typical of a multi-PW facility such as ELI-NP, Romania [152], as well as the increased x-ray density possible using exploding foils.

At the University of Rochester, the NSF OPAL facility is currently under development to provide dual 25 PW beam capability, delivering 500 J in 20 fs [161]. This facility aims to study physics within intense electromagnetic fields, such as SFQED and laser-driven nuclear physics. With such laser parameters, it will be possible to access regions of (a_0, χ) parameter space that have never been reached before, surpassing even LUXE and E-320, potentially even reaching the Ritus-Narozhny limit [147]. Another proposed facility that is under construction is the Station of Extreme Light (SEL), Shanghai, China which aims to deliver beams up to 100 PW [162]. As evidenced in Section 6.1, frontier facilities such as these are prime candidates for exploring the rare two-photon processes, as well as strong-field QED in the high χ regime. The increased intensities that are possible will increased the accelerated electron yield from a LWFA source, increasing the expected yield above that quoted in Section 6.1.

The generation of the x-ray field is also a point of further development. Qualitatively from the arguments in Section 6.1.2, the increased laser energy and stretching of the pulse duration can greatly enhance the achievable density using an exploding foil source. However, as $\lambda \sim 1$ µm for both NSF OPAL and SEL, this will require frequency doubling to attain the efficient x-ray conversion discussed in [153]. Recent results show that $\sim 60 - 80\%$ of the laser energy can be maintained upon 2ω conversion [163, 164]. In [104], hohlraums were proposed as an x-ray source however their use presented an additional challenge in laser stability and timing for producing a uniform, high density field.

Other experimental configurations involving the direct interaction of two and three light beams have also been analysed on a theoretical basis [85, 86] for light-by-light scattering, as well as using a Compton-produced photon source [103]. While this offers a cleaner environment to study two-photon processes, without the presence of substantial background as in the bremsstrahlung/x-ray configuration, synchronising the spatiotemporal overlap of the multiple beams presents a new challenge. Additionally, due to potential imperfections in the vacuum at the interaction point, the intense laser pulses can induce competing scattering due to plasma cavitation [165]. However, with further technological development, these challenges could be overcome and the multi-beam configuration could also be a viable approach to observe photon-photon scattering at facilities such as NSF OPAL and SEL.

List of Publications

Development of a sapphire microstrip detector for gamma beam monitoring

Authors: G. Avoni, M. Benettoni, M. Bruschi, A. Cian, F. Dal Corso, U. Dosselli, K. Fleck, E. Gerstmayr, M. Giorato, P. Grutta, F. Lasagni Manghi, B. Margesin, M. Morandin, G. Sarri, S. Vasiukov, M. Zuffa

Published: Nuclear Instruments and Methods in Physics Research Section A: Accelerators, Spectrometers, Detectors and Associated Equipment, **1068**, 169752 (2024)

Technical Design Report for the LUXE Experiment

Authors: Abramowicz, H., Almanza Soto, M., Altarelli, M. et al.

Published: European Physical Journal Special Topics, **233**, 1709 (2024)

Dependence of the number-weighted angular distribution of Compton-scattered photon beams on the laser intensity

Authors: Fleck, K., Blackburn, T., Gerstmayr, E., Bruschi, M., Grutta, P., Morandin, M., Sarri, G.

Published: Physical Review A, **110**, 023510 (2024)

Experimental characterization of a single-shot spectrometer for high-flux, GeV-scale gamma-ray beams

Authors: Cavanagh, N., Fleck, K., Streeter, M. J. V., Gerstmayr, E., Dickson, L. T., Ballage, C., Cadas, R., Calvin, L., Dobosz Dufrénoy, S., Moulanier, I., Romagnani, L., Vasilovici, O., Whitehead, A., Specka, A., Cros, B., Sarri, G.

Published: Physical Review Research, **5**, 043046 (2023)

Instrumentation challenges of the strong-field QED experiment LUXE at the European XFEL

Authors: Fleck, K.

Pubslished: Journal of Instrumentation, **17**, C08022 (2022)

Conceptual Deisgn Report for the LUXE Experiment

Authors: Abramowicz, H., Acosta, U., Altarelli, M., et al.

Published: European Physical Journal Special Topics, **230**, 2445 (2021)

Conceptual Design of a High-flux Multi-GeV Gamma-ray Spectrometer

Authors: Fleck, K., Cavanagh, N., Sarri, G.

Published: Scientific Reports, **10**, 9894 (2020)

Role of the Author

The author performed all of the simulation and analysis work presented herein, including as part of a wider collaboration, unless otherwise stated and referenced in the text.

In Chapter 4, the design of the detector and the Bayesian reconstruction algorithm were developed with N. Cavanagh. The LUXE performance simulations and subsequent analysis were performed by the author, using some simulation results and analysis tools devised within the LUXE collaboration as benchmarking. The experiment at Apollon, including planning, assembly and data taking, involved all authors of [22] jointly. The electron spectroscopy and plasma diagnostics were overseen and analysed by M.J.V. Streeter, L.T. Dickson and R. Cadas. Calibration of the spectrometer and scintillator images was done by N. Cavanagh and E. Gerstmayr; the subsequent analysis of the electron and positron spectra, as well as the use of the deconvolution algorithm to reconstruct the photon spectrum was done by the author with input from E. Gerstmayr. Additional GEANT4 simulations of the experimental setup were also performed by the author.

The theory of Chapter 5 was developed mainly by T. Blackburn, with all PTARMIGAN simulations performed by the author and jointly analysed along with T. Blackburn and E. Gerstmayr. The author was also a part of the collaboration responsible for the design of gamma beam profiler in [145], which involved running PTARMIGAN, FLUKA and GEANT4 simulations within the context of LUXE to estimate detector performance and achievable signal-to-noise ratios. Application of the theory developed by T. Blackburn to this data was also done by the author.

The entirety of Chapter 6 was done by the author, following the original conception in [79, 105]. R. Watt aided in the use of the GEANT4 extension for QED processes and discussions with

B. Kettle helped form the rationale for Section 6.1.2.

Bibliography

[1] G. Gabrielse et al. *New Determination of the Fine Structure Constant from the Electron g Value and QED*. In: Physical Review Letters 97.3 (July 2006). ISSN: 1079-7114. DOI: 10.1103/physrevlett.97.030802. URL: http://dx.doi.org/10.1103/PhysRevLett.97.030802.

[2] A. Fedotov et al. *Advances in QED with intense background fields*. In: Phys. Rep. 1010 (2023), pp. 1–138. DOI: 10.1016/j.physrep.2023.01.003.

[3] S. A. Olausen and V. M. Kaspi. *THE McGILL MAGNETAR CATALOG*. In: The Astrophysical Journal Sup 212.1 (Apr. 2014), p. 6. ISSN: 1538-4365. DOI: 10.1088/0067-0049/212/1/6. URL: http://dx.doi.org/10.1088/0067-0049/212/1/6.

[4] B. Crinquand et al. *Multidimensional Simulations of Ergospheric Pair Discharges around Black Holes*. In: Physical Review Letters 124.14 (Apr. 2020). ISSN: 1079-7114. DOI: 10.1103/physrevlett.124.145101. URL: http://dx.doi.org/10.1103/PhysRevLett.124.145101.

[5] C. M. Kim and S. P. Kim. *Magnetars as laboratories for strong field QED*. In: 5TH INTERNATIONAL CONFERENCE ON EARTH SCIENCE, MINERALS, AND ENERGY (IC Vol. 3019. AIP Publishing, 2024, p. 020013. DOI: 10.1063/5.0215939. URL: http://dx.doi.org/10.1063/5.0215939.

[6] Ulrik I. Uggerhøj. *The interaction of relativistic particles with strong crystalline fields*. In: Reviews of Modern Physics 77.4 (Oct. 2005), 1131–1171. ISSN: 1539-0756. DOI: 10.1103/revmodphys.77.1131. URL: http://dx.doi.org/10.1103/RevModPhys.77.1131.

[7] P. Zhang et al. *Relativistic plasma physics in supercritical fields*. In: Physics of Plasmas 27.5 (May 2020). ISSN: 1089-7674. DOI: 10.1063/1.5144449. URL: http://dx.doi.org/10.1063/1.5144449.

[8] A. Matheron et al. *Probing strong-field QED in beam-plasma collisions*. In: Communications Physics 6.1 (June 2023). ISSN: 2399-3650. DOI: 10.1038/s42005-023-01263-4. URL: http://dx.doi.org/10.1038/s42005-023-01263-4.

[9] V. Yakimenko et al. *Prospect of Studying Nonperturbative QED with Beam-Beam Collisions*. In: Physical Review Letters 122.19 (May 2019). ISSN: 1079-7114. DOI: 10.1103/physrevlett.122.190404. URL: http://dx.doi.org/10.1103/PhysRevLett.122.190404.

[10] D. Strickland and G. Mourou. *Compression of amplified chirped optical pulses*. In: Opt. Commun. 56.3 (Dec. 1985), pp. 219–221. DOI: 10.1016/0030-4018(85)90120-8.

[11] J. W. Yoon et al. *Realization of laser intensity over* 10^{23} *W/cm*^{2}. In: Optica 8.5 (May 2021), p. 630. ISSN: 2334-2536. DOI: 10.1364/optica.420520. URL: http://dx.doi.org/10.1364/OPTICA.420520.

[12] C. N. Danson et al. *Petawatt and exawatt class lasers worldwide*. In: High Power Laser Sci. Eng. 7 (2019), e54. DOI: 10.1017/hpl.2019.36.

[13] C. Bula et al. *Observation of Nonlinear Effects in Compton Scattering*. In: Phys. Rev. Lett. 76 (17 1996), pp. 3116–3119. DOI: 10.1103/PhysRevLett.76.3116. URL: https://link.aps.org/doi/10.1103/PhysRevLett.76.3116.

[14] D. L. Burke et al. *Positron Production in Multiphoton Light-by-Light Scattering*. In: Phys. Rev. Lett. 79 (9 1997), pp. 1626–1629. DOI: 10.1103/PhysRevLett.79.1626. URL: https://link.aps.org/doi/10.1103/PhysRevLett.79.1626.

[15] G. Sarri et al. *Ultrahigh Brilliance Multi-MeV $\ensuremath{\gamma}$-Ray Beams from Nonlinear Relativistic Thomson Scattering*. In: Phys. Rev. Lett. 113.22 (Nov. 2014). Publisher: American Physical Society, p. 224801. DOI: 10.1103/PhysRevLett.113.

224801. URL: https://link.aps.org/doi/10.1103/PhysRevLett.113.224801 (visited on 03/27/2023).

[16] I. C. E. Turcu et al. *High Field Physics and QED experiments at ELI-NP*. English. In: Rom. Rep. Phys. 68 (2016), S145–1231. ISSN: 1221-1451.

[17] J. M. Cole et al. *Experimental Evidence of Radiation Reaction in the Collision of a High-Intensity Laser Pulse with a Laser-Wakefield Accelerated Electron Beam*. In: Phys. Rev. X 8 (1 2018), p. 011020. DOI: 10.1103/PhysRevX.8.011020. URL: https://link.aps.org/doi/10.1103/PhysRevX.8.011020.

[18] K. Poder et al. *Experimental Signatures of the Quantum Nature of Radiation Reaction in the Field of an Ultraintense Laser*. In: Phys. Rev. X 8.3 (July 2018). Publisher: American Physical Society, p. 031004. DOI: 10.1103/PhysRevX.8.031004. URL: https://link.aps.org/doi/10.1103/PhysRevX.8.031004 (visited on 06/13/2023).

[19] S. Meuren. *Probing Strong-field QED at FACET II (SLAC E-320)*. URL: https://conferences.slac.stanford.edu/sites/default/files/2023-08/Wed_01_sfqed_2019.pdf. 2019.

[20] H. Abramowicz et al. *Conceptual design report for the LUXE experiment*. en. In: Eur. Phys. J. Spec. Top. 230.11 (Oct. 2021), pp. 2445–2560. ISSN: 1951-6401. DOI: 10.1140/epjs/s11734-021-00249-z. URL: https://doi.org/10.1140/epjs/s11734-021-00249-z (visited on 05/10/2023).

[21] H. Abramowicz et al. *Technical Design Report for the LUXE Experiment*. 2023. arXiv: 2308.00515 [hep-ex].

[22] K. Fleck. *Instrumentation challenges of the strong-field QED experiment LUXE at the European XFEL**. In: Journal of Instrumentation 17.08 (Aug. 2022), p. C08022. ISSN: 1748-0221. DOI: 10.1088/1748-0221/17/08/c08022. URL: http://dx.doi.org/10.1088/1748-0221/17/08/C08022.

[23] A. Santra. *Detector challenges of the strong-field QED experiment LUXE at the European XFEL*. In: Journal of Instrumentation 18.08 (Aug. 2023), p. C08003. ISSN: 1748-0221.

DOI: 10.1088/1748-0221/18/08/c08003. URL: http://dx.doi.org/10.1088/1748-0221/18/08/C08003.

[24] H. Abramowicz et al. *Performance and Molière radius measurements using a compact prototype of LumiCal in an electron test beam*. In: The European Physical Journal C 79.7 (July 2019). ISSN: 1434-6052. DOI: 10.1140/epjc/s10052-019-7077-9. URL: http://dx.doi.org/10.1140/epjc/s10052-019-7077-9.

[25] K. Fleck, N. Cavanagh, and G. Sarri. *Conceptual Design of a High flux Multi-GeV Gamma-ray Spectrometer*. English. In: Nature Scientific Reports 10 (June 2020). ISSN: 2045-2322. DOI: 10.1038/s41598-020-66832-x.

[26] N. Cavanagh et al. *Experimental characterization of a single-shot spectrometer for high-flux, GeV-scale gamma-ray beams*. In: Phys. Rev. Res. 5 (4 2023), p. 043046. DOI: 10.1103/PhysRevResearch.5.043046. URL: https://link.aps.org/doi/10.1103/PhysRevResearch.5.043046.

[27] A. Di Piazza et al. *Extremely high-intensity laser interactions with fundamental quantum systems*. In: Rev. Mod. Phys. 84.3 (Aug. 2012). arXiv:1111.3886 [hep-ph, physics:physics], pp. 1177–1228. ISSN: 0034-6861, 1539-0756. DOI: 10.1103/RevModPhys.84.1177. URL: http://arxiv.org/abs/1111.3886 (visited on 05/03/2023).

[28] W. Greiner and J. Reinhardt. *Quantum electrodynamics*. 1992. ISBN: 978-3-540-87560-4.

[29] W. H. Furry. *On Bound States and Scattering in Positron Theory*. In: Phys. Rev. 81 (1 1951), pp. 115–124. DOI: 10.1103/PhysRev.81.115. URL: https://link.aps.org/doi/10.1103/PhysRev.81.115.

[30] L. D. Landau and E. M. Lifschitz. *The Classical Theory of Fields*. Vol. Volume 2. Course of Theoretical Physics. Oxford: Pergamon Press, 1975. ISBN: 978-0-08-018176-9.

[31] H. Mitter. *Quantum Electrodynamics in Laser Fields*. In: Electromagnetic Interactions and Field Theory. Springer Vienna, 1975, 397–468. ISBN: 9783709184240. DOI: 10.1007/978-3-7091-8424-0_7. URL: http://dx.doi.org/10.1007/978-3-7091-8424-0_7.

[32] V I Ritus. *Quantum effects of the interaction of elementary particles with an intense electromagnetic field*. In: J. Sov. Laser Res.; (United States) 6.497 (Sept. 1985). DOI: 10.1007/BF01120220.

[33] T. G. Blackburn. *Radiation reaction in electron–beam interactions with high-intensity lasers*. en. In: Rev. Mod. Plasma Phys. 4.1 (Mar. 2020), p. 5. ISSN: 2367-3192. DOI: 10.1007/s41614-020-0042-0. URL: https://doi.org/10.1007/s41614-020-0042-0 (visited on 01/30/2023).

[34] F. Sauter. *Über das Verhalten eines Elektrons im homogenen elektrischen Feld nach der relativistischen Theorie Diracs*. de. In: Zeitschrift für Physik 69.11 (Nov. 1931), pp. 742–764. ISSN: 0044-3328. DOI: 10.1007/BF01339461. URL: https://doi.org/10.1007/BF01339461 (visited on 02/21/2025).

[35] W. Heisenberg and H. Euler. *Folgerungen aus der Diracschen Theorie des Positrons*. In: Zeitschrift für Physik 98.11–12 (Nov. 1936), 714–732. ISSN: 1434-601X. DOI: 10.1007/bf01343663. URL: http://dx.doi.org/10.1007/BF01343663.

[36] Julian Schwinger. *On gauge invariance and vacuum polarization*. In: Physical Review 82.5 (1951), pp. 664–679. DOI: 10.1103/PHYSREV.82.664.

[37] A. I. Nikishov. *Pair Production by a Constant External Field*. In: Soviet Journal of Experimental and The 30 (Jan. 1969). Publisher: Springer ADS Bibcode: 1969JETP...30..660N, p. 660. ISSN: 1063-7761. URL: https://ui.adsabs.harvard.edu/abs/1969JETP...30..660N (visited on 10/31/2024).

[38] A. Gonoskov et al. *Charged particle motion and radiation in strong electromagnetic fields*. en. In: Reviews of Modern Physics 94.4 (Oct. 2022), p. 045001. ISSN: 0034-6861, 1539-0756. DOI: 10.1103/RevModPhys.94.045001. URL: https://link.aps.org/doi/10.1103/RevModPhys.94.045001 (visited on 03/01/2023).

[39] A. Fedotov. *Conjecture of perturbative QED breakdown at* $\alpha\chi^{2/3} \geq 1$. In: Journal of Physics: Conference 826 (Apr. 2017), p. 012027. ISSN: 1742-6596. DOI: 10.1088/1742-6596/826/1/012027. URL: http://dx.doi.org/10.1088/1742-6596/826/1/012027.

[40] A I Nikishov and V I Ritus. *QUANTUM PROCESSES IN THE FIELD OF A PLANE ELECTROMAGNETIC WAVE AND IN A CONSTANT FIELD. I.* In: J. Exptl. Theoret. Phys. (U.S.S.R.) 19.2 (1964), pp. 776–796.

[41] A I Nikishov and V I Ritus. *PAIR PRODUCTION BY A PHOTON AND PHOTON EMISSION BY AN ELECTRON IN THE FIELD OF AN INTENSE ELECTROMAGNETIC WAVE AND IN A CONSTANT FIELD*. Tech. rep. Issue: 6 Volume: 25. 1967, pp. 1707–1719.

[42] H. R. Reiss. *Absorption of Light by Light*. In: Journal of Mathematical Physics 3.1 (Jan. 1962), 59–67. ISSN: 1089-7658. DOI: 10.1063/1.1703787. URL: http://dx.doi.org/10.1063/1.1703787.

[43] V. N. Baier, V. M. Katkov, and V. M. Strakhovenko. *Electromagnetic processes at high energies in oriented single crystals*. 1998. ISBN: 978-981-02-1603-0.

[44] I.A. Aleksandrov, G. Plunien, and V.M. Shabaev. *Locally-constant field approximation in studies of electron-positron pair production in strong external fields*. In: Physical Review D 99.1 (Jan. 2019). Publisher: American Physical Society, p. 016020. DOI: 10.1103/PhysRevD.99.016020. URL: https://link.aps.org/doi/10.1103/PhysRevD.99.016020 (visited on 10/30/2024).

[45] S. Montefiori and M. Tamburini. *SFQEDtoolkit: A high-performance library for the accurate modeling of strong-field QED processes in PIC and Monte Carlo codes*. In: Computer Physics Communications 292 (Nov. 2023), p. 108855. ISSN: 0010-4655. DOI: 10.1016/j.cpc.2023.108855. URL: http://dx.doi.org/10.1016/j.cpc.2023.108855.

[46] A. Di Piazza et al. *Improved local-constant-field approximation for strong-field QED codes*. In: Physical Review A 99.2 (Feb. 2019). ISSN: 2469-9934. DOI: 10.1103/physreva.99.022125. URL: http://dx.doi.org/10.1103/PhysRevA.99.022125.

[47] A. Ilderton, B. King, and D. Seipt. *An extended locally constant field approximation for nonlinear Compton scattering*. In: Physical Review A 99.4 (Apr. 2019). arXiv:1808.10339

[hep-ph, physics:physics], p. 042121. ISSN: 2469-9926, 2469-9934. DOI: 10.1103/PhysRevA.99.042121. URL: http://arxiv.org/abs/1808.10339 (visited on 06/27/2023).

[48] T. Heinzl, B. King, and A. J. MacLeod. *Locally monochromatic approximation to QED in intense laser fields*. In: Phys. Rev. A 102.6 (2020), p. 063110.

[49] V. B. Berestetskii, E. M. Lifshitz, and L. P. Pitaevskii. *QUANTUM ELECTRODYNAMICS*. Vol. 4. Course of Theoretical Physics. Oxford: Pergamon Press, 1982. ISBN: 978-0-7506-3371-0.

[50] M. Abramowitz and I. A. Stegun. *Handbook of Mathematical Functions with Formulas, Graphs, and Mathematical Tables*. ninth Dover printing, tenth GPO printing. New York: Dover, 1964.

[51] D. Seipt. *Volkov States and Non-linear Compton Scattering in Short and Intense Laser Pulses*. arXiv:1701.03692 [hep-ph, physics:physics]. Jan. 2017. DOI: 10.48550/arXiv.1701.03692. URL: http://arxiv.org/abs/1701.03692 (visited on 01/30/2023).

[52] C. N. Harvey. *In situ characterization of ultraintense laser pulses*. In: Phys. Rev. Accel. Beams 21 (11 2018), p. 114001. DOI: 10.1103/PhysRevAccelBeams.21.114001. URL: https://link.aps.org/doi/10.1103/PhysRevAccelBeams.21.114001.

[53] S. V. Bulanov et al. *Relativistic mirrors in plasmas. Novel results and perspectives*. In: Physics-Uspekhi 56.5 (May 2013), 429–464. ISSN: 1468-4780. DOI: 10.3367/ufne.0183.201305a.0449. URL: http://dx.doi.org/10.3367/UFNe.0183.201305a.0449.

[54] R. A. Watt et al. *Monte Carlo modeling of the linear Breit-Wheeler process within the geant4 framework*. In: Physical Review Accelerators and Beams 26.5 (May 2023). ISSN: 2469-9888. DOI: 10.1103/physrevaccelbeams.26.054601. URL: http://dx.doi.org/10.1103/PhysRevAccelBeams.26.054601.

[55] A. Di Piazza et al. *Implementing nonlinear Compton scattering beyond the local-constant-field approximation*. In: Phys. Rev. A 98 (1 2018), p. 012134. DOI: 10.1103/PhysRevA.98.012134. URL: https://link.aps.org/doi/10.1103/PhysRevA.98.012134.

[56] T. G. Blackburn and B. King. *Higher fidelity simulations of nonlinear Breit–Wheeler pair creation in intense laser pulses*. en. In: The European Physical Journal C 82.1 (Jan. 2022), p. 44. ISSN: 1434-6052. DOI: `10.1140/epjc/s10052-021-09955-3`. URL: `https://doi.org/10.1140/epjc/s10052-021-09955-3` (visited on 11/11/2024).

[57] M. Abraham. *Theorie der Elektrizität. Zweiter Band: Elektromagnetische Theorie der Strahlung: von Dr. M. Abraham. Mit 5 Textfig., 404 S. 80. Verlag von B. G. Teubner, Leipzig, 1905*. In: Monatshefte für Mathematik und Physik 17.1 (Dec. 1906), A39–A39. ISSN: 1436-5081. DOI: `10.1007/bf01697706`. URL: `http://dx.doi.org/10.1007/bf01697706`.

[58] P. A. M. Dirac. *Classical theory of radiating electrons*. In: Proceedings of the Royal Society of London. S 167.929 (Jan. 1938). Publisher: Royal Society, pp. 148–169. DOI: `10.1098/rspa.1938.0124`. URL: `https://royalsocietypublishing.org/doi/10.1098/rspa.1938.0124`.

[59] J. D. Jackson. *Classical Electrodynamics*. Wiley, 1998. ISBN: 978-0-471-30932-1.

[60] David A. Burton and Adam Noble. *Aspects of electromagnetic radiation reaction in strong fields*. In: Contemporary Physics 55.2 (Feb. 2014), 110–121. ISSN: 1366-5812. DOI: `10.1080/00107514.2014.886840`. URL: `http://dx.doi.org/10.1080/00107514.2014.886840`.

[61] A. Di Piazza. *Exact Solution of the Landau-Lifshitz Equation in a Plane Wave*. en. In: Lett. Math. Phys. 83.3 (Mar. 2008), pp. 305–313. ISSN: 1573-0530. DOI: `10.1007/s11005-008-0228-9`. URL: `https://doi.org/10.1007/s11005-008-0228-9` (visited on 05/10/2023).

[62] I. M. Ternov. *Synchrotron radiation*. en. In: Physics-Uspekhi 38.4 (Apr. 1995). Publisher: IOP Publishing, p. 409. ISSN: 1063-7869. DOI: `10.1070/PU1995v038n04ABEH000082`. URL: `https://iopscience.iop.org/article/10.1070/PU1995v038n04ABEH000082/meta` (visited on 02/13/2023).

[63] T. G. Blackburn, B. King, and S. Tang. *Simulations of laser-driven strong-field QED with Ptarmigan: Resolving wavelength-scale interference and γ-ray polarization*. In:

Phys. Plasmas 30.9 (Sept. 2023), p. 093903. ISSN: 1070-664X. DOI: 10.1063/5.0159963. eprint: https://pubs.aip.org/aip/pop/article-pdf/doi/10.1063/5.0159963/18131627/093903_1_5.0159963.pdf. URL: https://doi.org/10.1063/5.0159963.

[64] N. Neitz and A. Di Piazza. *Stochasticity Effects in Quantum Radiation Reaction*. In: Phys. Rev. Lett. 111 (5 2013), p. 054802. DOI: 10.1103/PhysRevLett.111.054802. URL: https://link.aps.org/doi/10.1103/PhysRevLett.111.054802.

[65] M. Vranic et al. *Quantum radiation reaction in head-on laser-electron beam interaction*. en. In: New J. Phys. 18.7 (July 2016). Publisher: IOP Publishing, p. 073035. ISSN: 1367-2630. DOI: 10.1088/1367-2630/18/7/073035. URL: https://dx.doi.org/10.1088/1367-2630/18/7/073035 (visited on 03/13/2023).

[66] C. P. Ridgers et al. *Signatures of quantum effects on radiation reaction in laser–electron-beam collisions*. en. In: J. Plasma Phys. 83.5 (Oct. 2017), p. 715830502. ISSN: 0022-3778, 1469-7807. DOI: 10.1017/S0022377817000642. URL: https://www.cambridge.org/core/product/identifier/S0022377817000642/type/journal_article (visited on 05/26/2023).

[67] C. D. Baird et al. *Realising single-shot measurements of quantum radiation reaction in high-intensity lasers*. In: New J. Phys. 21.5 (May 2019), p. 053030. ISSN: 1367-2630. DOI: 10.1088/1367-2630/ab1baf. URL: http://dx.doi.org/10.1088/1367-2630/ab1baf.

[68] Tobias N. Wistisen et al. *Experimental evidence of quantum radiation reaction in aligned crystals*. en. In: Nature Communications 9.1 (Feb. 2018). Publisher: Nature Publishing Group, p. 795. ISSN: 2041-1723. DOI: 10.1038/s41467-018-03165-4. URL: https://www.nature.com/articles/s41467-018-03165-4 (visited on 10/29/2024).

[69] B. De Tollis. *Dispersive approach to photon-photon scattering*. en. In: Il Nuovo Cimento (1955-1965) 32.3 (May 1964), pp. 757–768. ISSN: 1827-6121. DOI: 10.1007/BF02735895. URL: https://doi.org/10.1007/BF02735895 (visited on 05/06/2024).

[70] B. De Tollis. *The scattering of photons by photons*. en. In: Il Nuovo Cimento (1955-1965) 35.4 (Feb. 1965), pp. 1182–1193. ISSN: 1827-6121. DOI: 10.1007/BF02735534. URL: https://doi.org/10.1007/BF02735534 (visited on 05/06/2024).

[71] M. Marklund and P. K. Shukla. *Nonlinear collective effects in photon-photon and photon-plasma interactions*. In: Reviews of Modern Physics 78.2 (May 2006). Publisher: American Physical Society, pp. 591–640. DOI: 10.1103/RevModPhys.78.591. URL: https://link.aps.org/doi/10.1103/RevModPhys.78.591 (visited on 11/08/2024).

[72] W. Dittrich and M. Reuter. *Introduction*. In: Effective Lagrangians in Quantum Electrodynamics. Berlin, Heidelberg: Springer Berlin Heidelberg, 1985, pp. 1–28. ISBN: 978-3-540-39259-0. DOI: 10.1007/3-540-15182-6_1. URL: https://doi.org/10.1007/3-540-15182-6_1.

[73] M. E. Peskin and D. V. Schroeder. *An Introduction to quantum field theory*. Reading, USA: Addison-Wesley, 1995. ISBN: 978-0-201-50397-5, 978-0-429-50355-9, 978-0-429-49417-8. DOI: 10.1201/9780429503559.

[74] T. Heinzl, B. King, and D. Liu. *Coherent enhancement of QED cross-sections in electromagnetic backgrounds*. 2024. arXiv: 2412.10574 [hep-ph]. URL: https://arxiv.org/abs/2412.10574.

[75] F. Moulin, D. Bernard, and F. Amiranoff. *Photon-photon elastic scattering in the visible domain*. In: Zeitschrift für Physik C: Particles and Fields 72.4 (Dec. 1996), 607–611. ISSN: 1431-5858. DOI: 10.1007/s002880050282. URL: http://dx.doi.org/10.1007/s002880050282.

[76] D. Bernard et al. *Search for stimulated photon-photon scattering in vacuum*. In: The European Physical Journal D 10.1 (Mar. 2000), 141–145. ISSN: 1434-6060. DOI: 10.1007/s100530050535. URL: http://dx.doi.org/10.1007/s100530050535.

[77] T. Inada et al. *Search for photon–photon elastic scattering in the X-ray region*. In: Physics Letters B 732 (May 2014), 356–359. ISSN: 0370-2693. DOI: 10.1016/j.

physletb.2014.03.054. URL: http://dx.doi.org/10.1016/j.physletb.2014.03.054.

[78] T. Yamaji et al. *An experiment of X-ray photon–photon elastic scattering with a Laue-case beam collider*. In: Physics Letters B 763 (Dec. 2016), 454–457. ISSN: 0370-2693. DOI: 10.1016/j.physletb.2016.11.003. URL: http://dx.doi.org/10.1016/j.physletb.2016.11.003.

[79] R. Watt et al. *Bounding elastic photon-photon scattering at* $\sqrt{s} \approx 1$ *MeV using a laser-plasma platform*. In: Physics Letters B 861 (Feb. 2025), p. 139247. ISSN: 0370-2693. DOI: 10.1016/j.physletb.2025.139247. URL: http://dx.doi.org/10.1016/j.physletb.2025.139247.

[80] G. Jarlskog et al. *Measurement of Delbrück Scattering and Observation of Photon Splitting at High Energies*. In: Phys. Rev. D 8 (11 1973), pp. 3813–3823. DOI: 10.1103/PhysRevD.8.3813. URL: https://link.aps.org/doi/10.1103/PhysRevD.8.3813.

[81] *Evidence for light-by-light scattering in heavy-ion collisions with the ATLAS detector at the LHC*. In: Nature Physics 13.9 (Aug. 2017), 852–858. ISSN: 1745-2481. DOI: 10.1038/nphys4208. URL: http://dx.doi.org/10.1038/nphys4208.

[82] A.M. Sirunyan and et al. *Evidence for light-by-light scattering and searches for axion-like particles in ultraperipheral PbPb collisions at* $\sqrt{s_{NN}} = 5.02$ *TeV*. In: Physics Letters B 797 (2019), p. 134826. ISSN: 0370-2693. DOI: 10.1016/j.physletb.2019.134826. URL: http://dx.doi.org/10.1016/j.physletb.2019.134826.

[83] G. Aad et al. *Observation of Light-by-Light Scattering in Ultraperipheral* Pb + Pb *Collisions with the ATLAS Detector*. In: Phys. Rev. Lett. 123 (5 2019), p. 052001. DOI: 10.1103/PhysRevLett.123.052001. URL: https://link.aps.org/doi/10.1103/PhysRevLett.123.052001.

[84] F. Moulin and D. Bernard. *Four-wave interaction in gas and vacuum: definition of a third-order nonlinear effective susceptibility in vacuum:* χ*vacuum(3)*. In: Optics Communications

164.1–3 (June 1999), 137–144. ISSN: 0030-4018. DOI: 10.1016/s0030-4018(99)00169-8. URL: http://dx.doi.org/10.1016/S0030-4018(99)00169-8.

[85] B King and C H Keitel. *Photon–photon scattering in collisions of intense laser pulses*. In: New Journal of Physics 14.10 (Oct. 2012), p. 103002. ISSN: 1367-2630. DOI: 10.1088/1367-2630/14/10/103002. URL: http://dx.doi.org/10.1088/1367-2630/14/10/103002.

[86] B. King, H. Hu, and B. Shen. *Three-pulse photon-photon scattering*. In: Phys. Rev. A 98 (2 2018), p. 023817. DOI: 10.1103/PhysRevA.98.023817. URL: https://link.aps.org/doi/10.1103/PhysRevA.98.023817.

[87] Sh. Zh. Akhmadaliev et al. *Experimental Investigation of High-Energy Photon Splitting in Atomic Fields*. In: Phys. Rev. Lett. 89 (6 2002), p. 061802. DOI: 10.1103/PhysRevLett.89.061802. URL: https://link.aps.org/doi/10.1103/PhysRevLett.89.061802.

[88] H. Bethe and W. Heitler. *On the Stopping of fast particles and on the creation of positive electrons*. In: Proc. Roy. Soc. Lond. A 146 (1934), pp. 83–112. DOI: 10.1098/rspa.1934.0140.

[89] H. A. Bethe and L. C. Maximon. *Theory of Bremsstrahlung and Pair Production. I. Differential Cross Section*. In: Phys. Rev. 93 (4 1954), pp. 768–784. DOI: 10.1103/PhysRev.93.768. URL: https://link.aps.org/doi/10.1103/PhysRev.93.768.

[90] Y. Tsai. *Pair production and bremsstrahlung of charged leptons*. In: Rev. Mod. Phys. 46 (4 1974), pp. 815–851. DOI: 10.1103/RevModPhys.46.815. URL: https://link.aps.org/doi/10.1103/RevModPhys.46.815.

[91] S. R. Klein. *Pair production from 10 GeV to 10 ZeV*. In: Radiation Physics and Chemistry 75.6 (2006), pp. 696–711. DOI: 10.1016/j.radphyschem.2005.09.005. URL: https://doi.org/10.1016\%2Fj.radphyschem.2005.09.005.

[92] Geant4 Collaboration. *Geant4 Physics Reference Manual*. 2017.

[93] Y. S. Tsai and Van Whitis. *Thick-Target Bremsstrahlung and Target Considerations for Secondary-Particle Production by Electrons*. In: Phys. Rev. 149 (4 1966), pp. 1248–1257. DOI: 10.1103/PhysRev.149.1248. URL: https://link.aps.org/doi/10.1103/PhysRev.149.1248.

[94] S. Chen et al. *MeV-Energy X Rays from Inverse Compton Scattering with Laser-Wakefield Accelerated Electrons*. In: Phys. Rev. Lett. 110 (15 2013), p. 155003. DOI: 10.1103/PhysRevLett.110.155003. URL: https://link.aps.org/doi/10.1103/PhysRevLett.110.155003.

[95] W. Yan et al. *High-order multiphoton Thomson scattering*. en. In: Nat. Photonics 11.8 (Aug. 2017). Number: 8 Publisher: Nature Publishing Group, pp. 514–520. ISSN: 1749-4893. DOI: 10.1038/nphoton.2017.100. URL: https://www.nature.com/articles/nphoton.2017.100 (visited on 09/29/2023).

[96] A. Hannasch et al. *Compact spectroscopy of keV to MeV X-rays from a laser wakefield accelerator*. In: Scientific Reports 11.1 (July 2021). ISSN: 2045-2322. DOI: 10.1038/s41598-021-93689-5. URL: http://dx.doi.org/10.1038/s41598-021-93689-5.

[97] F C Salgado et al. *Towards pair production in the non-perturbative regime*. In: New Journal of Physics 23.10 (Oct. 2021), p. 105002. ISSN: 1367-2630. DOI: 10.1088/1367-2630/ac2921. URL: http://dx.doi.org/10.1088/1367-2630/ac2921.

[98] P. Jucha, M. Kłusek-Gawenda, and A. Szczurek. *Light-by-light scattering in ultra-peripheral collisions of heavy ions at two future detectors*. In: Physical Review D 109.1 (Jan. 2024). ISSN: 2470-0029. DOI: 10.1103/physrevd.109.014004. URL: http://dx.doi.org/10.1103/PhysRevD.109.014004.

[99] F. C. Salgado et al. *Towards pair production in the non-perturbative regime*. In: New J. Phys. 23.10 (Oct. 2021), p. 105002. ISSN: 1367-2630. DOI: 10.1088/1367-2630/ac2921. URL: http://dx.doi.org/10.1088/1367-2630/ac2921.

[100] S. Huang. *Probing new physics at the LUXE experiment*. In: PoS ICHEP2022 (2022), p. 150. DOI: 10.22323/1.414.0150.

[101] N. Ahmadiniaz et al. *Letter of Intent: Towards a Vacuum Birefringence Experiment at the Helmholtz International Beamline for Extreme Fields*. 2024. arXiv: 2405.18063 [physics.ins-det]. URL: https://arxiv.org/abs/2405.18063.

[102] A. Ejlli et al. *The PVLAS experiment: A 25 year effort to measure vacuum magnetic birefringence*. In: Physics Reports 871 (Aug. 2020), 1–74. ISSN: 0370-1573. DOI: 10.1016/j.physrep.2020.06.001. URL: http://dx.doi.org/10.1016/j.physrep.2020.06.001.

[103] M. Sangal, C. H. Keitel, and M. Tamburini. *Observing light-by-light scattering in vacuum with an asymmetric photon collider*. In: Physical Review D 104.11 (Dec. 2021). ISSN: 2470-0029. DOI: 10.1103/physrevd.104.l111101. URL: http://dx.doi.org/10.1103/PhysRevD.104.L111101.

[104] O. J. Pike et al. *A photon–photon collider in a vacuum hohlraum*. In: Nature Photonics 8.6 (May 2014), 434–436. ISSN: 1749-4893. DOI: 10.1038/nphoton.2014.95. URL: http://dx.doi.org/10.1038/nphoton.2014.95.

[105] B Kettle et al. *A laser–plasma platform for photon–photon physics: the two photon Breit–Wheeler process*. In: New Journal of Physics 23.11 (Nov. 2021), p. 115006. ISSN: 1367-2630. DOI: 10.1088/1367-2630/ac3048. URL: http://dx.doi.org/10.1088/1367-2630/ac3048.

[106] T. G. Blackburn. *Ptarmigan: Particle-tracking code that models strong-field QED interactions*. 2023. URL: https://github.com/tgblackburn/ptarmigan.

[107] G. Battistoni et al. *Overview of the FLUKA code*. In: Annals of Nuclear Energy 82 (Aug. 2015), 10–18. ISSN: 0306-4549. DOI: 10.1016/j.anucene.2014.11.007. URL: http://dx.doi.org/10.1016/j.anucene.2014.11.007.

[108] C. Ahdida et al. *New Capabilities of the FLUKA Multi-Purpose Code*. In: Frontiers in Physics 9 (Jan. 2022). ISSN: 2296-424X. DOI: 10.3389/fphy.2021.788253. URL: http://dx.doi.org/10.3389/fphy.2021.788253.

[109] S. Agostinelli et al. *Geant4—a simulation toolkit*. In: Nuclear Instruments and Methods in Physics Resea
506.3 (July 2003), 250–303. ISSN: 0168-9002. DOI: 10.1016/s0168-9002(03)01368-8. URL: http://dx.doi.org/10.1016/S0168-9002(03)01368-8.

[110] J. Allison et al. *Geant4 developments and applications*. In: IEEE Transactions on Nuclear Science 53.1 (2006), pp. 270–278. DOI: 10.1109/TNS.2006.869826.

[111] J. Allison et al. *Recent developments in Geant4*. In: Nuclear Instruments and Methods in Physics Researc
835 (Nov. 2016), 186–225. ISSN: 0168-9002. DOI: 10.1016/j.nima.2016.06.125. URL: http://dx.doi.org/10.1016/j.nima.2016.06.125.

[112] K. J. Oxford. *Cosmic gamma ray bursts*. In: Nature (London) 267 (1977), p. 103.

[113] P. T. Greenlees et al. *Shell-Structure and Pairing Interaction in Superheavy Nuclei: Rotational Properties of the Z=104 Nucleus* ^{256}Rf. In: Phys. Rev. Lett. 109 (1 2012), p. 012501. DOI: 10.1103/PhysRevLett.109.012501. URL: https://link.aps.org/doi/10.1103/PhysRevLett.109.012501.

[114] W. Schumaker et al. *Measurements of high-energy radiation generation from laser-wakefield accelerated electron beams*. In: Physics of Plasmas 21.5 (2014), p. 056704. DOI: 10.1063/1.4875336. eprint: https://doi.org/10.1063/1.4875336. URL: https://doi.org/10.1063/1.4875336.

[115] Y. Glinec et al. *High-Resolution γ-Ray Radiography Produced by a Laser-Plasma Driven Electron Source*. In: Phys. Rev. Lett. 94 (2 2005), p. 025003. DOI: 10.1103/PhysRevLett.94.025003. URL: https://link.aps.org/doi/10.1103/PhysRevLett.94.025003.

[116] A. Giulietti et al. *Intense γ-Ray Source in the Giant-Dipole-Resonance Range Driven by 10-TW Laser Pulses*. In: Phys. Rev. Lett. 101 (10 2008), p. 105002. DOI: 10.1103/PhysRevLett.101.105002. URL: https://link.aps.org/doi/10.1103/PhysRevLett.101.105002.

[117] C. P. Ridgers et al. *Dense Electron-Positron Plasmas and Ultraintense γ rays from Laser-Irradiated Solids*. In: Phys. Rev. Lett. 108 (16 2012), p. 165006. DOI: 10.1103/

PhysRevLett.108.165006. URL: https://link.aps.org/doi/10.1103/PhysRevLett.108.165006.

[118] T. Nakamura et al. *High-Power γ-Ray Flash Generation in Ultraintense Laser-Plasma Interactions*. In: Phys. Rev. Lett. 108 (19 2012), p. 195001. DOI: 10.1103/PhysRevLett.108.195001. URL: https://link.aps.org/doi/10.1103/PhysRevLett.108.195001.

[119] J E McMillan et al. *Scintillators and Cherenkov detectors for the registration of 10.8 MeV gamma rays*. In: Journal of Physics: Conference Series 763 (Oct. 2016), p. 012011. ISSN: 1742-6596. DOI: 10.1088/1742-6596/763/1/012011. URL: http://dx.doi.org/10.1088/1742-6596/763/1/012011.

[120] D. J. Corvan, G. Sarri, and M. Zepf. *Design of a compact spectrometer for high-flux MeV gamma-ray beams*. In: Review of Scientific Instruments 85.6 (2014), p. 065119. DOI: 10.1063/1.4884643.

[121] K. T. Behm et al. *A spectrometer for ultrashort gamma-ray pulses with photon energies greater than 10 MeV*. In: Review of Scientific Instruments 89.11 (2018), p. 113303. DOI: 10.1063/1.5056248.

[122] F. Barbosa et al. *Pair spectrometer hodoscope for Hall D at Jefferson Lab*. In: Nucl. Instrum. Meth. A 795 (2015), pp. 376–380. DOI: 10.1016/j.nima.2015.06.012.

[123] Y. Glinec. *Propagation of an ultra intense laser pulse in an under dense plasma : production of quasi monoenergetic electron beams and development of applications*. Thesis also available in english at http://perso.orange.fr/en-vrac/These. Theses. Ecole Polytechnique X, 2006. URL: https://pastel.archives-ouvertes.fr/tel-00131624.

[124] W. H. Press et al. *Numerical Recipes 3rd Edition: The Art of Scientific Computing*. 3rd ed. USA: Cambridge University Press, 2007. ISBN: 0521880688.

[125] A. Mohammad-Djafari. *On the estimation of hyperparameters in Bayesian approach of solving inverse problems*. In: 1993 IEEE International Conference on Acoustics, Speech, and Signal Pro
Vol. 5. 1993, 495–498 vol.5. doi: 10.1109/ICASSP.1993.319857.

[126] M. Piana. *Inversion of bremsstrahlung spectra emitted by solar plasma*. In: SVD and Signal Processing III
Ed. by Marc Moonen and Bart De Moor. Amsterdam: Elsevier Science B.V., 1995, pp. 475–484. isbn: 978-0-444-82107-2. doi: https://doi.org/10.1016/B978-044482107-2/50051-0. url: https://www.sciencedirect.com/science/article/pii/B9780444821072500510.

[127] A. Mohammad-Djafari. *A Full Bayesian Approach for Inverse Problems*. In: Maximum Entropy and Baye
Ed. by Kenneth M. Hanson and Richard N. Silver. Dordrecht: Springer Netherlands, 1996, pp. 135–144. isbn: 978-94-011-5430-7. doi: 10.1007/978-94-011-5430-7_16.

[128] G. H. Golub, P. C. Hansen, and D. P. O'Leary. *Tikhonov Regularization and Total Least Squares*. In: SIAM Journal on Matrix Analysis and Applications 21.1 (Jan. 1999), 185–194. issn: 1095-7162. doi: 10.1137/s0895479897326432. url: http://dx.doi.org/10.1137/S0895479897326432.

[129] C. W. E. van Eijk. *Inorganic scintillators in medical imaging*. In: Physics in Medicine and Biology 47.8 (Apr. 2002), R85–R106. issn: 1361-6560. doi: 10.1088/0031-9155/47/8/201. url: http://dx.doi.org/10.1088/0031-9155/47/8/201.

[130] L. D. Landau. *On the Energy Loss of Fast Particles by Ionisation*. In: J. Phys. (USSR) 8 (1944). Ed. by D. ter Haar. doi: 10.1016/b978-0-08-010586-4.50061-4.

[131] H. Bichsel. *Straggling in thin silicon detectors*. In: Rev. Mod. Phys. 60 (3 1988), pp. 663–699. doi: 10.1103/RevModPhys.60.663. url: https://link.aps.org/doi/10.1103/RevModPhys.60.663.

[132] R L Workman et al. *Review of Particle Physics*. In: Progress of Theoretical and Experimental Physics 2022.8 (Aug. 2022). issn: 2050-3911. doi: 10.1093/ptep/ptac097. url: http://dx.doi.org/10.1093/ptep/ptac097.

[133] M. Berggren et al. *Kinematic edge detection using finite impulse response filters*. In: Nuclear Instruments and Methods in Physics Research Section A: Accelerators, Spectrometers, Detec 1010 (Sept. 2021), p. 165555. ISSN: 0168-9002. DOI: 10.1016/j.nima.2021.165555. URL: http://dx.doi.org/10.1016/j.nima.2021.165555.

[134] L. Torrisi et al. *Metallic etching by high power Nd:yttrium-aluminum-garnet pulsed laser irradiation*. In: Review of Scientific Instruments 71.11 (2000), p. 4330. DOI: 10.1063/1.1287628. URL: https://doi.org/10.1063/1.1287628.

[135] V. Yanovsky et al. *Ultra-high intensity- 300-TW laser at 0.1 Hz repetition rate*. In: Opt. Express 16.3 (2008), p. 2109. ISSN: 1094-4087. DOI: 10.1364/oe.16.002109. URL: http://dx.doi.org/10.1364/OE.16.002109.

[136] Y. I. Salamin. *Fields of a Gaussian beam beyond the paraxial approximation*. In: Appl. Phys. B 86 (2007), p. 319. DOI: 10.1007/s00340-006-2442-4.

[137] A. L'Huillier et al. *Multiply charged ions induced by multiphoton absorption in rare gases at 0.53 μm*. In: Phys. Rev. A 27 (5 1983), pp. 2503–2512. DOI: 10.1103/PhysRevA.27.2503. URL: https://link.aps.org/doi/10.1103/PhysRevA.27.2503.

[138] H. G. Hetzheim and C. H. Keitel. *Ionization Dynamics versus Laser Intensity in Laser-Driven Multiply Charged Ions*. In: Phys. Rev. Lett. 102 (8 2009), p. 083003. DOI: 10.1103/PhysRevLett.102.083003. URL: https://link.aps.org/doi/10.1103/PhysRevLett.102.083003.

[139] J. Gao. *Laser intensity measurement by Thomson scattering*. In: App. Phys. Lett. 88.9 (Feb. 2006), p. 091105. ISSN: 0003-6951. DOI: 10.1063/1.2180869. URL: https://doi.org/10.1063/1.2180869 (visited on 10/09/2023).

[140] S. Ravichandran et al. *Imaging electron angular distributions to assess a full-power petawatt-class laser focus*. In: Phys. Rev. A 108 (5 2023), p. 053101. DOI: 10.1103/PhysRevA.108.053101. URL: https://link.aps.org/doi/10.1103/PhysRevA.108.053101.

[141] O. Har-Shemesh and A. Di Piazza. *Peak intensity measurement of relativistic lasers via nonlinear Thomson scattering*. In: Opt. Lett. 37.8 (2012), pp. 1352–1354. doi: `10.1364/OL.37.001352`. url: `https://opg.optica.org/ol/abstract.cfm?URI=ol-37-8-1352`.

[142] T. G. Blackburn et al. *Model-independent inference of laser intensity*. en. In: Phys. Rev. Accel. Beams 23.6 (June 2020), p. 064001. issn: 2469-9888. doi: `10.1103/PhysRevAccelBeams.23.064001`. url: `https://link.aps.org/doi/10.1103/PhysRevAccelBeams.23.064001` (visited on 01/30/2023).

[143] K. Fleck et al. *Dependence of the number-weighted angular distribution of Compton-scattered photon beams on the laser intensity*. In: Phys. Rev. A 110 (2 2024), p. 023510. doi: `10.1103/PhysRevA.110.023510`. url: `https://link.aps.org/doi/10.1103/PhysRevA.110.023510`.

[144] A. R. Bell and John G. Kirk. *Possibility of Prolific Pair Production with High-Power Lasers*. In: Phys. Rev. Lett. 101 (20 2008), p. 200403. doi: `10.1103/PhysRevLett.101.200403`. url: `https://link.aps.org/doi/10.1103/PhysRevLett.101.200403`.

[145] G. Avoni et al. *Development of a sapphire microstrip detector for gamma beam monitoring*. In: Nuclear Instruments and Methods in Physics Research Section A: Accelerators, Spectrometers, De 1068 (Nov. 2024), p. 169752. issn: 0168-9002. doi: `10.1016/j.nima.2024.169752`. url: `http://dx.doi.org/10.1016/j.nima.2024.169752`.

[146] C. Radier et al. *10 PW peak power femtosecond laser pulses at ELI-NP*. In: High Power Laser Science and 10 (2022). issn: 2052-3289. doi: `10.1017/hpl.2022.11`. url: `http://dx.doi.org/10.1017/hpl.2022.11`.

[147] *EP-OPAL - planning for a next-generation laser user facility dedicated to the study of ultra-high intensity laser-matter interactions*. URL: `https://indico.duke.edu/event/1/contributions/60/`. Sept. 2023.

[148] S. Buck, P. Oliveira, and M. Angelides T.and Galimberti. *A Review of Optical Parametric Amplification at the Vulcan Laser Facility*. In: Photonics 11.6 (May 2024), p. 495. issn:

2304-6732. DOI: 10.3390/photonics11060495. URL: http://dx.doi.org/10.3390/photonics11060495.

[149] X. Wang et al. *Quasi-monoenergetic laser-plasma acceleration of electrons to 2 GeV*. In: Nature Communications 4.1 (June 2013). ISSN: 2041-1723. DOI: 10.1038/ncomms2988. URL: http://dx.doi.org/10.1038/ncomms2988.

[150] H. Kim et al. *Multi-GeV Laser Wakefield Electron Acceleration with PW Lasers*. In: Applied Sciences 11.13 (June 2021), p. 5831. ISSN: 2076-3417. DOI: 10.3390/app11135831. URL: http://dx.doi.org/10.3390/app11135831.

[151] X. Yu et al. *Numerical optimization of transmission bremsstrahlung target for intense pulsed electron beam*. In: Nuclear Engineering and Technology 54.2 (Feb. 2022), 666–673. ISSN: 1738-5733. DOI: 10.1016/j.net.2021.08.021. URL: http://dx.doi.org/10.1016/j.net.2021.08.021.

[152] L. Calvin et al. *Laser-driven muon production for material inspection and imaging*. In: Frontiers in Physics 11 (June 2023). ISSN: 2296-424X. DOI: 10.3389/fphy.2023.1177486. URL: http://dx.doi.org/10.3389/fphy.2023.1177486.

[153] D. W. Phillion and C. J. Hailey. *Brightness and duration of x-ray line sources irradiated with intense 0.53-μm laser light at 60 and 120 ps pulse width*. In: Phys. Rev. A 34 (6 1986), pp. 4886–4896. DOI: 10.1103/PhysRevA.34.4886. URL: https://link.aps.org/doi/10.1103/PhysRevA.34.4886.

[154] B. Kettle et al. *M-L band x-rays (3-3.5 KeV) from palladium coated targets for isochoric radiative heating of thin foil samples*. English. In: Journal of Physics B: Atomic Molecular and Optical Phy 48.22 (Sept. 2015). ISSN: 0953-4075. DOI: 10.1088/0953-4075/48/22/224002.

[155] D Riley et al. *He-like x-ray line emission from laser irradiated sources*. In: Plasma Sources Science and Te 11.4 (Oct. 2002), 484–491. ISSN: 0963-0252. DOI: 10.1088/0963-0252/11/4/315. URL: http://dx.doi.org/10.1088/0963-0252/11/4/315.

[156] G. Carleo et al. *Machine learning and the physical sciences*. In: Rev. Mod. Phys. 91 (4 2019), p. 045002. DOI: 10.1103/RevModPhys.91.045002. URL: https://link.aps.org/doi/10.1103/RevModPhys.91.045002.

[157] G. Karagiorgi et al. *Machine learning in the search for new fundamental physics*. In: Nature Reviews Physics 4.6 (May 2022), 399–412. ISSN: 2522-5820. DOI: `10.1038/s42254-022-00455-1`. URL: `http://dx.doi.org/10.1038/s42254-022-00455-1`.

[158] A. Döpp et al. *Data-driven science and machine learning methods in laser–plasma physics*. In: High Power Laser Science and Engineering 11 (2023). ISSN: 2052-3289. DOI: `10.1017/hpl.2023.47`. URL: `http://dx.doi.org/10.1017/hpl.2023.47`.

[159] E. E. Los et al. *A Bayesian Framework to Investigate Radiation Reaction in Strong Fields*. 2024. arXiv: `2406.19420 [physics.data-an]`. URL: `https://arxiv.org/abs/2406.19420`.

[160] M. Yadav et al. *Machine learning-based analysis of experimental electron beams and gamma energy distributions*. 2023. arXiv: `2209.12119 [physics.acc-ph]`. URL: `https://arxiv.org/abs/2209.12119`.

[161] Hans G. Rinderknecht et al. *On Measuring Stimulated Photon-photon Scattering using Multiple Ultraintense Lasers*. 2025. arXiv: `2503.21856 [hep-ex]`. URL: `https://arxiv.org/abs/2503.21856`.

[162] Y. Peng et al. *Current progress of SEL-100 PW laser facility*. In: 2024 Conference on Lasers and Electro-
Optica Publishing Group, 2024. URL: `https://opg.optica.org/abstract.cfm?URI=CLEOPR-2024-Mo3L_1`.

[163] C. Y. Chien et al. *Highly efficient second-harmonic generation of ultraintense Nd:glass laser pulses*. In: Opt. Lett. 20.4 (1995), pp. 353–355. DOI: `10.1364/OL.20.000353`. URL: `https://opg.optica.org/ol/abstract.cfm?URI=ol-20-4-353`.

[164] M. Suzuki et al. *Highly efficient frequency doubling of high-energy Nd:YAG laser using a CsB3O5 crystal*. In: Optics Communications 283.3 (Feb. 2010), 451–453. ISSN: 0030-4018. DOI: `10.1016/j.optcom.2009.10.015`. URL: `http://dx.doi.org/10.1016/j.optcom.2009.10.015`.

[165] E. Lundström et al. *Using High-Power Lasers for Detection of Elastic Photon-Photon Scattering*. en. In: Physical Review Letters 96.8 (Mar. 2006), p. 083602. ISSN: 0031-9007, 1079-7114. DOI: `10.1103/PhysRevLett.96.083602`. URL: `https://link.aps.org/doi/10.1103/PhysRevLett.96.083602` (visited on 02/18/2025).